I of 2
AD A
109819

	1.0		2.8		2.5
	1.1		3.2		2.2
			3.5		2.0
					1.8
	1.25		1.4		1.6

MICROCOPY RESOLUTION TEST CHART

CERAMIC FINISHING COMPANY

State College, Pennsylvania 16801

LEVEL II

FRACTOGRAPHIC INVESTIGATION OF MICROMECHANISMS OF FRACTURE IN ALUMINA CERAMICS

August, 1981

DTIC
SELECT
JAN 20 1982
E

Prepared by:

Henry P. Kirchner

Robert M. Gruver

John A. Ragosta

011882 007

REPORT DOCUMENTATION PAGE		READ INSTRUCTIONS BEFORE COMPLETING FORM
1. REPORT NUMBER	2. GOVT ACCESSION NO. AD-A109 879	3. RECIPIENT'S CATALOG NUMBER
4. TITLE (and Subtitle) FRACTOGRAPHIC INVESTIGATION OF MICROMECHANISMS OF FRACTURE IN ALUMINA CERAMICS		5. TYPE OF REPORT & PERIOD COVERED SUMMARY REPORT 24 Apr 1979 - 24 Mar 1981
		6. PERFORMING ORG. REPORT NUMBER
7. AUTHOR(s) Henry P. Kirchner Robert M. Gruver John A. Ragosta		8. CONTRACT OR GRANT NUMBER(s) N00019-79-C-0528
9. PERFORMING ORGANIZATION NAME AND ADDRESS Ceramic Finishing Company P.O.Box 498 State College, Pa. 16801		10. PROGRAM ELEMENT, PROJECT, TASK AREA & WORK UNIT NUMBERS
11. CONTROLLING OFFICE NAME AND ADDRESS Naval Air Systems Command Department of the Navy Washington, D.C. 20360		12. REPORT DATE 31 November 1981
		13. NUMBER OF PAGES 114
14. MONITORING AGENCY NAME & ADDRESS(If different from Controlling Office)		15. SECURITY CLASS. (of this report) Unclassified
		15a. DECLASSIFICATION/DOWNGRADING SCHEDULE

16. DISTRIBUTION STATEMENT (of this Report)

Distribution of this report is unlimited

17. DISTRIBUTION STATEMENT (of the abstract entered in Block 20, If different from Report)

18. SUPPLEMENTARY NOTES

19. KEY WORDS (Continue on reverse side if necessary and identify by block number)

96% alumina	fracture mode	computerized analysis
hot pressed alumina	fracture profiles	fractography
coarse grained 99+% alumina	fracture mechanisms	flaw linking
work of fracture	electron channeling	
crack branching	environmental effects	

20. ABSTRACT (Continue on reverse side if necessary and identify by block number)

The variations in the fracture features along radii from fracture origins in alumina ceramics were characterized and compared at equal values of stress intensity factor. The flaws at fracture origins, flaw linking, fraction of intergranular and transgranular fracture; linear features such as cleavage steps, surface roughness profiles, and crack branching were investigated for specimens fractured at various stresses and in selected

DD FORM 1473 1 JAN 73   EDITION OF 1 NOV 65 IS OBSOLETE

environments using multiple techniques such as SEM, TEM, selected area electron channeling, and computerized surface roughness analysis.

In alumina ceramics subcritical crack growth occurs mainly by wavy transgranular fracture which gives rise to the so-called reflecting spots that surround the fracture origin. The subcritical crack growth boundaries are characterized by minima in the percent intergranular fracture and scattered pullouts and projecting grains. A particularly striking example of these pullouts and projecting grains was observed in coarse grained 99+% alumina. At greater radii the percentages of intergranularly fractured grains and grains with linear features increased and the surfaces had a more disturbed appearance.

Effects of environment on the fracture mode were investigated in specimens from strength measurements and work of fracture tests. Present evidence indicates that the presence of water in the environment enhances transgranular fracture.

These results are expected to be useful in developing improved methods for locating flaws at fracture origins, locating subcritical crack growth boundaries, understanding the mechanism of transition from subcritical to critical crack growth, and improving the resistance to subcritical crack growth and fracture toughness of alumina ceramics. It is increasingly apparent that variations in micromechanisms of fracture with variations in the stress intensity factor acting at the crack front are important in understanding the mechanical properties of ceramics.

CERAMIC FINISHING COMPANY

State College, Pennsylvania 16801

FRACTOGRAPHIC INVESTIGATION OF MICROMECHANISMS
OF FRACTURE IN ALUMINA CERAMICS

August, 1981

Prepared by:

Henry P. Kirchner

Robert M. Gruver

John A. Ragosta

TABLE OF CONTENTS

FOREWARD

LIST OF TABLES

LIST OF FIGURES

LIST OF FIGURES (continued)

LIST OF FIGURES (Continued)

I. INTRODUCTION

At low and moderate temperatures, fractures in ceramics originate at preexisting flaws. Many types of flaws have been observed at fracture origins including pores, cracks, large grains, poorly bonded regions and so forth. In a general sense, any stress concentrator can be regarded as a flaw. Therefore, flaws are not always characterized by absence of material as at pores and cracks, but may also involve regions of low elastic modulus relative to the average for the ceramic body or regions of high elastic anisotropy.

Each polycrystalline ceramic specimen contains large numbers of flaws of widely varying characteristics. When uniform tensile stresses are applied to such a specimen a crack will tend to initiate at the most severe or vulnerable flaw. The severity or vulnerability of such a flaw depends not only on the stress concentrating characteristics of the flaw itself but also on external factors such as local variations in the resistance to crack growth, localized residual stresses and the effect of environment.

After a crack has initiated at a flaw, the crack growth or propagation is governed by factors that can be described in fracture mechanics terms and that include the dependence on the load history and environment (temperature, chemistry, etc.). When a crack is present, it is possible to define a stress intensity factor (K_I) which for a uniform tensile stress (σ) perpendicular to a crack of length (c) is

$$K_I = \frac{Y}{Z} \, \sigma \, c^{\frac{1}{2}} \tag{1}$$

where Y is a dimensionless term that depends on the crack depth and the test geometry and Z is another dimensionless quantity that depends on the crack shape. In reactive environments subcritical crack growth will begin

2

when $K_I > K_o$ where K_o is the threshold stress intensity factor for subcriti-
cal crack growth. The crack growth rate or crack velocity (V) varies with
stress intensity factor according to

$$V = A \left(\frac{K_I}{K_n} \right)^n \tag{2}$$

where K_n is a normalizing factor with units of stress intensity factor and A
and n are constants for a particular material and set of environmental con-
ditions.

As c increases, K_I also increases. At high crack growth rates, diffu-
sion of the environment may not be able to keep up with the crack front. In
that case, the dependence of V on K_I changes from that in equation (2) and
the values of V are lower than otherwise expected. Eventually, K_I increases
to a critical value (K_{IC}) where catastrophic fracture occurs. At the critical
condition

$$K_{IC} = \frac{Y}{Z} \sigma_f c_c^{\frac{1}{2}} \tag{3}$$

where σ_f is the fracture stress and c_c is the critical crack size.

There are substantial localized variations in the appearance of fracture
surfaces as the observations proceed outward along radii from fracture origins.
Many of these variations seem to occur systematically, suggesting that the
micromechanisms of fracture are influenced by factors such as the stress
intensity factor at the crack front and the crack velocity as well as the
localized variations in material properties. Therefore, a principal objective
of the present program has been to relate these localized variations in frac-
ture features to major variables such as K_I, V and environment on the one hand
and to reasonable micromechanisms of fracture on the other.

It should be noted that it is still not uncommon to see published photo-
graphs illustrating the mode of fracture of particular ceramics that do not

specify the location of the photograph in relation to the fracture origin and that are used to discuss the mechanisms controlling failure of the material. It is clear that if fracture features vary along radii from the fracture origin to the subcritical to critical crack growth boundary, only features in this region are meaningful in terms of micromechanisms controlling failure. Features observed at greater radii may be interesting in their own right but they do not control failure.

The first observations in our laboratory that revealed variations in the fracture mode along radii from fracture origins were observations of reflecting spots surrounding fracture origins in polycrystalline alumina[1]. Subsequently, these reflecting spots were shown to represent areas of what we have called wavy transgranular fracture[2]. Evans and Tappin[3] used a fracture mechanics method to relate the sizes and shapes of flaws observed at fracture origins to the effective surface energy (γ_i) necessary for crack initiation. Their equation is similar to equation (3) except that we have substituted K_{IC} for $(2E\gamma_c)^{\frac{1}{2}}$. They used critical flaw size calculations based on this equation to support the reasonableness of their suggested flaw boundaries.

Physically, one would expect the micromechanisms of fracture at each point on the fracture surface to be the mechanism requiring the minimum energy, considering the time available for the local fracture to occur. It should be noted that the energy required may depend on the mechanism of fracture of the immediately preceeding fracture element which influences the orientation of the crack, the local crack velocity and other important characteristics. Two important micromechanisms of fracture are intergranular and transgranular fracture. The fracture energies for transgranular fracture

of a particular crystal can vary substantially depending on the particular lattice plane. For example, in sapphire the fracture energy varies from 6 to > 40 Jm^{-2} depending on the orientation of the lattice plane[4]. Little is known about the fracture energies for intergranular fracture but it seems reasonable to expect large variations in grain boundary fracture energies depending on the composition and thickness of the grain boundary phases and the orientations of the adjoining crystal surfaces. Also, intergranular fracture energies in alumina ceramics must be close to those for transgranular fracture because both intergranular and transgranular fracture occur in close proximity.

This report describes the results of research on the most recent of three related contracts. The first of these contracts emphasized locating and characterizing flaws at fracture origins and correlating the flaw characteristics with material properties such as strength[5-7]. Four materials, 96% alumina, hot pressed (H.P.) alumina, H.P. silicon nitride, and H.P. silicon carbide were fractured at various temperatures and loading rates. This investigation revealed the wide variety of flaw types at fracture origins and provided a substantial number of fracture surfaces for further investigation.

In the second contract, fracture surfaces from the earlier investigation were characterized along radii from the fracture origins[2,8-11]. Scanning electron micrographs were prepared of each element of area along the radii and fitted together to form composite photographs. Grids with openings of about one grain size at the particular magnification were placed over the composite photographs. The area in each grid space was rated as either intergranular or transgranular fracture. These ratings were averaged over paths that were ten grid spaces wide and correlated with the K_I acting at each increment of radius.

In each case (96% alumina, H.P. alumina, H.P. silicon nitride) the percent intergranular fracture (PIF) increased when $K_I > K_{IC}$. In the alumina ceramics, the intervening maxima and minima in PIF occurred at K_I values that seemed to correlate with the K_{IC} values for fracture on the various lattice planes in sapphire. Based on these observations it was concluded that when K_I at the crack tip became high enough to allow fracture on an additional lattice plane, transgranular fracture increased and PIF decreased to a new minimum. Then, as the crack velocity increased, PIF increased again. Criteria were developed for locating subcritical crack growth boundaries in H.P. Al_2O_3, 96% Al_2O_3 and H.P. Si_3N_4.

The research on the present contract is based on the earlier research and involves development of new methods of analysis of fracture surfaces and application of available methods to analysis of fracture surfaces in several materials. The principal investigation emphasized study of three alumina ceramics of various grain sizes and the report is limited to these materials. As mentioned previously, the principal objective of the present research is to relate localized variations in fracture features to major variables such as K_I,V, and environment on the one hand and to reasonable micromechanisms of fracture on the other. In the following sections the effects of K_I,V and environment on the fracture features in three different alumina ceramics are described.

II. HOT PRESSED ALUMINA

This hot pressed alumina is a dense, fine-grained material prepared at Ceramic Finishing Company in the form of cylindrical rods about 3.3 mm diameter. The densities ranged from 99.5 to 99.7% of theoretical and the average grain size ranged from 1 to 3 µm. The specimens were fractured in flexure.

A. Relationship of K_I to Fracture Mode

Specimens were chosen for characterization of fracture features along radii from the fracture origins mainly based on the radial symmetry of the fracture features, especially the reflecting spots and the fracture mirror (crack branching) boundary. These criteria evolved in response to difficulties encountered in attempting to characterize fracture surfaces with unsymmetrical features where we assume that the crack front was irregular in shape. It was also advantageous to use specimens that fractured after a relatively large amount of subcritical crack growth, for example, by delayed fracture testing. This crack growth spreads the significant fracture features over larger areas so that the systematic variations are more likely to emerge from the background of random variations caused by variations in crystal orientation, grain size, and grain boundary characteristics.

The fracture origins were located mainly by means of the reflecting spots which were observed by optical microscopy. The correctness of the choice of fracture origin was confirmed in each case by locating the intersection of extensions of the hackle and other radially oriented fracture markings and by locating the intersection of the fracture mirror radii. The flaws at the fracture origins were characterized by scanning electron microscopy. Composite scanning electron micrographs (1000-2000X) were prepared

showing the fracture origin and the fracture surface along radii from the fracture origin.

The percentages of intergranular and transgranular fracture were determined along radii from the fracture origins. As in the previous contract, a transparent grid with spaces approximately equal to one grain size in the photographs, and 10-20 spaces wide, was placed on the composite photograph. The area in each grid space was rated as to whether it was predominantly intergranular or transgranular. These results were averaged across a path ten or twenty grid spaces wide. This process was repeated for adjoining rows of the grid. The percentages of intergranular and trans-granular fracture vary considerably from one row to the next so averages were calculated for each row which included the results from the preceding and following rows to form three row running averages.

The stress intensity factors were calculated for each row using equation (1) with the Y value taken as 2.0 for surface flaws and 1.8 for internal flaws and $Z = 1.57$, the value for semicircular cracks. The assumption of semicircular or circular cracks was based on the radial symmetry of the reflecting spots originally used to select the specimens. Using these data, curves of K_I vs. PIF were plotted.

Strictly speaking, equation (1) applies only when $K_I \leq K_{IC}$. However, the variations in fracture mode continue into the range $K_I > K_{IC}$ so that we needed an energy or stress intensity related quantity to use for comparisons in this range. Therefore, we have defined an apparent stress intensity factor (K_I^*) that can be calculated using equation (1) to be used when $K_I > K_{IC}$. In effect, the calculation assumes that the inertial or kinetic energy effects at the crack tip are negligible at high crack velocities. This assumption has considerable precedent[12,13].

A fracture surface of a specimen (R-45, loaded at a linear loading rate at room temperature) with an internal fracture origin is shown in Figures 1 and 2. Figure 1 shows the specimen at low magnification. The fracture origin is located near the top of the fracture surface. It is surrounded by a rather smooth region which is called the mirror region and by radiating ridges and valleys that are called hackle. These features are relatively well defined because of the high fracture stress which was 660 MPa.

Figure 2 shows the fracture origin, indicated by an arrow, located about 20 μm below the specimen surface. The flaw at the fracture origin appears to be a small poorly bonded region. The fracture origin is surrounded by a small area of intergranular fracture out to radii of 10-15 μm. Surrounding this area is a ring of transgranular fracture that extends to radii of 20-35 μm. Then, there is an incomplete ring of increased intergranular fracture and another ring of primarily transgranular fracture extending to about 50 μm. At still greater radii, the fracture origin is surrounded by elongated areas of transgranular fracture that are oriented so that they radiate from the fracture origin like spokes in a wheel.

The critical flaw size for Specimen R-45 was calculated assuming a circular flaw subjected to uniform tensile stresses perpendicular to the plane of the crack. K_{IC} for this hot pressed alumina was taken to be 4.2 MPa $m^{\frac{1}{2}}$ which is the value measured for a similar material by Bansal and Duckworth[14]. The critical flaw radius was about 30 μm. In evaluating this result it is well to bear in mind that intergranular cracks act as though they are somewhat blunt because of the irregularities at the crack front. Therefore, as the flaw extends to form the transgranularly fractured ring, the crack front becomes less irregular, more closely approximating the sharp crack assumed in the analysis.

Figure 1. Fracture surface of H.P. alumina (Specimen R-45 fractured using a linear loading rate in air at room temperature, σ_F = 660 MPa, 20X).
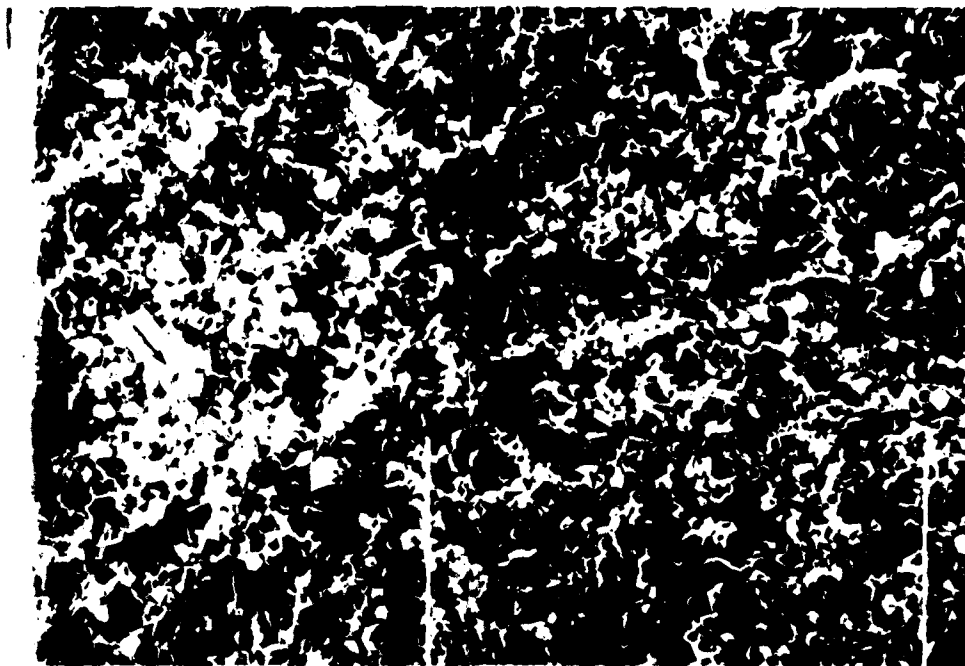
Figure 2. Fracture surface surrounding internal fracture origin in H.P. alumina (Specimen R-45, σ_F = 660 MPa, arrow indicates fracture origin, 1000X).

The K_I vs. PIF curve for specimen R-45 is given in Figure 3. The PIF values for K_I < 2 or 3 MPa $m^{\frac{1}{2}}$ should be considered to be characteristics of the flaw at the fracture origin which is mainly intergranular, rather than characteristics of the subsequent crack propagation. At higher K_I values the PIF decreases and passes through a series of two or three minima at about 3.9, 4.8 and 5.8 MPa $m^{\frac{1}{2}}$. These minima are located in the rings of trans-granular fracture described above.

At higher K_I values PIF increases gradually. However, the actual PIF values may vary substantially depending on the relationship of the grid to the spoke-like regions of transgranular fracture. There is no definite explanation of these spoke-like features. Tentatively, we think of them as regions in which the fracture proceeded in advance of the average crack front. In other words, the radiating transgranular regions may represent "tongues" of fracture ahead of the average crack front where the fracture occurred at relatively low K_I values. This suggestion leads to the further suggestion that the intergranular regions represent resistant regions that did not frac-ture until later, after K_I increased to a much higher value.

The transgranularly fractured radial regions are considered to form first because we associate transgranular fracture with fracture at low K_I and V values. Intergranular fracture is associated with microcracking that is con-sidered to occur at higher K_I values. Because the regions between the trans-granularly fractured spokes would be subjected to very high K_I, it is not surprizing that these regions fracture intergranularly.

Another reason for thinking that the spoke-like regions represent regions that fractured transgranularly at low K_I values is the resemblance of these regions to areas formed by flaw linking. Flaw linking is discussed in more detail in the next section.
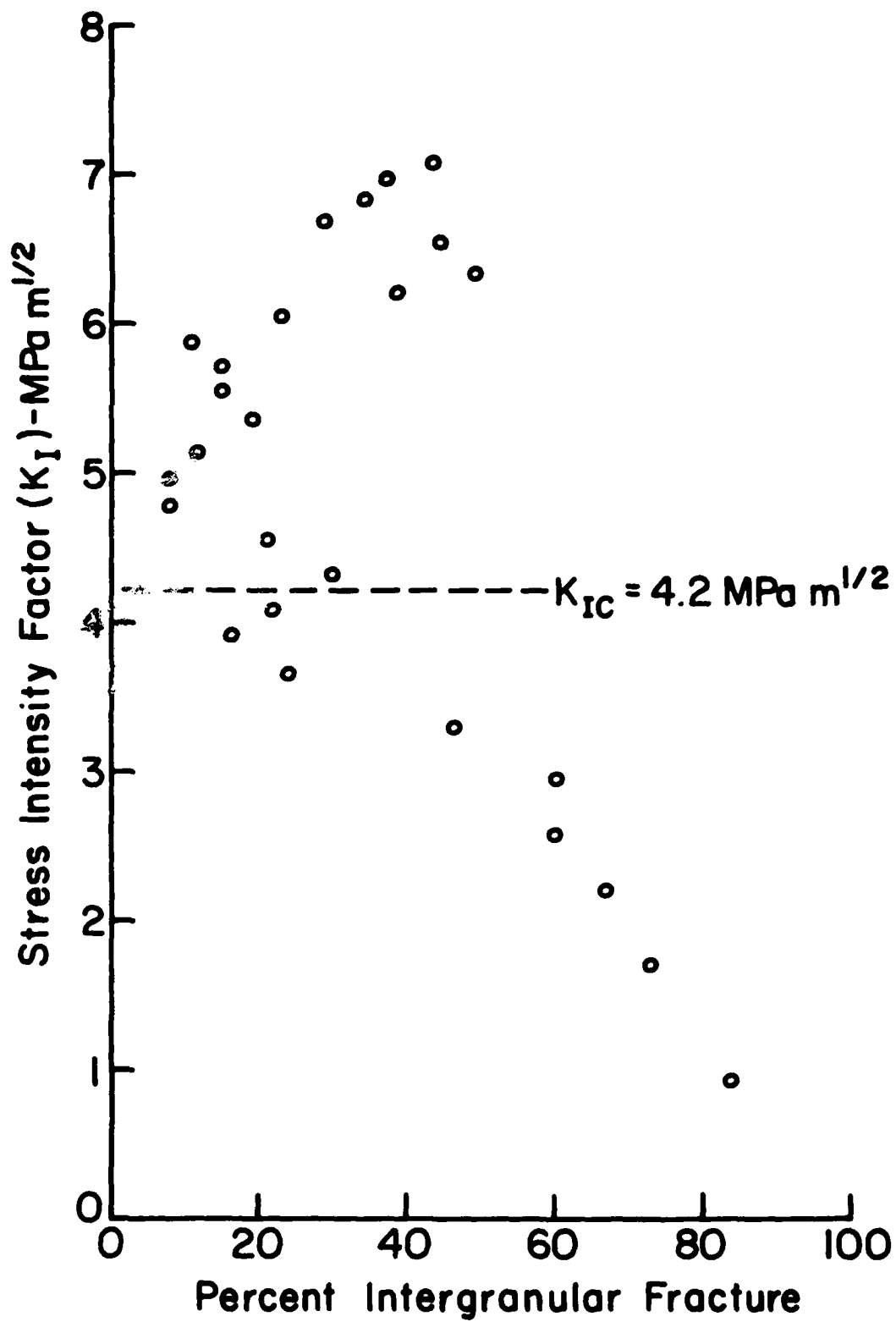
Figure 3. Stress intensity factor vs. PIF of H.P. alumina specimen subsurface fracture origin (Specimen R-45, σ_F = 660 MPa).

Another example of the variations in intergranular and transgranular fracture, in this case a delayed fracture specimen that fractured at a surface flaw, is given in Figure 4. This specimen (D-13) failed at 458 MPa after 426 seconds under load. The fracture origin appears to be a machining flaw about 20-30 μm deep. Therefore, the lower part of the curve where $K_I <$ 2 or 3 MPa m$^{\frac{1}{2}}$ represents mainly a preexisting flaw which was formed by mechanisms involving compressive and shear stresses so that the fracture mode in this K_I range is not directly related to the subsequent crack propagation during delayed fracture testing. The photographs of the fracture surface show two fairly well defined bands of transgranular fracture surrounding the fracture origin. These bands are represented in the figure by the regions of low PIF at $K_I \cong$ 4.5 and 5.7 MPa m$^{\frac{1}{2}}$. Assuming a semicircular surface flaw, the critical flaw radius is about 52 μm at K_{IC} = 4.2 MPa m$^{\frac{1}{2}}$. Beyond the second band of transgranular fracture there are elongated regions of transgranular fracture that are oriented radially like spokes in a wheel as was the case in specimen R-45.

The results presented in this section are based on reexamination of the photographs of fractures analysed during the previous contract and provide additional confirmation of the variations in fracture mode with K_I reported earlier[8] as well as new fractographic observations.

B. Flaw Linking

Evans and Tappin[3] invoked flaw linking as a mechanism to explain the presence of surface cracks large enough to cause failure of alumina ceramics at the measured fracture stresses. Flaw linking is a mechanism of subcritical crack growth in which the stress concentrations at neighboring flaws increase the crack growth rates in the ligament between the flaws leading to failure
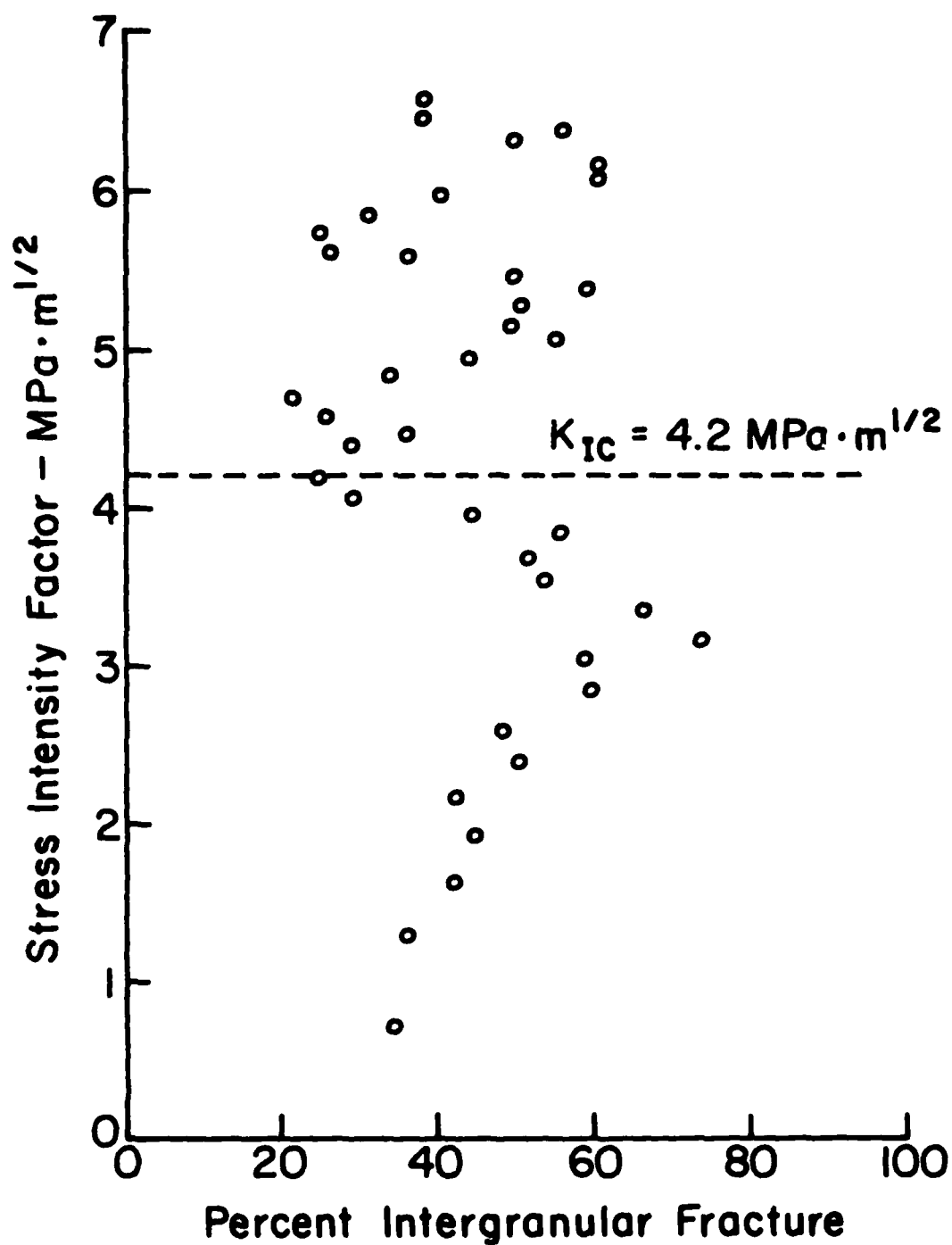
Figure 4. Stress intensity factor vs. percent intergranular fracture (H.P. alumina Specimen D-13 fractured at 458 MPa).

of the ligament to create a single larger flaw. Evans and Tappin do not

discuss the fractographic, as distinguished from fracture mechanics criteria

that they used to determine the existence of flaw linking. The present

investigation has provided further evidence that subcritical crack growth

occurs primarily by transgranular fracture in these alumina ceramics.

Many cases of apparent linking of surface flaws have been observed. In

these cases the space between the surface flaws is primarily wavy transgran-

ular fracture with a very low area density of so-called linear features showing

that the stress intensity factor acting during linking was low. However, in

many of these cases it is difficult to explain the existence of the linking

because the calculated stress intensity factor is so low that any subcritical

crack growth including linking seems unlikely. In other words, if the extent

of subcritical crack growth is as great as is indicated by the appearance of

the fracture surface, how can the K_I at the flaw have been great enough to

start the process? Of course, in the case of machining flaws localized

residual stresses can increase K_I substantially and in coarse grained bodies

localized stresses due to thermal expansion or elastic anisotropy might con-

tribute, but in the present fine grained hot pressed alumina and the 96%

alumina to be described later there is little evidence in most cases to suggest

that these explanations apply so the dilemma remains unsolved.

In cases of linkage of subsurface flaws with the surface, one can

frequently be more confident that linkage has occurred. In this investigation

a few cases were found in which relatively large subsurface flaws linked to

the surface. An example involving a 50 μm flaw, consisting of coarse grains,

that linked to the surface is illustrated in Figure 5. The specimen was

loaded at a constant loading rate and fractured at 651 MPa. In this case
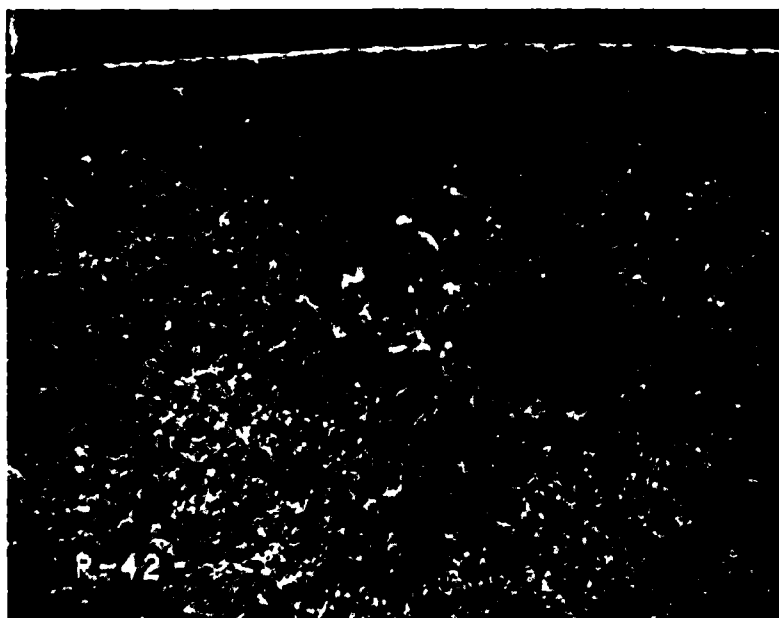
Figure 5. Linking of a subsurface flaw with the
surface (H.P. alumina specimen R-42,
σ_F = 651 MPa, 500X).

the linkage involves 40 μm crack growth which is reasonable in terms of

range of K_I values in which significant subcritical crack growth can occur.

The large areas of wavy transgranular fracture show clearly that the sub-

critical crack growth occurred by that mechanism.

C. Objective Methods of Fracture Surface Analysis

It is highly desirable to develop more objective methods of fracture

surface analysis. One approach is to correlate the features of interest

with an objectively measurable variable such as surface roughness, then

measure the variable and interpret the results in terms of the features

of interest. This approach has been investigated using two methods

(1) direct comparison of SEM brightness profiles with photographs of fracture surfaces and (2) computerized analysis of surface profiles and comparison with K_I vs. PIF curves.

Comparison of SEM brightness profiles with photographs of fracture surfaces

Brightness profiles are compared with features on glass fracture surfaces in Figure 6 to illustrate the method used. Each photograph of the glass surface is paired with an SEM brightness trace. The brightness trace can be understood by comparing the trace (B) with the fracture surface (A). Starting on the left side, the trace is relatively high because of the bright background. The path of the trace on the fracture surface is indicated by the arrows. When the trace crosses the edge of the specimen into the mirror region, the trace goes to a lower level because of the darker surface, but the trace is smooth because the surface is smooth. At the mirror-mist boundary the trace indicates very small variations in brightness that occur because of small scale surface roughness. At the mist-hackle boundary the amplitude of these variations increases substantially. Large scale branching occurs at this boundary. After branching the surface becomes much smoother again. The mist and mist-hackle boundary are shown in more detail in C and D. Also, note that the mirror-mist and mist-hackle boundaries recur at about twice the original radii.

Examples of similar traces in a hot pressed alumina specimen are given in Figure 7. The specimen (D-12) was fractured by delayed fracture in 362 seconds at 467 MPa. A and B show the trace at low magnification. The edge of the specimen is indicated by an increase in brightness. After the trace crosses the edge of the specimen, the scale of the roughness is small. The crack branching (mirror) boundary is not very evident in A. Therefore, the
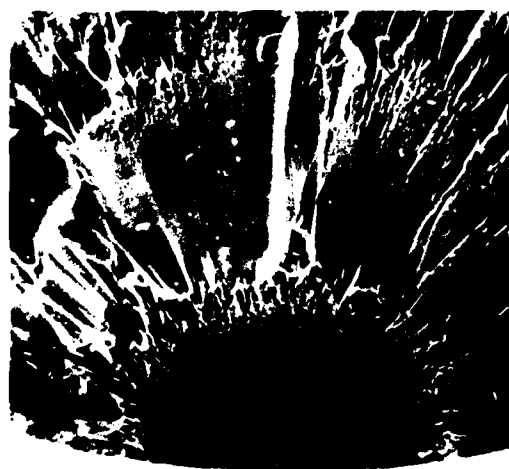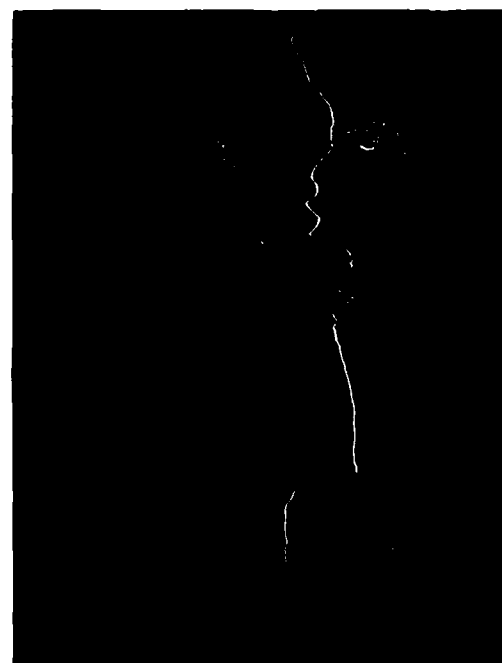
Figure 6. SEM brightness profiles of a glass fracture surface; (A,B), fracture origin including mirror and hackle; (C,D), detail of the mist-hackle boundary (Glass specimen #6).

18
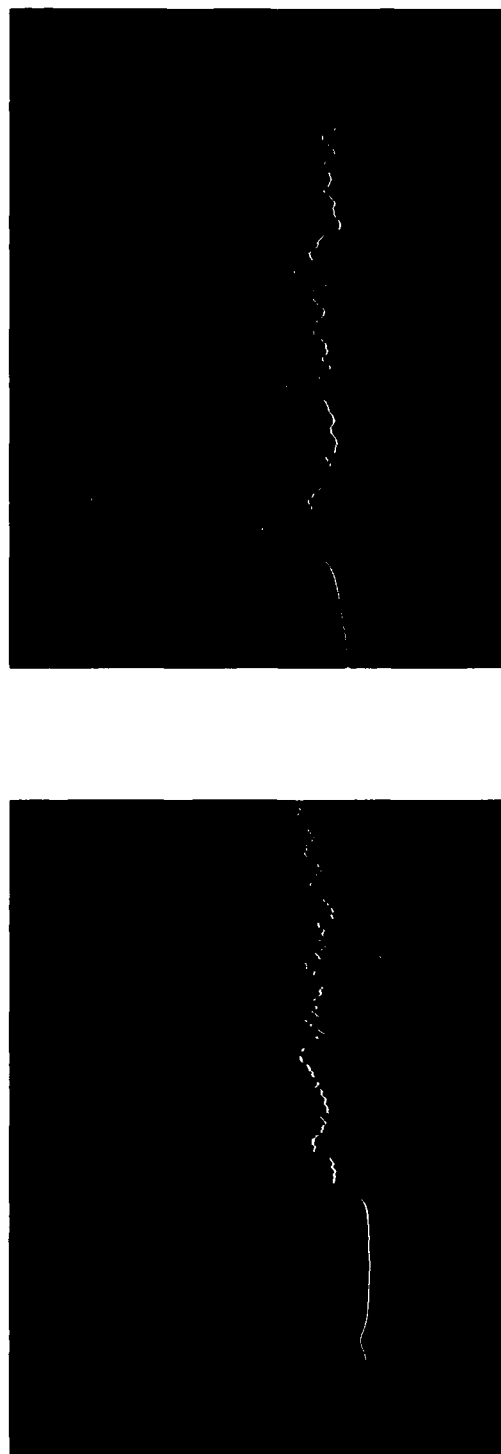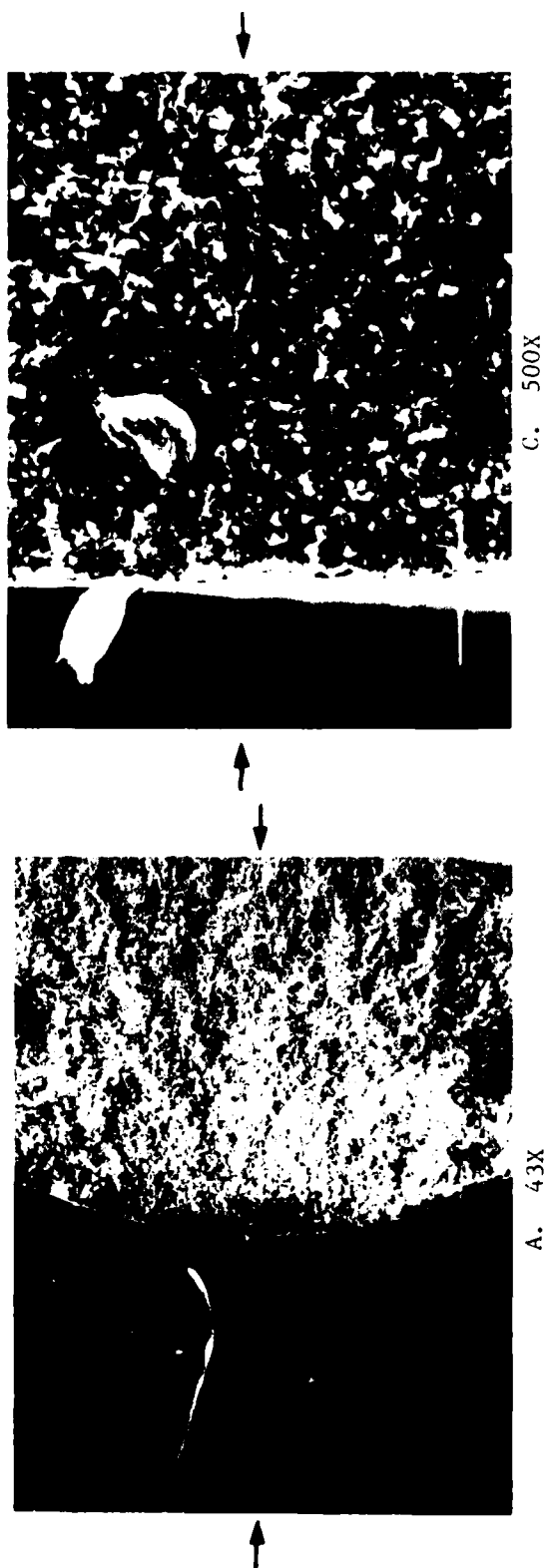
Figure 7. SEM brightness profiles of a hot pressed alumina surface: (A,B), fracture origin at low magnification; (C,D), fracture origin at higher magnification (Specimen D-12).

radius to the boundary was calculated using the mirror constant and the fracture stress yielding 449 μm or 486 μm depending on the mirror constant value used[15]. At 43X, the crack branching boundary is expected at 1.9-2.1 cm. to the right of the edge of the specimen. This location corresponds to the second major peak in the trace showing that the brightness variations can be used to detect the crack branching in H.P. alumina. At greater distances from the fracture origin the surface is somewhat rougher but the features are not very distinctive.

At higher magnification in C and D the trace shows a series of sharp peaks interspersed with flatter valleys. The K_I values represented by the locations of these brightness peaks on the fracture surface were calculated. Although in some cases the brightness peaks correspond to regions of high PIF, the results were not completely consistent. It appears that using one trace, as was done in this case, a single intergranularly fractured grain can cause a substantial peak. Therefore, we conclude that this method is too sensitive to these localized variations to be useful for analysis of the mode of fracture unless the average of several parallel traces is used.

Computerized analysis of fracture surface profiles

It is possible to record the signals reaching the detectors in the SEM on magnetic tape and then to operate on the data to investigate other methods of analysis. LeMont Scientific Company, based on research by E. W. White, J. Lebiedzik and their associates at Penn State University, has developed several methods of computerized analysis of SEM images[16]. One of these methods involves the measurement of surface profiles. In an earlier contract, a preliminary attempt was made to use the existing computer program to analyse fracture surfaces in ceramics[17]. The computer plotted the surface profile,

determined the average elevation of the entire trace, calculated the RMS

deviation from the average for intervals along the trace and plotted the

results as a bar chart. In its original form, the method was insensitive

as a method of analysis of the fracture mode because the large scale waviness

of the fracture surface had a larger effect on the measured surface roughness

than the localized variations caused by intergranular and transgranular

fracture.

In the present program the computer program was revised to provide for

determining the slopes of small intervals of the trace. Then the surface

roughness of the interval was determined by the deviations of the surface

from that slope. The surface roughness of each interval was calculated as

a percentage of the greatest roughness observed for the trace and the

results were plotted as a bar chart. The program was tested by traversing a

path perpendicular to the surface of H.P. alumina specimen D-13, a delayed

fracture specimen fractured at 458 MPa. The path did not begin exactly at

the fracture origin so that it is not exactly a radius from the fracture

origin. The results are given in Figure 8 in which the RMS surface roughness

as a fraction of the maximum roughness is shown by the bars for various

distances from the surface, increasing from the of the figure. As

indicated in the heading, the interval over which the roughness was averaged

was 4.97 µm which is a few (3-5) grains. The height was measured at points

0.24 µm apart within each of the intervals so that results for 21 such points

were used to calculate the roughness for each interval. The roughnesses

varied from 9×10^{-2} µm RMS to 1.8 µm RMS indicating a high degree of sensi-

tivity to local conditions. This sensitivity seems to be improved compared

with the trials in the earlier contract before the new computer program was

available.

```
SAMPLE ID:  C.F. ALUMINA D-13                              DATE: 22JAN.80
LINE   1   MODE = VERTICAL      POINTS/GROUP =    21
INTERVAL =          4.96557 UM  POINT SPACING =          0.23646 UM


LOCAL RMS ROUGHNESS VERSUS LENGTH
-----------------------------------------------------------------------------
                       RMS                                              RMS
                  9.05E-02                                         1.77E 00
                    MIN                                            1 MAX
  LENGTH    RMS    0    1    2    3    4    5    6    7    8    9    0
  (UM)     (UM)    0----0----0----0----0----0----0----0----0----0----0
4.97E 00  2.13E-01 (****
9.93E 00  8.31E-01 (**********************
1.49E 01  1.66E-01 (**
1.99E 01  1.65E 00 (*************************************************
2.48E 01  2.48E-01 (*****
2.98E 01  2.90E-01 (******
3.48E 01  2.98E-01 (******
3.97E 01  9.05E-02 (
4.47E 01  1.94E-01 (***
4.97E 01  3.17E-01 (*******
5.46E 01  8.14E-01 (*********************       <---- K_I = 4.3 MPa m^(1/2)
5.96E 01  6.50E-01 (*****************
6.46E 01  1.17E 00 (*******************************
6.95E 01  1.02E-01 (
7.45E 01  7.20E-01 (*******************
7.94E 01  8.36E-01 (**********************
8.44E 01  2.14E-01 (****
8.94E 01  1.17E-01 (*
9.43E 01  1.78E-01 (***               <---- K_I = 5.6 MPa m^(1/2)
9.93E 01  1.06E-01 (
1.04E 02  2.26E-01 (****
1.09E 02  1.77E 00 (**************************************************
1.14E 02  3.42E-01 (*******
1.19E 02  5.68E-01 (**************
1.24E 02  1.09E-01 (*
```

Figure 8. RMS surface roughness as a fraction of maximum roughness
for various distances from the surface.

Figure 8 shows several regions of low roughness at various distances from the surface. The variation of PIF with K_I was previously determined for this specimen (D-13) by the manual method, along a slightly different path with the results shown in Figure 4. The K_I vs. PIF curve shows minima in PIF (maxima in transgranular fracture) at about 4.5 and 5.7 MPa $m^{\frac{1}{2}}$, close to the values of 4.3 and > 5.6 MPa $m^{\frac{1}{2}}$ determined for fracture on the $\{\bar{1}\bar{1}26\}$ and (0001) lattice planes. The crack lengths at which these K_I values are expected to act at the crack front are indicated by arrows on the bar chart (Figure 8) where the minima in PIF are close to minima in surface roughness indicating that the computerized method of analysis may be yielding useful information.

Based on the early indications that the computerized method of analysis could be used to characterize the fracture mode in H.P. Al_2O_3, extensive trials were done in an effort to develop the technique. The objectives included identifying the best combination of interval for averaging, magnification of the trace, number of points per group and the point spacing. Other objectives involved averaging of parallel traces to improve the relia- bility and analysis of several traces radiating at various angles from a flaw to determine the consistency of the roughness variations from one trace to another and the symmetry of the fracture features.

This program yielded an overwhelming amount of data and only part of the data has been evaluated so far.

Some of the most meaningful data obtained thus far were obtained for Specimen R-45, the specimen with an internal fracture origin that was described previously. Roughness traces were made perpendicular, parallel and at 45° to the surface of the specimen at two magnifications and at

averaging intervals of 5, , ... surface profile is
superimposed on a photograph . . . . the fracture
surface in Figure 9. The surface . . . . top of the
photograph. The heavy white line represents the path of the roughness
analysis on the fracture surface. The fracture origin is the rough appear-
ing region to the left of the white line just under the surface. The
roughness trace is the lighter line with deviations showing differences in
elevation plotted horizontally.
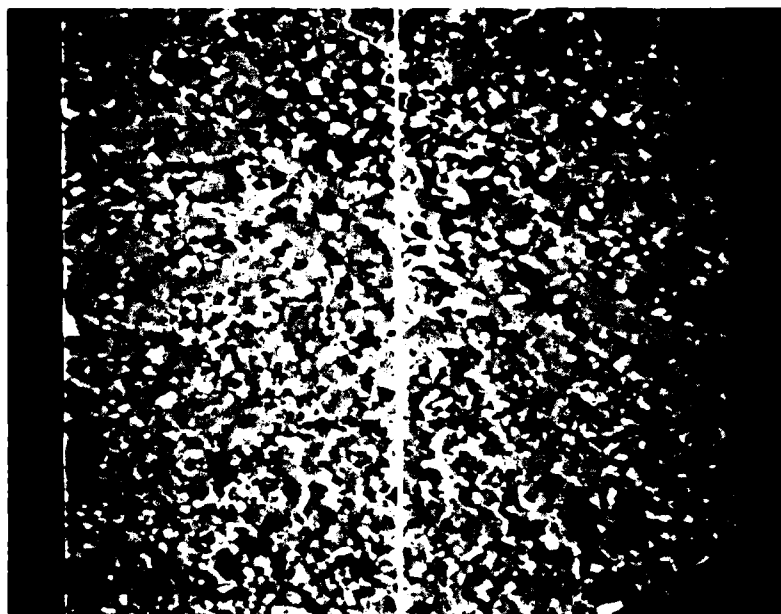
Figure 9. Roughness trace, H.P. Al₂O₃ specimen R-35
with internal fracture origin (816X).

The surface roughness values for an averaging interval of 3.0 μm, about two or three grains, are plotted vs. K_I together with the "manually" determined PIF values in Figure 10. The variability of both the surface roughness and PIF values has been reduced by using three row running averages in which, at a particular K_I, the local value is averaged together with the preceeding and following values. The roughness scale was selected so that the maximum roughness values were approximately equal to the maximum PIF values. It is apparent that, in this case, there is a strong correlation between the surface roughness and the PIF.

The symmetry of the surface roughness variations was investigated by comparing the surface roughness variations for traces parallel to the surface and at a 45° angle to the surface with the trace perpendicular to the surface. In one case there was reasonable agreement between a horizontal trace and a perpendicular trace as shown in Figure 11. Except near $K_I = 4.2$ MPa $m^{\frac{1}{2}}$ the two curves are quite similar. It is interesting that the small peak in roughness at $K_I = 4.2$ MPa $m^{\frac{1}{2}}$ in the perpendicular trace is absent from the 45° trace. Therefore, of the curves analysed, the 45° trace is closest to the expected result.

The observed correlation between the surface roughness and PIF gives reason to hope that the computerized method of analysis of surface roughness can provide an indirect but more objective method of determining variations of fracture mode with K_I in ceramics. The present program has shown that, to make available the full potential of the method, it will be necessary to extend the computer program so that the data can be analysed automatically and displayed in useful form. Among the desired improvements are:

1. Averaging of the roughnesses of several parallel traces.
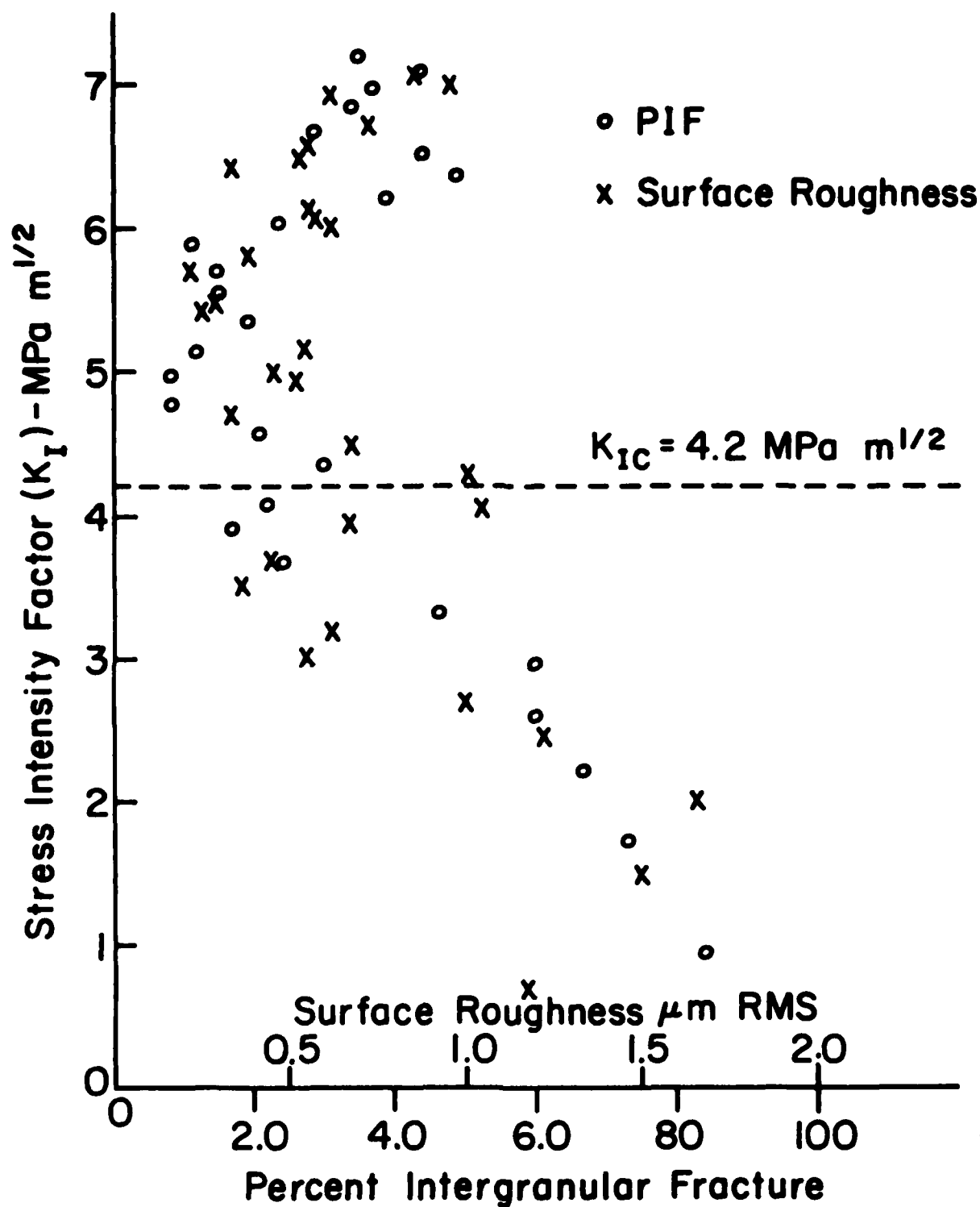
Figure 10. Stress intensity factor vs. PIF and fracture surface roughness along a radius from the fracture origin (H.P. alumina Specimen R-45, σ_F = 660 MPa, vertical scan, 816X, three row averages).
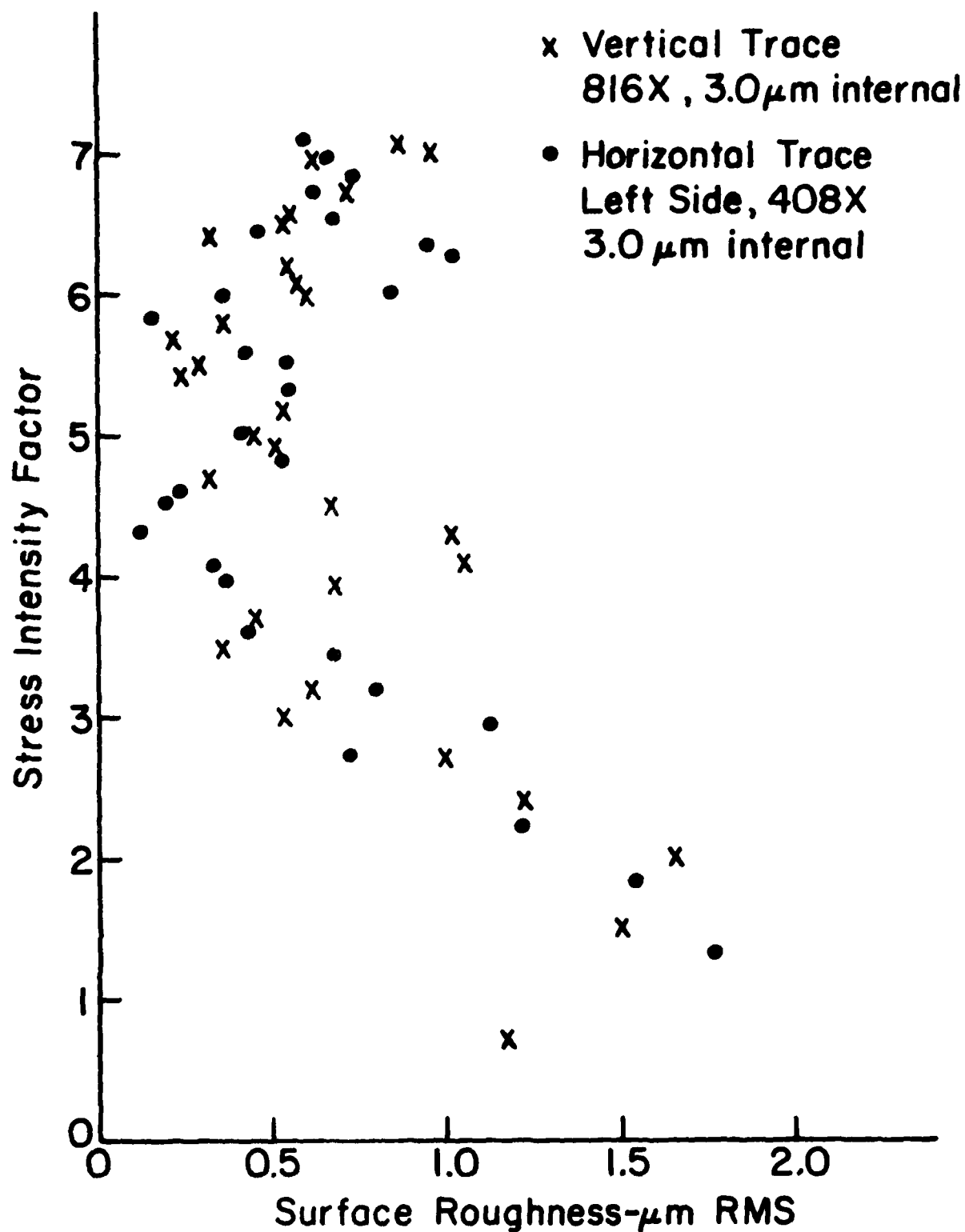
Figure 11. Stress intensity factor vs. surface roughness for vertical and horizontal traces (H.P. alumina Specimen R-45, $\sigma_F = 660$ MPa).

2. Plotting of surface roughness vs. K_I for several traces for
   purposes of comparison of one specimen with another or
   comparison of several traces radiating from one origin.

3. Correlation of surface roughness and PIF.

Improvements in the technique are needed. It has been more difficult
than expected to locate the fracture origin in the SEM at LeMont and to run
the trace directly through the fracture origin. These problems will no
doubt be more serious when the method is applied to unknown specimens instead
of the carefully selected and thoroughly studied specimens used so far.

Application of this method has been limited to the region from the
fracture origin to radii equal to four times the critical crack size. At
greater distances from the fracture origin the fracture surfaces of strong,
fine grained ceramics become very disturbed, the individual grains become
apparent and a wide variety of other fracture features are observed. No
doubt the relation between surface roughness and PIF is different in this
region and depends on the roughness introduced by these other features.

D. Summary of Fractographic Observations in H.P. Alumina

Fractures in H.P. Al_2O_3 originate at several types of preexisting flaws
including large surface and internal crystals, surface and internal pores,
machining flaws and poorly bonded regions[5]. The most distinctive fracture
feature near the fracture origins is the region of transgranular fracture.
In reflected light this region appears as a region of reflecting spots extend-
ing to radii where the apparent K_I values are about 6.6 MPa m$^{\frac{1}{2}}$ [11]. In
composite scanning electron micrographs of specimens with symmetrical crack
propagation and substantial subcritical crack growth, this region may appear

as two concentric bands of transgranular fracture separated by an irregular region with a higher fraction of intergranular fracture. Depending on the fracture origin flaw type and the extent of subcritical crack growth, there may be a narrow band of varying PIF between the flaw and the bands of transgranular fracture.

The two bands of transgranular fracture are near $K_I = K_{IC} = 4.2$ MPa m$^{\frac{1}{2}}$ and $K_I^* = 5.6$ MPa m$^{\frac{1}{2}}$. In our earlier work we attributed the increased transgranular fracture in these regions to the fact that K_I exceeded the K_{IC} value for fracture on $(\bar{1}\bar{1}26)$ planes at 4.3 MPa m$^{\frac{1}{2}}$ and exceeded the K_I value for fracture on $\{\bar{1}012\}$ surfaces and conchoidal fractures roughly parallel to $\{01\bar{1}4\}$ planes observed to fracture in preference to fracture on the basal (0001) plane at $\sim$5.6 MPa m$^{\frac{1}{2}}$ [4]. Based on this evidence, the first of these bands is considered to be the boundary at which the transition from the subcritical to critical crack growth occurs.

A few cases of linking of flaws have been observed in H.P. alumina. In most cases these involve linking of a sub-surface pore or inclusion with the surface. The region between the flaw and the surface typically fractures by transgranular fracture yielding a relatively dark, smooth appearing region in the scanning electron micrographs. Observation of wavy transgranular fracture as a mechanism of flaw linking confirms that this transgranular fracture is a significant subcritical crack growth mechanism.

At $K_I^* > 5.6$ MPa m$^{\frac{1}{2}}$, the PIF increases gradually to moderate values ($\sim$50%). The highest PIF values are not as high as those reported in our earlier work. At that time some transgranular fractures of individual grains were mistakenly classified as intergranular because of the very regular, well-defined appearance of the grains. Partly as a result of improved photographs, this problem was identified and remedied.

Surface roughness analysis has been used to supplement the usual optical and scanning electron microscopic observations. The direct brightness curves are useful for locating major features such as the crack branching boundary. The results of computerized SEM microtopography observations were correlated in some cases with the percent intergranular fracture. With further development, these methods may provide more objective means of analysis of fracture surfaces.

III. 96% ALUMINA

The 96% alumina is a commercial body* containing a (Ca,Mg,Al) silicate intergranular phase. The grain size of the alumina averages 4-6 μm. Most of the specimens tested during the present contract were extruded rods, 3 mm diameter, with ground surfaces. Before strength testing the specimens were annealed at 1500°C for one hour to relieve the residual stresses at the grinding flaws. The specimens tested during the previous contracts, some of which were studied during the present contract, were received with as-fired surfaces so that annealing was not required. Based on the results of Bansal and Duckworth[14] using the double torsion method the K_{IC} of the 96% Al_2O_3 was taken to be 3.8 MPa $m^{\frac{1}{2}}$. The present investigation included single edge notched beam and work of fracture (WOF) measurements intended to verify the reasonableness of this value. These measurements are presented and discussed in the next section.

Compared with the H.P. Al_2O_3, results for which are given in the previous section, the 96% Al_2O_3 body is less pure, weaker, coarser grained and has a lower K_{IC}. These differences caused differences in the observed fractographic features.

---

* ALSIMAG 614, 3M Company, Chattanooga, Tenn.

A. Work of Fracture and Critical Stress Intensity Factor of 96% Alumina

Freiman, McKinney and Smith[19] determined K_I vs. crack velocity for Region I (the region of the log K_I vs. log V curve in which V depends on environment) for nominally similar 96% alumina, apparently at 40% rh. A log K_I vs. log V curve is shown schematically in Figure 12. They determined K_{IC} as the value of K_I necessary to drive the crack at 10^{-4} $m \cdot s^{-1}$ obtaining 3.2 MPa $m^{\frac{1}{2}}$ and used this value together with their measured values of Young's modulus (303 GPa) to calculate the critical fracture energy which was 17 Jm^{-2}. As mentioned previously, Bansal and Duckworth[14] measured K_{IC} of the same material obtaining 3.8 MPa $m^{\frac{1}{2}}$. This value was used to estimate the location of the subcritical to critical crack growth boundary in the fractographic studies of this material reported here because this higher value was more in line with the accepted values for other alumina ceramics. Since this decision was made, other measurements have become available. Notable among these are data of Manz, Bubsey and Shannon[20] who obtained 3.4 MPa $m^{\frac{1}{2}}$ for single edge notch beams with narrow notches, 3.5 MPa $m^{\frac{1}{2}}$ for chevron notched beams and 3.7 to 4.7 MPa $m^{\frac{1}{2}}$ for short bar chevron notch specimens of varying size and chevron notch geometry.

In addition to the above results, WOF and single edge notch beam measurements were done in our laboratory. The single edge notch beam tests yielded two values that averaged 3.71 MPa $m^{\frac{1}{2}}$ [21]. This is equivalent to a critical fracture energy of 23 Jm^{-2}.

The WOF tests were done using chevron notched beam specimens as sketched in Figure 13A. The tests were performed by loading the specimens as indicated, using a known crosshead speed, and recording the load as a function of time. Using the known crosshead speed, the strip chart record was
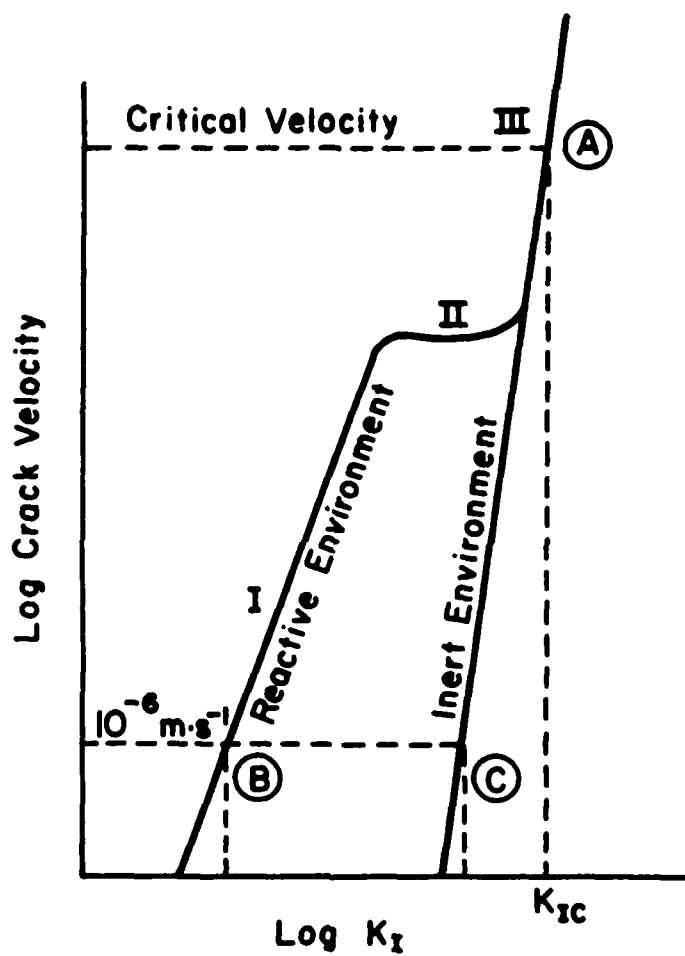
Figure 12. Schematic diagram showing variation
of crack velocity with K_I for
reactive and inert environments.

converted to a load vs. distance curve which, when integrated, yields the work done during fracture. Then, the projected cross sectional area of the fracture surface was measured and the work necessary to form a unit area of fracture surface, the work of fracture, was calculated.

Obtaining stable crack propagation was a substantial problem. In many cases the fracture was unstable yielding load vs. time curves similar to the one on the left side of Figure 13B. Several methods were used to improve stability including reduction of the cross sectional area remaining to be fractured, increasing the hardness of the loading system by using a higher capacity load cell, superficial etching of the material in the notch, reducing the crosshead speed, and so forth. Results for unstable cracks were rejected. A load vs. time curve for a stable crack is sketched on the right side of Figure 13B.

The work of fracture data are given in Table I. In these tests the crack velocities were 10^{-5}-10^{-6} m·s^{-1}. Freiman and coworkers[19] data indicate that a stress intensity factor of about 3.0 MPa m$^{\frac{1}{2}}$ should be necessary to achieve this crack velocity. The K_{WOF} values estimated from the WOF values average 3.4 MPa m$^{\frac{1}{2}}$, appreciably higher than 3.0 MPa m$^{\frac{1}{2}}$. The present K_{WOF} values were calculated using E = 324 GPa, a value obtained from both the manufacturers literature and verified by resonance measurements made in our laboratory on a dry pressed plate. This value was used rather than the value E = 303 GPa measured by Freiman and coworkers based on the weight of the available evidence. The relationship of the WOF to critical fracture energy in ceramics is not completely understood. However, if the WOF is equal to the fracture energy at the crack velocity of the WOF tests, as seems reasonable, the critical fracture energy and K_{IC} should be

Applied Load

Remaining Cross Section

Specimen Support Rollers
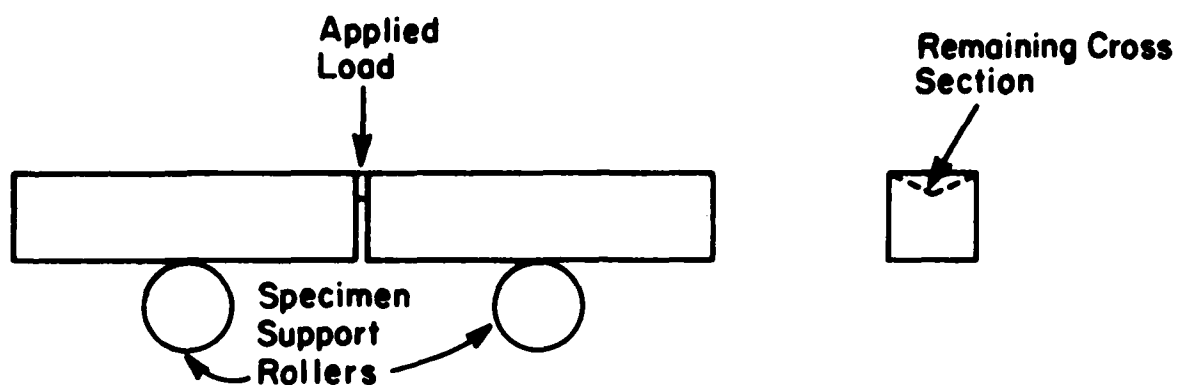
A. Specimen configuration (Scale 2X) and loading arrangement
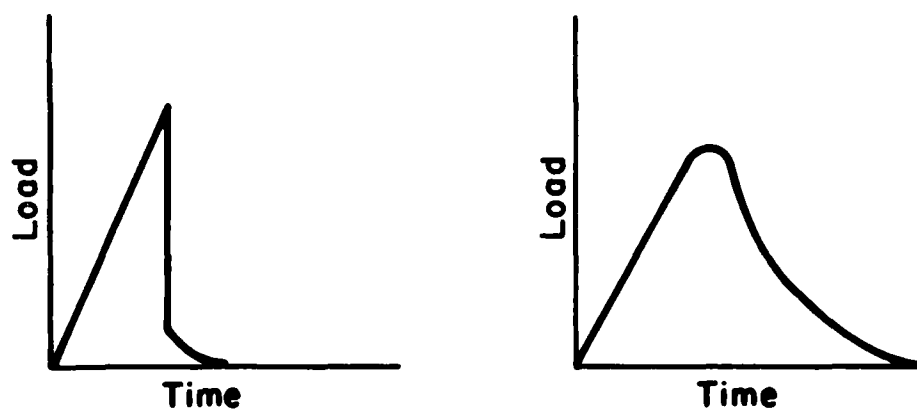
B. Load vs. time curves for unstable (left) and stable (right) fractures.

Figure 13. Work of fracture test, chevron notched beam (CNB) method.

TABLE I

Work of Fracture of 96% Al_2O_3 in the Laboratory Atmosphere

($\sim$40% rh)

Specimen Type	Specimen No.	Fracture Surface Area mm^2		WOF Jm^{-2}	K_{WOF}[†] $MPa\ m^{\frac{1}{2}}$
Dry Pressed Rectangular Bars (6 x 6 x 50 mm)	70-12		2.5	21.1	3.7
	70-13		3.0	14.9	3.1
	70-14		4.2	18.9	3.5
		Average	3.2	18.3 ± 3.1	3.4
Extruded Cylindrical Rods 3 mm diameter	(r-4)		2.2	15.0	3.1
	6		1.3	13.9	3.0
	7		1.2	20.4	3.6
		Average	1.6	16.4 ± 3.5	3.3
Extruded Cylindrical Rods 3 mm diameter	70		1.6	19.8	3.6
	E11*		1.6	19.8	3.6
	64		1.5	19.6	3.6
	81		1.1	14.8	3.1
		Average	1.5	18.5 ± 2.5	3.5

† Calculated assuming $K_{WOF} = (2E \cdot WOF)^{\frac{1}{2}}$

* Etched 30 min. in HF

appreciably higher than the estimates based on the WOF tests as was
observed in these experiments.

A further advantage of WOF tests is that they yield fracture surfaces
that are formed at approximately constant K_I and V. Therefore, by charac-
terizing these surfaces and then looking for similar features on other types
of fracture surfaces one can obtain an indication of the K_I acting at these
locations on the other fracture surfaces. As one might expect, based on the
stable conditions under which they are formed, these fracture surfaces have
quite a uniform appearance compared with fracture surfaces of specimens
from strength tests. In 96% Al_2O_3 the fracture is primarily transgranular
as shown in Figure 14. In addition, in this particular case, the grain
boundaries are more apparent than is usually the case.
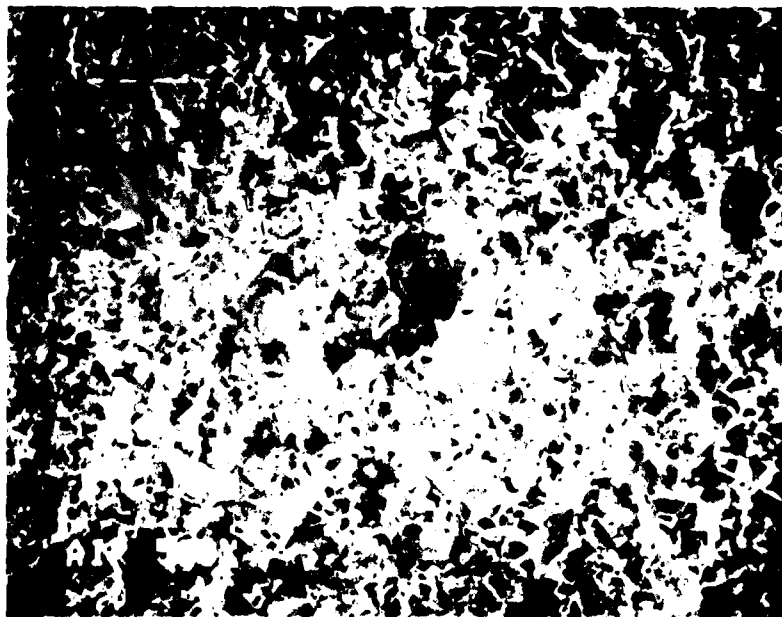
Figure 14.   Fracture surface of 96% Al_2O_3 work of
             fracture specimen fractured in air, 40% rh
             (Specimen #6, 500X).

The results presented above support the use of $K_{IC} = 3.8$ MPa m$^{\frac{1}{2}}$ for calculating the locations of critical crack boundaries. This is indicated especially by the fact that our single edge notch beam value is only slightly lower than the 3.8 MPa m$^{\frac{1}{2}}$ value originally measured by Bansal and Duckworth[14]. Also, if our WOF values at 10^{-6} m·s^{-1} are used to estimate the K_I necessary to drive the crack at the critical velocity, 10^{-4} or 10^{-2} m·s^{-1}, using the slope of the log V vs. K_I curve from Freiman and coworkers[19], a similar value is obtained.

There has been some uncertainty of the relationship of WOF values to the fracture energies determined from other fracture mechanics tests. The results in Table I suggest that the WOF values are simply the fracture energies for 10^{-6} m·s^{-1} in the laboratory atmosphere. This result can be explained with the aid of Figure 12 which is a schematic diagram of the variation of crack velocity with K_I for inert and reactive environments. It shows that one should expect the critical fracture energy values calculated from K_{IC} values (Point A) to be higher than fracture energy values for lower crack velocities determined by WOF tests (Point B). In our case these values are 23 Jm^{-2} and about 18 Jm^{-2}, respectively.

Effect of environment on WOF

In this part of the investigation WOF tests were done on 96% specimens in laboratory air, water and CCl$_4$. The WOF values and differences in fracture mode were compared. There have been earlier attempts to determine the effect of environment on fracture energy of alumina. Davidge and Tappin[23], using edge notched beam tests, found that the fracture energy of a 95% alumina body (HYALUMINA) decreased from 50 Jm^{-2} in silicone oil at 20°C, after degassing, to 43 Jm^{-2} in air and to 22 Jm^{-2} in boiling water. Although the fracture

energy in silicone oil seems very high, the K_{IC} value based on this fracture energy, 5.3 MPa $m^{\frac{1}{2}}$, is consistent with later observations of Evans[24] who determined log V vs. log K_I curves by the double torsion beam method in air (50% rh) and toluene. Therefore, it appears that 50 Jm^{-2} is the critical fracture energy for this 95% alumina and the 43 Jm^{-2} and 22 Jm^{-2} values are not critical fracture energies despite the fact that the single edge notched beam method is expected to yield such values. More recently Dailly, Hastings and Lach[25] compared the log V vs. log K_I curves for several aluminas in air, water and saline solution. If these results were interpreted in terms of the energy required to drive a crack at a particular velocity, the energies would decrease in the order in which the environments are listed. Thus, there is some evidence of an effect of environment on this fracture energy.

Some of the specimens used for WOF tests were chevron notched and then etched in 52% HF for 30 minutes after which the remaining acid was removed by washing for 30 minutes. The etching penetrated about 30 μm. This penetration is considered to be sufficient to relieve residual stresses at the notch and to provide an adequate starter crack but the fraction of the material that was etched was so small that it was not expected to affect the WOF data.

Other specimens were chevron notched and etched for 20 hours in 52% HF. This etching removed the siliceous intergranular phase[26], leaving the alumina-alumina contacts intact so that the WOF necessary to fracture these contacts could be measured. These specimens were also washed.

Still another batch of specimens was chevron notched but not etched. All of the specimens, etched and unetched, were heated to 250°C and held at this temperature to remove a fraction of the residual water adhering to the alumina.

38

As described previously, considerable difficulty was encountered in obtaining stable fractures. Load vs. time curves for two specimens are compared in Figure 15. The tendency toward stable fractures seemed to vary with environment. Stable fractures were eventually obtained in all these media but it was more difficult to obtain stable fractures in CCl_4 than in water, and more difficult in H_2O than in air. This problem was eventually solved by several remedies, mainly those mentioned previously. In addition, relatively large numbers of specimens were tested and results from tests with unstable load vs. time curves were rejected. In some cases, results from tests with semi-stable load vs. time curves were retained, if the values were no higher than those from tests with stable fractures.
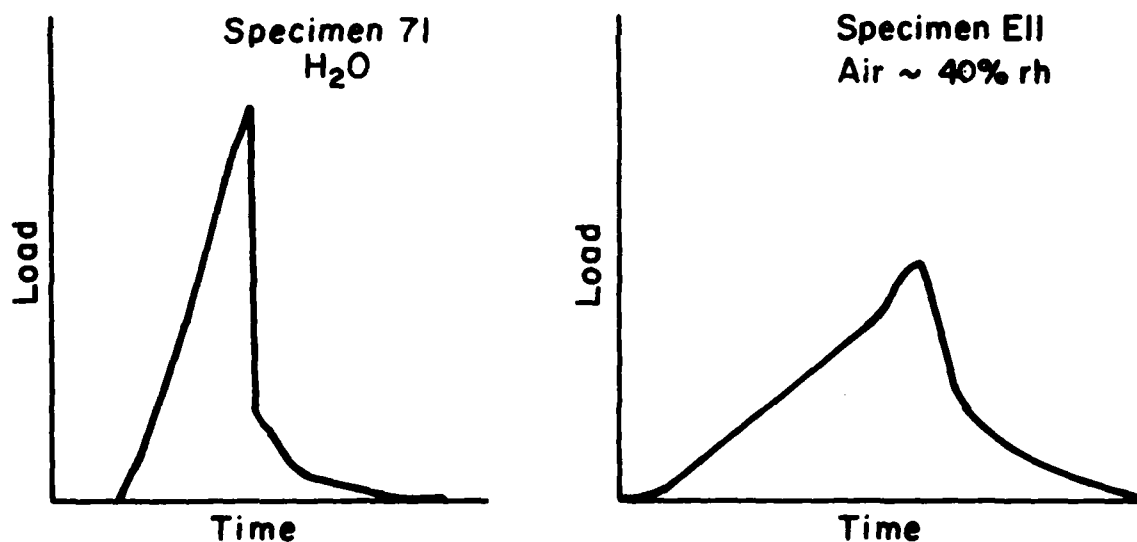
Figure 15. Load vs. time curves for unstable (left) and stable (right) fractures from WOF tests.

The results in Table II show small variations in WOF with environment. If we are correct in assuming that the WOF simply reflects the K_I value necessary to cause the crack to grow with the crack velocity of the WOF test, observation of the highest average WOF (23.0 Jm^{-2}) in the CCl_4 (essentially water free) environment is reasonable. The environments containing water (water, air at 40% rh) yielded slightly lower WOF values.

The fracture surfaces of specimens fractured in the three environments are illustrated in Figures 16-18. It is immediately apparent that the surfaces differ in important respects. The specimen fractured in air fractured to a very great extent by transgranular fracture. In both air and water, large areas of transgranular fracture were formed. In CCl_4 there is an increased amount of intergranular fracture and the areas of transgranular fracture are smaller than in water and air (40% rh). To provide a quantitative comparison, a grid was placed over each of these photographs and the mode of fracture in each grid space was determined and averaged.

The results in Table III show that environments containing water favor transgranular fracture and a relatively inert dry environment, CCl_4, tends to have more intergranular fracture. However, it should be remembered that, based on the results in Table II, the fracture in CCl_4 may have formed at slightly higher K_I which might account for the observed difference. These results can also be compared with the K_I vs. PIF curves presented in later sections which show the PIF for the likely range of K_I values at which the fracture surfaces of the specimens in Table II were formed.

The results of the WOF tests of the specimens etched for 20 hours are given in Table IV. They show that there was a substantial increase in the WOF as a result of etching.

TABLE II

WOF of 96% Al_2O_3 Fractured in Water, Air and CCl_4
Unetched and Lightly Etched Specimens

Environment	Specimen No.	Cross Sectional Area mm^2	WOF Jm^{-2}		$K_I^{\dagger \#}$ MPa $m^{\frac{1}{2}}$
Water	E12*	1.6	18.0		3.4
	E10	1.6	19.7		3.6
	50	2.8	28.4		4.3
	E25	1.2	19.9		3.6
	E28	1.1	22.8		3.9
			Average	21.8 ± 4.1	3.8
Air (~40% rh)	70	1.6	19.8		3.6
	E11	1.6	19.8		3.6
	64	1.5	19.6		3.6
	81	1.1	14.8		3.1
			Average	18.5 ± 2.5	3.5
CCl_4	61	1.0	22.3		3.8
	E21	0.9	23.2		3.9
	E22	0.9	23.5		3.9
			Average	23.0 ± 0.6	3.9

* Specimens designated by E were etched 30 min.

$K_I^{\dagger}$ was calculated assuming $K_I^{\dagger} = (2E \cdot WOF)^{\frac{1}{2}}$.

TABLE III

Fracture Mode for WOF Specimens Fractured in Three Environments

Specimen No.	Environment	Percent Intergranular Fracture
64	air (40% rh)	20
50	water	26.9
61	CCl_4	29.3

TABLE IV

WOF of 96% Al_2O_3 Fractured in Water, Air and CCl_4

Specimens Etched 20 Hours[#]

Environment	Specimen No.	Cross Sectional Area mm^2	WOF Jm^{-2}
Water	EE14*	3.1	36.8
	EE18	2.7	32.9
		Average	34.9 ± 2.8
Air (~75% rh)	EE15	1.7	55.3[+]
	EE17	2.8	41.8
	EE2	3.7	40.7
		Average	45.9 ± 8.1
CCl_4	EE1	3.7	39.7
	EE16	3.5	28.2
	EE19	1.4	24.8
		Average	30.9 ± 7.8

* Specimens designated by EE were etched for 20 hours.

$K_I^†$ was not calculated because the Young's modulus E of the etched material has not yet been measured.

+ EE15 was more completely etched leading to the higher WOF.
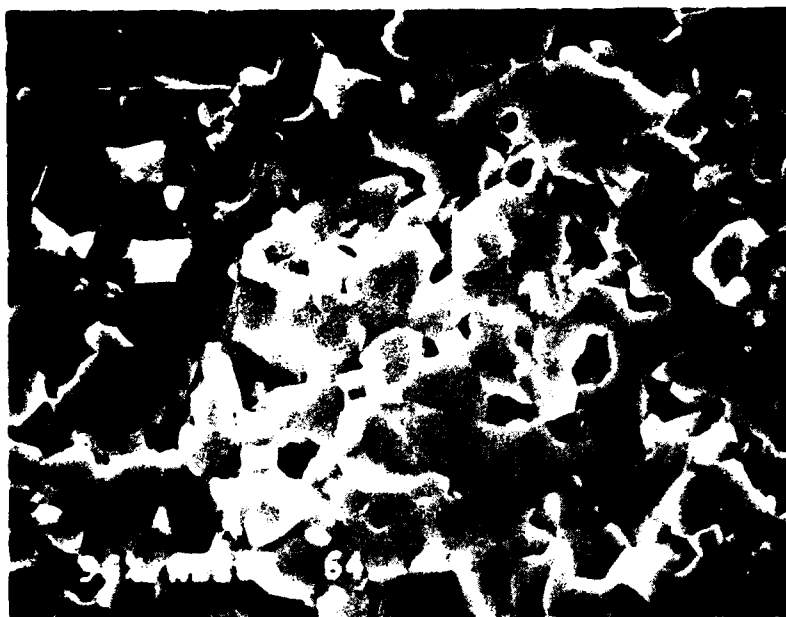
Figure 16. Fracture surface of WOF specimen tested in air, 40° rh (Specimen #64, 1000X).
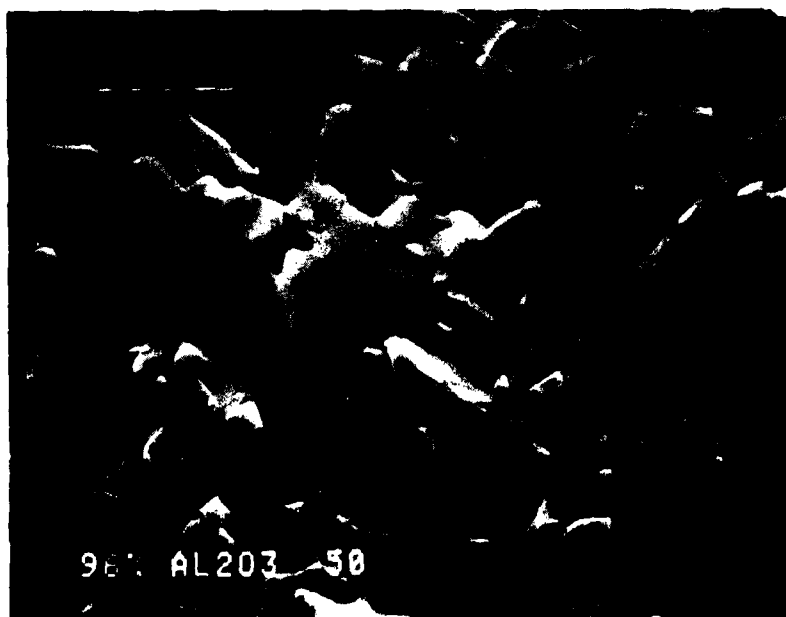
Figure 17. Fracture surface of WOF specimen tested in water (Specimen #50, 1000X).
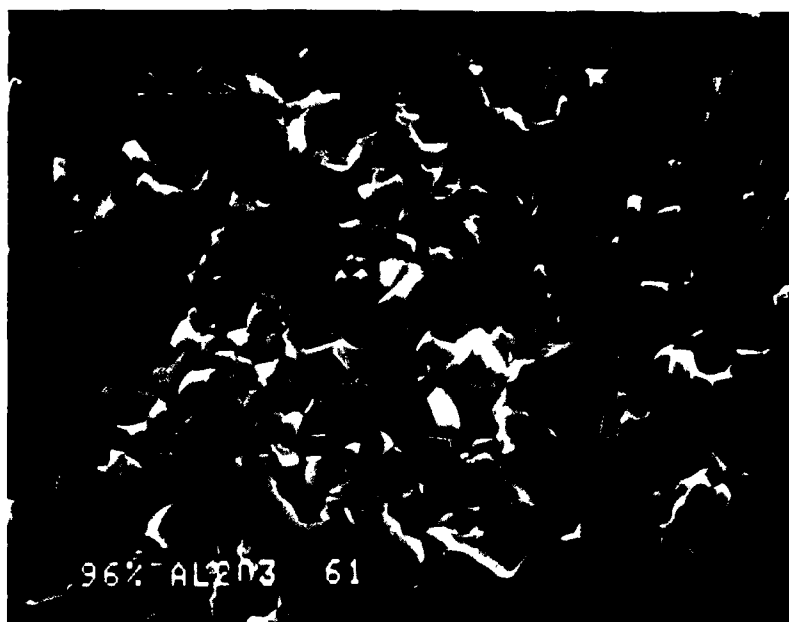
Figure 18.   Fracture surface of WOF specimen tested in
CCl₄ (Specimen #61, 1000X).

The fracture surfaces of specimens fractured in the three environments are illustrated in Figures 19-21. There is a substantial shift to intergranular fracture in the etched specimens compared with the unetched specimens. Of course, this observation should be expected because etching weakens the grain boundaries. These figures also show other important features. For example, all of the photographs show large numbers of microcracks. This observation suggests that the increased WOF in the etched material occurs as a result of enlargement of the process (microcracked) zone at the crack front in the etched material.

Comparing the photographs for the three environments shows that the apparent grain size for the CCl_4 environment is smaller than those for the other environments containing water. The apparent grain sizes were evaluated by the linear intercept method with the results given in Table V. This surprizing result indicates that the grain boundaries near the crack front are fracturing more easily in CCl_4 than they are in water containing environments. This explanation is also consistent with the observation of higher PIF for unetched specimens fractured in water contain'ng environments.

This procedure was repeated for additional specimens and, although the differences in apparent grain size were not as large, the averages varied as expected based on the first observations. Also included in Table V are apparent grain size measurements for unetched specimens fractured in the three environments. In this case the specimen fractured in CCl_4 also showed the smallest apparent grain size.

In addition to revealing interesting aspects of the effect of environment on fracture mechanisms, these results show that there are potential pitfall involved in the common practice of measuring grain sizes by analysis of fracture surfaces.

TABLE V

Variation of Apparent Grain Size with Environment
in Etched WOF Specimens

Treatment	Specimen No.	Environment	Apparent Grain Size	µm
Etched	EE16	CCl$_4$		3.9
	EE19			5.0
	EE1			5.1
			Average	4.7 ± 0.7
	EE15	Air(75% rh)		5.4
	EE17			4.2
	EE2			6.4
			Average	5.3 ± 1.1
	EE18	H$_2$O		5.7
	EE14			6.1
			Average	5.9 ± 0.3
Not Etched	61	CCl$_4$		6.2
	64	Air(40% rh)		8.5
	50	H$_2$O		8.1

46

Figure 19. Fracture surface of WOF specimen, etched 20 hours, tested in water (Specimen EE14, 1000X).

Figure 20. Fracture surface of WOF specimen, etched 20 hours, tested in air (75° rh) (Specimen EE2, 1000X).

Figure 21. Fracture surface of WOF specimen, etched 20 hours, tested in CCl_4 (Specimen EE16, 1000X).

The mechanism responsible for the increased grain boundary fracture for etched specimens fractured in CCl_4 remains in doubt. In water containing environments the water or water vapor in the connected pores may induce intergranular fractures over a more extensive process zone. This suggestion is consistent with the higher WOF values measured for air ($\sim$75% rh) and water environments. If, because of the absence of water, a less extensive process zone is formed in CCl_4 this may lead to higher stress concentrations acting along the main crack leading to a larger fraction of localized intergranular cracks on the fracture surface. In any case, it is interesting that weakening the grain boundaries by etching increased the work of fracture with greater increases occurring for environments containing water and the smallest increase occurring for CCl_4. Also, the reversal of the role of water from decreasing WOF in the dense bodies to increasing WOF in the etched bodies may help to explain some of the differences observed in earlier WOF measurements.

B. Relationship of K_I and Fracture Mode

The 96% Al_2O_3 specimens were fractured in several different environments including laboratory air at about 40% rh, silicone oil (DOW 200, 5 centistokes), water and CCl_4. The silicone oil is considered to be a relatively inert environment. Therefore, the data showing the relationship of K_I to the fracture mode will be presented first for a specimen fractured in silicone oil. Following that the results for specimens fractured in more or less reactive environments will be compared. Composite scanning electron micrographs of the fracture origin and the surrounding fracture surface, approximately 400 x 300 μm at 1000X, were prepared and analyzed.

The results selected for presentation represent a 96 Al O specimen (#150) fractured by 4-point loading on a one-inch span using a constant loading rate. The fracture stress was 500 MPa. The fracture surface is shown at relatively low magnification in Figure 22. The fracture origin is located at the top edge of the specimen and is indicated by an arrow. The composite photograph is presented in Figure 23 (in the attached envelope). The fracture origin was located mainly by means of the reflecting spots and by extending the river marks and other linear features to their intersection at or near the specimen surface. The flaw at the fracture origin is not well defined. The most reasonable explanation based on the large area of transgranular fracture at the origin is that the flaw is a small crack in the plane of the fracture surface. Such a crack is
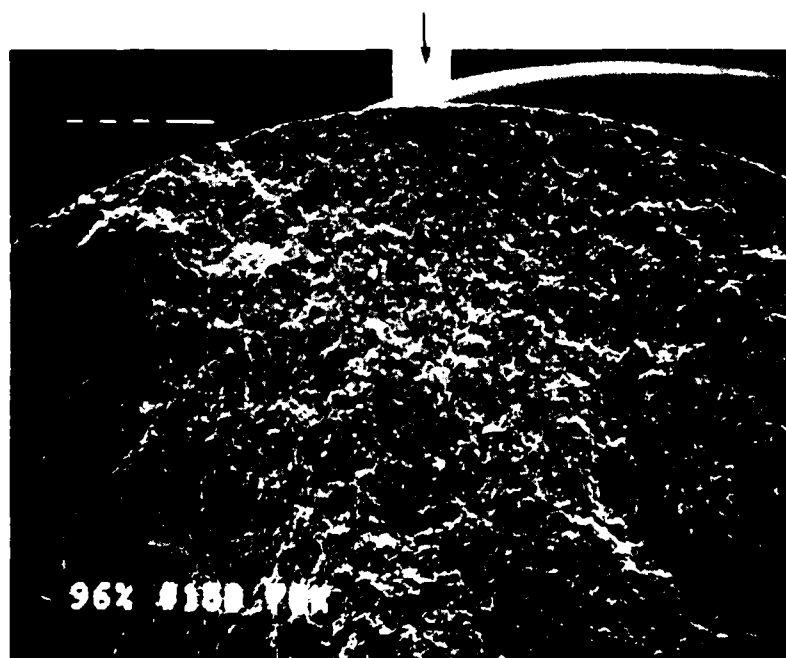
Figure 22. Fracture surface of a 96 alumina specimen fractured in silicone oil (Specimen #150, σ_f = 500 MPa).

likely to leave little evidence of its presence. As is typical for this
material, the fracture origin is surrounded by a region of primarily trans-
granular fracture. In reflected light such a region appears as a group of
reflecting spots[2]. At greater radii from the fracture origin the percent-
age of intergranular fracture increases. Also, an increasing percentage of
the transgranularly fractured grains contain what we have called linear
features. Many of the linear features are river marks[18] but they also
include ordinary cleavage steps, striations, cracks, and a variety of
unidentified features.

As in the case of H.P. Al_2O_3, a grid was placed over the composite
photograph and the fracture mode was evaluated for each grid space. The
grid spaces were 2.5 μm on a side at 1000X so that the grains average about
two times the grid size. It is immediately apparent that the large areas of
transgranular fracture are many grains in size but reveal little evidence
of grain boundaries. Therefore, it is clear that the wavy transgranular
fracture propagates from grain to grain with little disturbance at the grain
boundaries. The fracture surface was evaluated in a path 50 μm wide and
about 250 μm long extending perpendicular to the surface from the fracture
origin. Each space was evaluated to determine whether it was intergranular
or transgranular and, if transgranular, whether or not linear features were
present. The results were averaged for each row and presented in Figures
24 and 25.

As we observed previously[2], the 96% Al_2O_3 body usually shows a greater
proportion of transgranular fracture near fracture origins than the H.P.
Al_2O_3. This difference is attributed to the increased grain size of the 96%
Al_2O_3 which increases the energy required for intergranular fracture because

Figure 23. Composite scanning electron micrograph of fracture surface of a 96% alumina specimen fractured in silicone oil (Specimen #150, σ_F = 500 MPa, 1000X).

Stress Intensity Factor—MPa $m^{1/2}$

Distance from Surface—μm

0 — 0

3.8 — 35.6

4.50 — 50

6.37 — 100

7.80 — 150

9.00 — 200

Fracture Origin

Stre:.s Ir

Dista

9.00 — 200

10.06 — 250

96% 8158 1000X
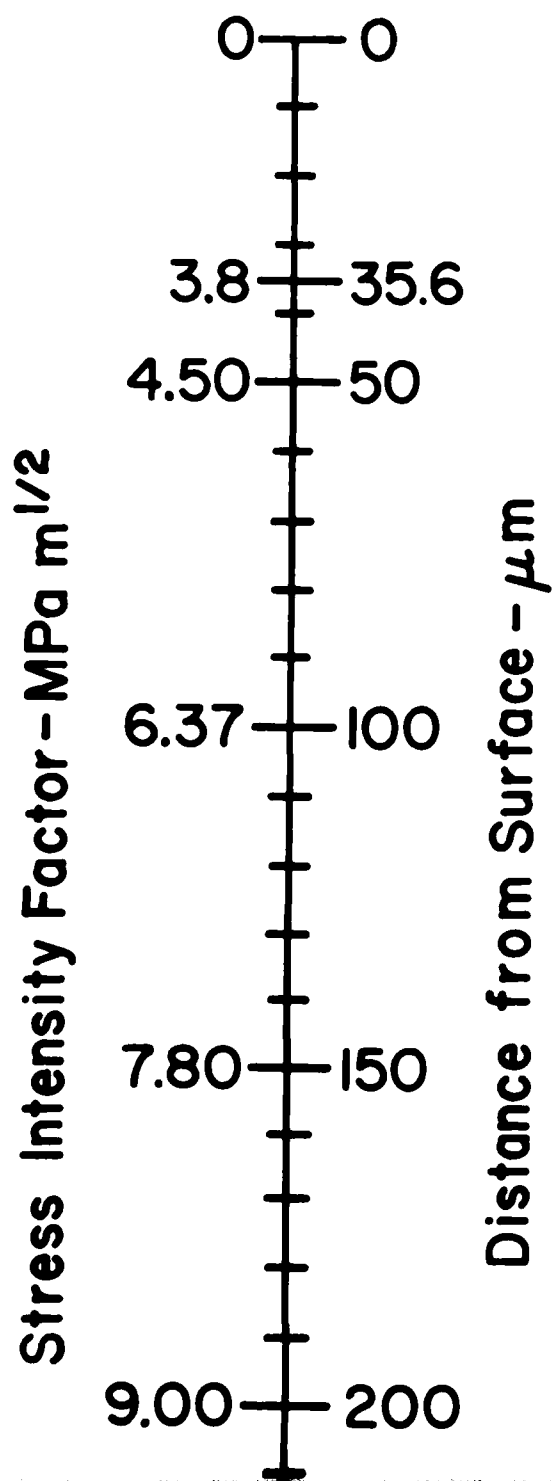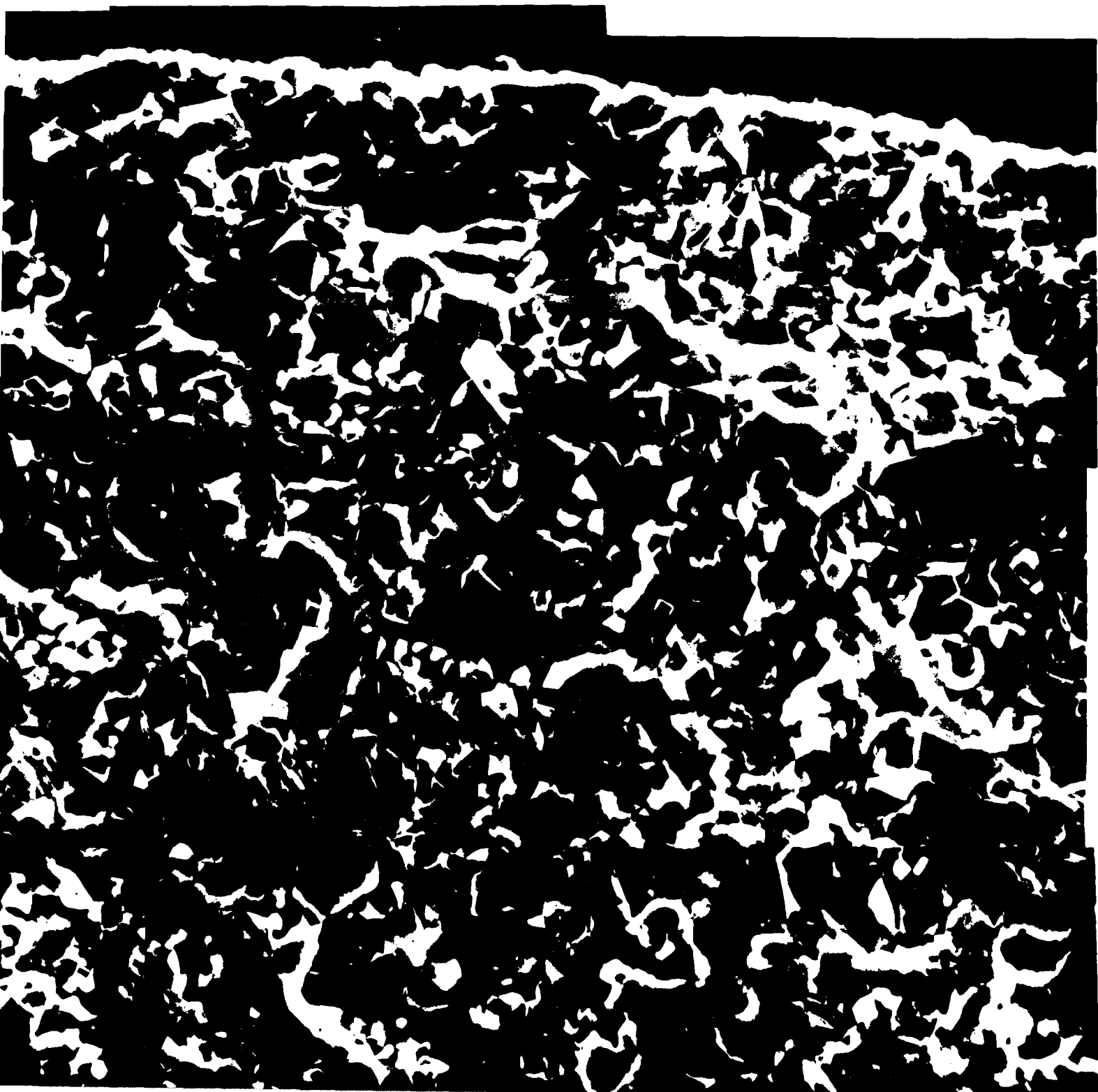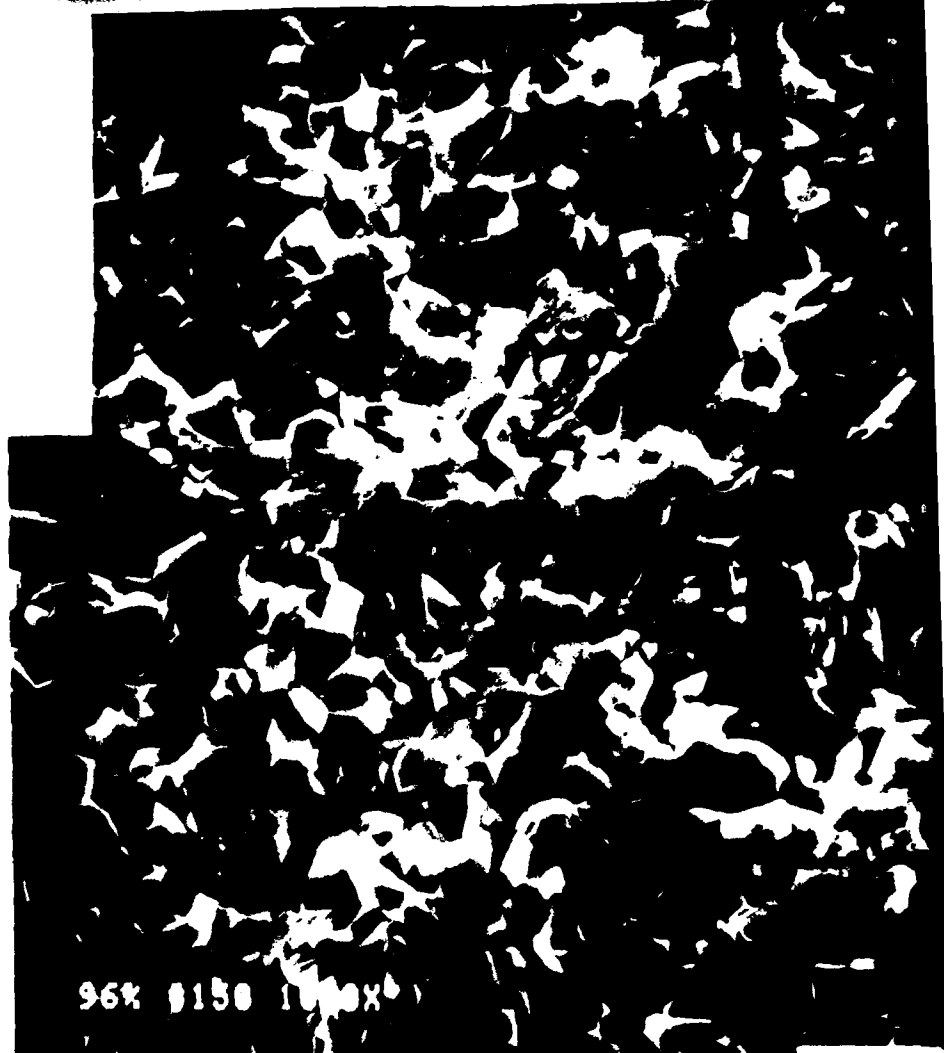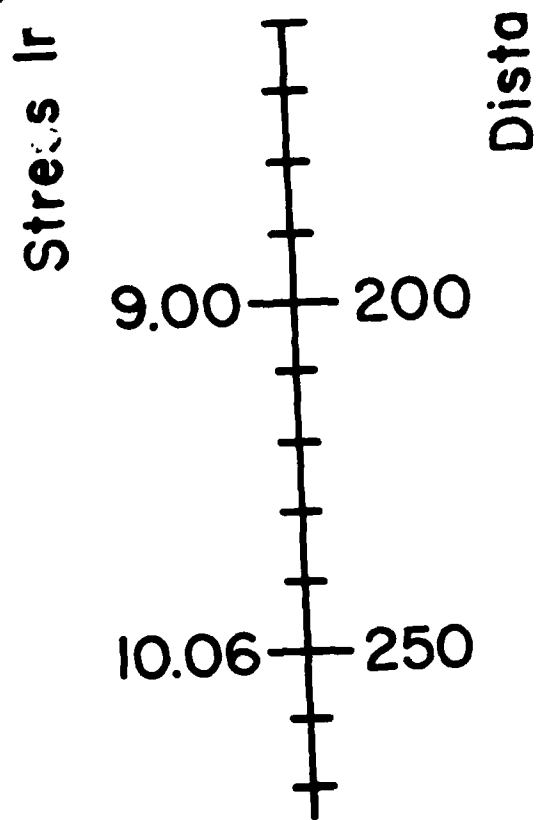
Figure 23. Composite
in silicone
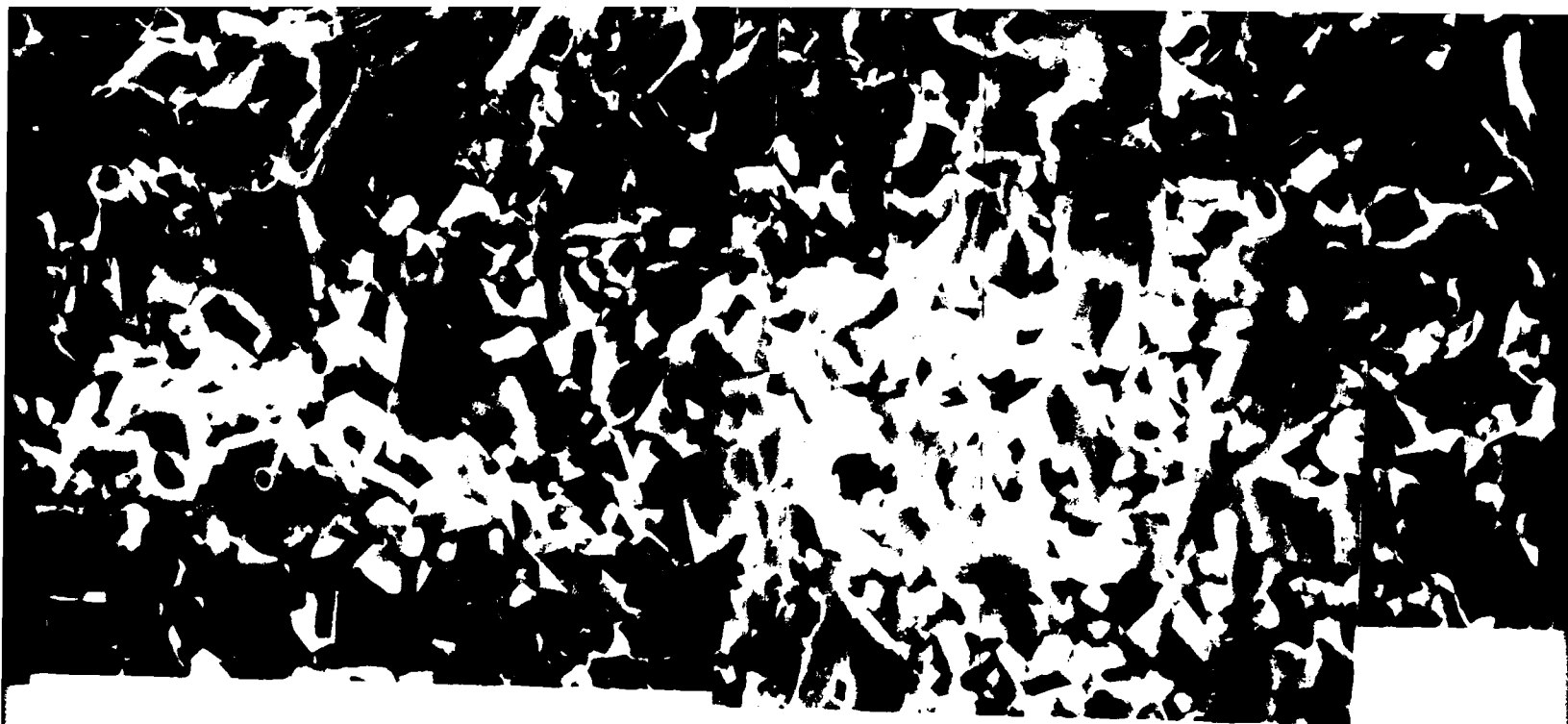
osite scanning electron micrograph of fracture surface of a cone oil (Specimen #150, σ_F = 500 MPa , 1000X).
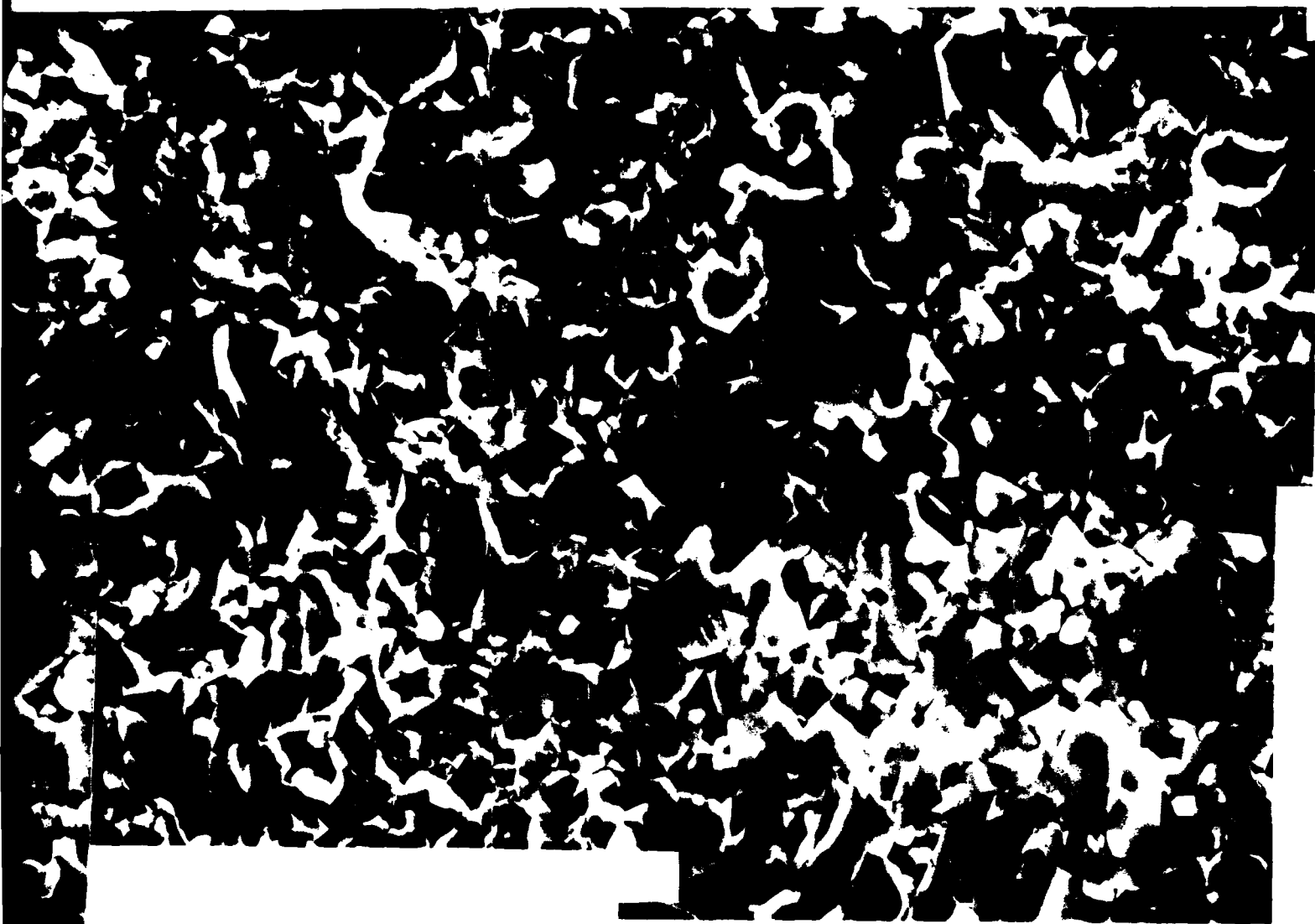
urface of a 96% alumina specimen fractured
)X).
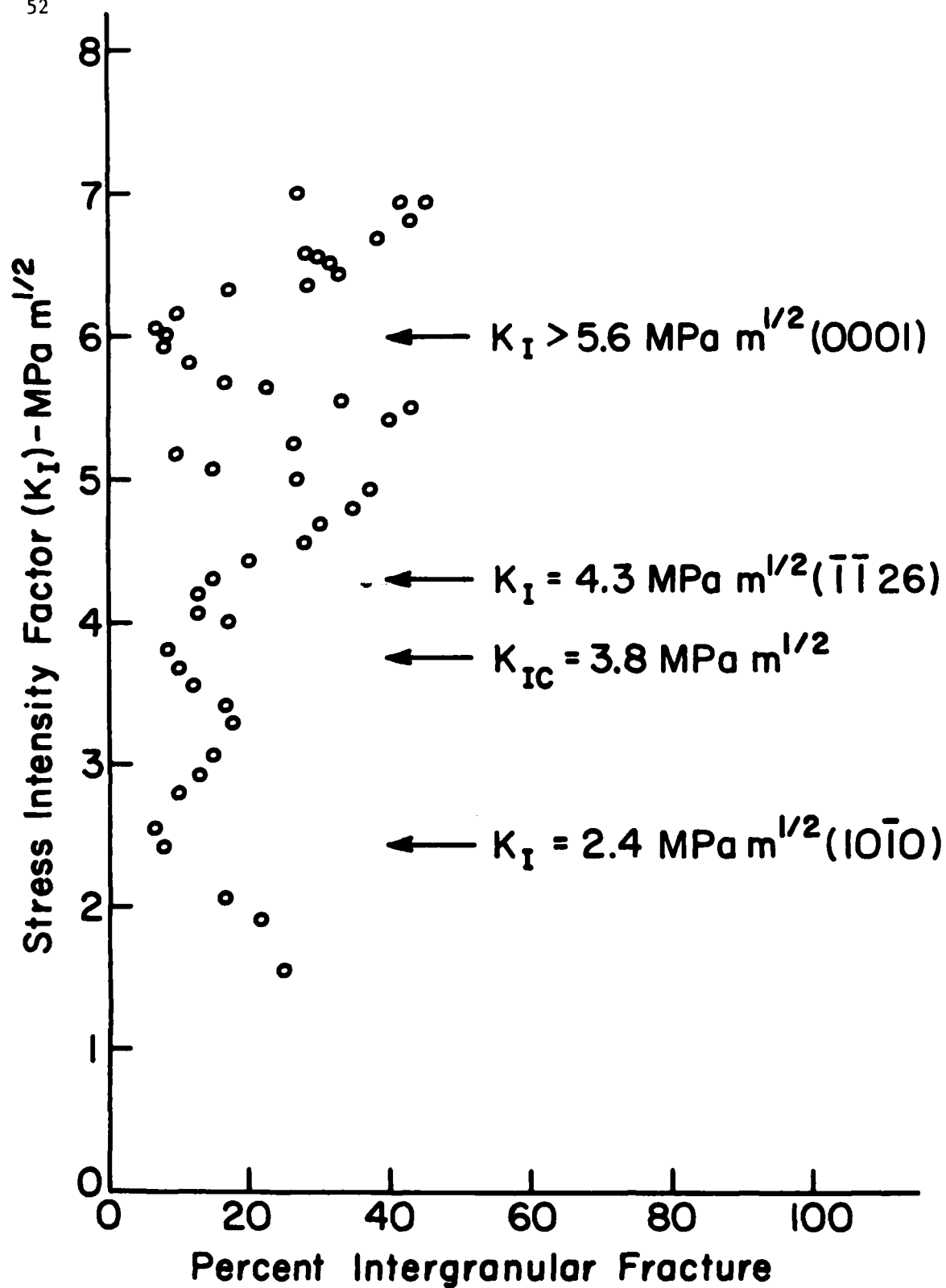
Figure 24. Stress intensity factor vs. PIF, 3-row running averages (96% alumina Specimen #150 fractured in silicone oil, σ_F = 500 MPa).
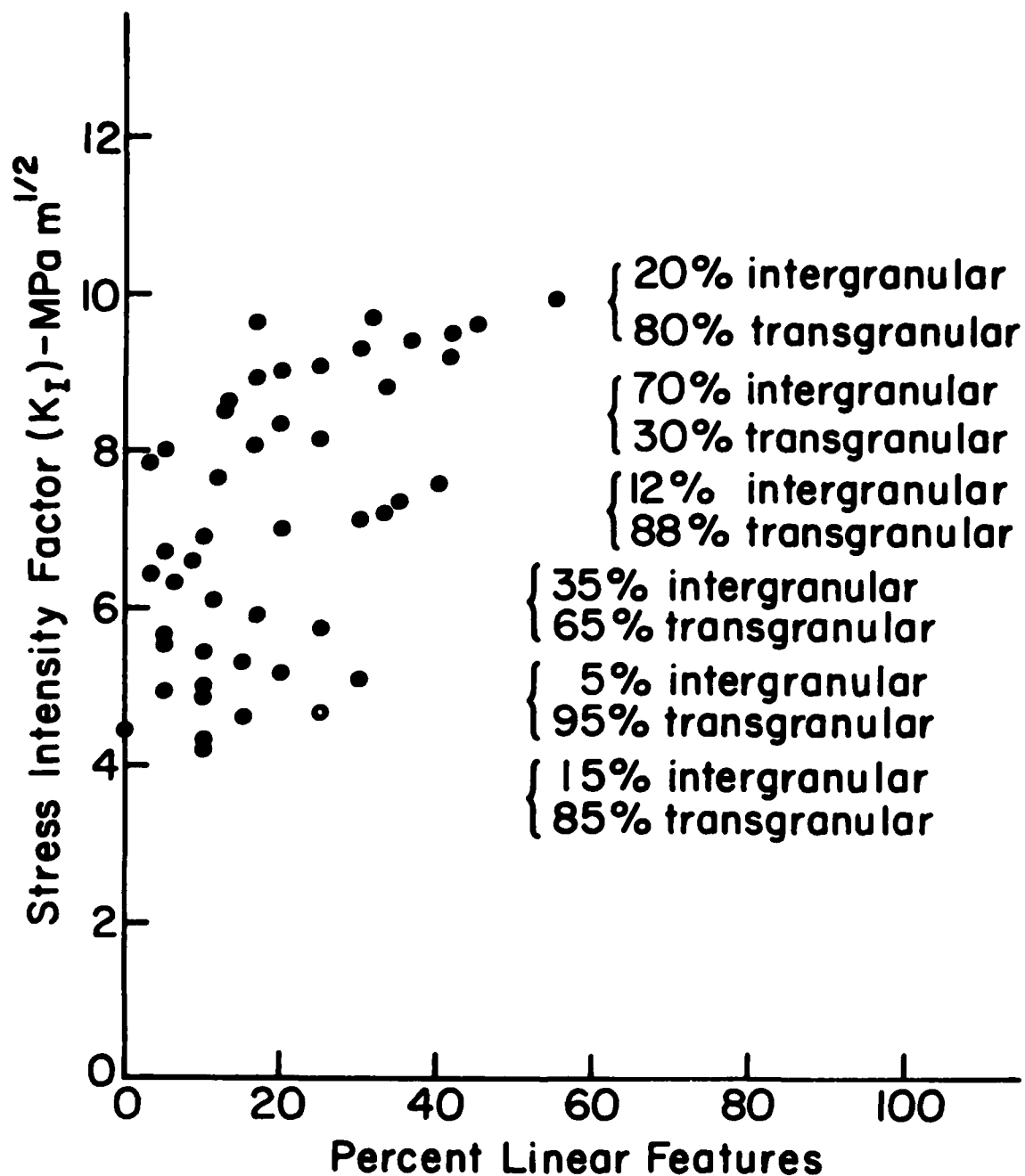
Figure 25. Stress intensity factor vs. percent linear features, single row averages (96% alumina Specimen #150 fractured in silicone oil, σ_F = 500 MPa).

of the increased surface area formed, the increased departure of the crack

from the average plane and the increased irregularity (bluntness) of the

crack front for intergranular fracture compared with transgranular fracture.

In overall terms PIF varies with K_I as expected based on earlier obser-

vations. Figure 24 shows minima near $K_I = 2.4$ MPa $m^{\frac{1}{2}}$ which is the estimated

K_{IC} for fracture on $\{10\bar{1}0\}$ planes in sapphire, 3.8 MPa $m^{\frac{1}{2}}$ which is the K_{IC}

of the polycrystalline body, 4.3 MPa $m^{\frac{1}{2}}$ which is the estimated K_{IC} for frac-

ture on $\{\bar{1}\bar{1}26\}$ planes in sapphire and 5.6 MPa $m^{\frac{1}{2}}$ which is the K_I at which

Wiederhorn[4] was unable to induce transgranular fracture on the (0001)

plane in sapphire. Instead he observed fracture alternating between $\{\bar{1}012\}$

rhombohedral surfaces and conchoidal surfaces roughly parallel to the $(01\bar{1}4)$

plane. It is interesting that most of the K_I vs. PIF curves show a double

minimum in this K_I range so that one can speculate that the polycrystalline

body is responding in a manner similar to the sapphire.

Figure 25 shows that the percent of the fracture surface with linear

features (PLF) increases strongly with K_I. Only the transgranularly frac-

tured grains show these features. These data show no linear features at

$K_I < 4$ MPa $m^{\frac{1}{2}}$ but small areas with linear features usually are observed at

$K_I < 4$ MPa $m^{\frac{1}{2}}$ in other specimens so that the onset of these phenomena is

not usually as abrupt as is indicated by the figure.

Between $K_I = 4$ and $K_I = 10$ MPa $m^{\frac{1}{2}}$ there are several maxima and minima

in PLF. These maxima and minima occur in response to variations in PIF.

When PIF is high PLF must be low because only transgranularly fractured

grains have linear features. The percentages of intergranular and trans-

granular fracture for one or two rows at each of the maxima and minima are

indicated in brackets on the figure. These results show among other things,

that the percentage of the area of transgranularly fractured grains showing linear features increases strongly with K_I. Taking the values at the three maxima we find that:

First maximum $K_I \simeq 4.6$ MPa $m^{\frac{1}{2}}$ 32% have linear features

Second maximum $K_I \simeq 7.6$ 45% "   "   "

Third maximum $K_I \simeq 9.9$ 69% "   "   "

It is clear that this increase in the areas of transgranularly fractured grains showing linear features can be a valuable tool during failure analysis for estimating the stress intensity factor or apparent stress intensity factor acting at various locations on the fracture surface.

Effect of environment on fracture mechanisms

As implied by the dependence of crack velocity on K_I and environment, the strengths of many ceramics are time dependent in chemically active environments. This characteristic can be demonstrated by so-called delayed fracture tests in which specimens are subjected to dead weight loads and the time to failure is measured. The environments investigated in this program included laboratory air, water and CCl_4*. Originally, the choice of environments was based on the work of Cuthrell and coworkers[22] who found that fractures during drilling tests in hydrogen poor environments were less "brittle" than fractures in hydrogen rich environments. Some uncertainty is introduced by the fact that, in drilling, the failure probably occurs by mixed mode stresses because of the compressive component of loading, whereas in the present tests failure occurs in tension (Mode I). In any case, as indicated in the WOF tests, there is substantial reason to expect variations in fracture mechanisms as a result of exposure to various environments.

---

* Baker analytical grade dried over $CaSO_4$.

The flexural strengths of thermally annealed 96% alumina ceramic rods tested by four point loading on a one inch span are higher when measured in "water-free" environments than they are when measured in water or in air at various humidities. In the present case, the flexural strengths averaged 466 MPa in CCl_4 and 434 MPa in water. These strengths are higher and the strength difference is smaller than we would have expected based on our earlier measurements for environments with various water contents[27,28]. The results of the delayed fracture tests are given in Figure 26. Again the strengths are higher and the strength differences for the two environments are smaller than we would have expected based on our earlier results. Nevertheless the differences are substantial.

Effect of environment on fracture features for fractures propagating from inherent flaws

In the section on WOF tests, fracture features were characterized for fractures propagating at almost constant K_I values from large artificially induced flaws. In the present section, the characteristics of fracture surfaces formed by cracks propagating from small inherent flaws in various environments and under strongly increasing K_I are described. The principal comparisons were made for specimens fractured in water and CCl_4. It is impractical to present all of the photographs and other data on which these comparisons are based. Therefore, detailed photographs will be presented for one specimen fractured in each environment together with tabulated data for a few other specimens. This information will be used to compare the fracture features of specimens fractured in the two environments. To compensate for differences in subcritical crack growth and fracture stress the comparisons are made at approximately equal K_I values.
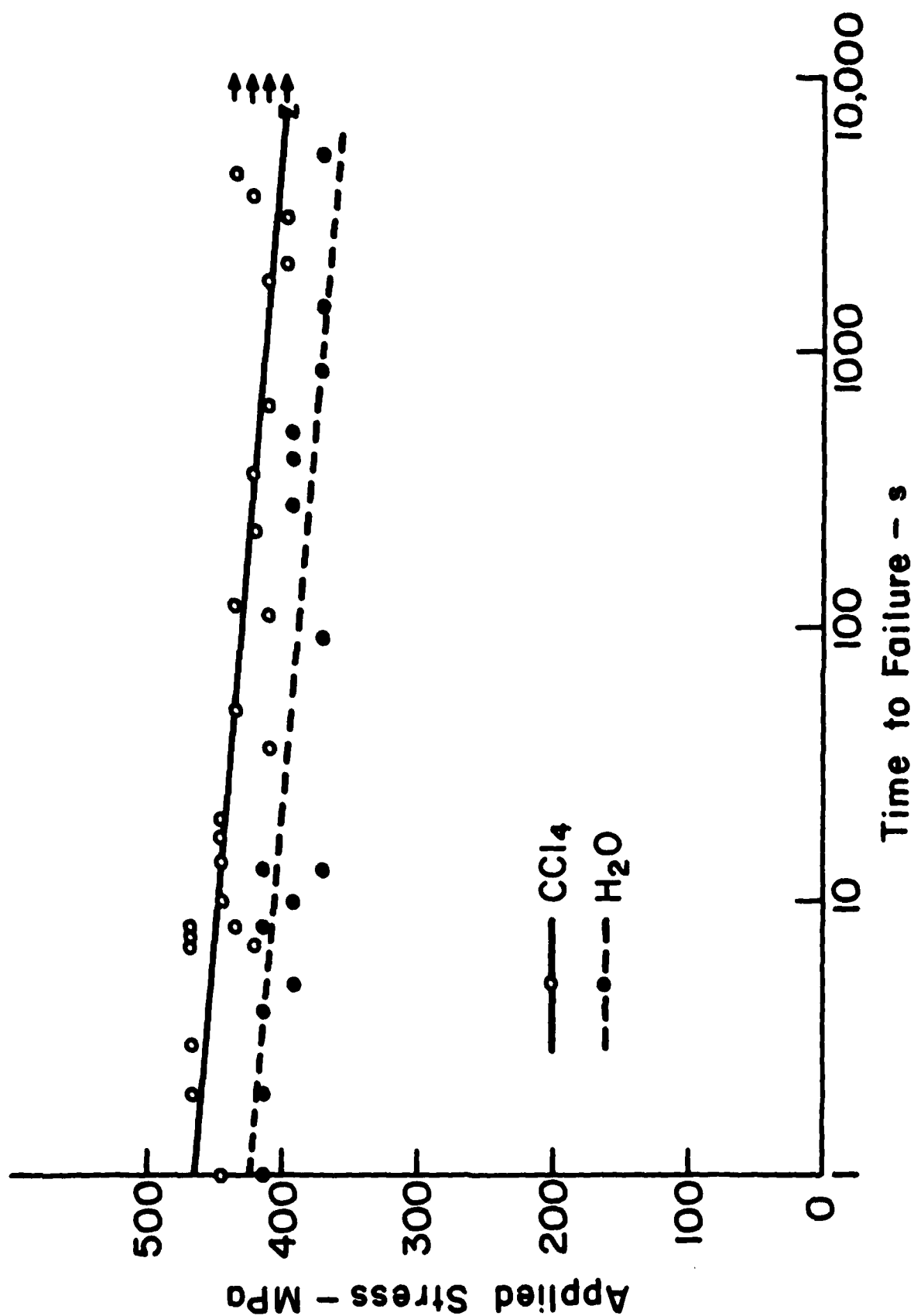
Figure 26. Applied stress vs. time to failure for 96% alumina tested in CCl$_4$ and H$_2$O.

57

Fracture in CCl$_4$, Specimen #8

Specimen #8 was fractured by loading in flexure at a linear loading rate. The loading rate was low so that the specimen fractured in about one minute. The composite photograph of the fracture surface of Specimen #8 is given in Figure 27. The darker round spots on the left and right sides of the composite photograph are artifacts caused by aging of the conducting coating used to prevent charging of the alumina surface. This specimen fractured at a relatively high stress, 509 MPa, from a surface pore ∿18 µm deep. Assuming a sharp crack at the pore boundary, K_I is less than 2.7 MPa m$^{\frac{1}{2}}$ at the pore boundary. River marks and other linear features point back to the pore indicating that it is the fracture origin. The fracture origin is surrounded by a region of wavy transgranular fracture. As explained previously, part of this region near the fracture origin is a region of subcritical crack growth. The critical crack is approximately 44 µm deep. As observed previously, the critical crack boundary is marked by a series of pullouts and projecting grains. At greater radii from the fracture origin the so-called linear features are observed with increasing frequency.

The shape of the area of wavy transgranular fracture, the subcritical crack growth boundary and the shapes of contours defined by equal frequency of linear features all indicate that the crack propagated at lower K_I values to the right than to the left. These observations suggest that the crack propagating from the surface pore linked up with another flaw to the right. There is a small pore located 35 µm to the right of the fracture origin and 10 µm below the surface. The river marks below this pore show that the crack propagated down from the pore. It may be that, when this crack grew to the point that it could overcome the resistance of the projecting grain to the

Figure 27. Composite scanning electron micrograph of the fracture surface of a 96% alumina specimen fractured in CCl_4 (Specimen #8, σ_F = 509 MPa, 1000X).

-250   -200

10.24   9.16

0 — 0

Intensity Factor—MPa m$^{1/2}$

4.58 — 50

6.58 — 100

7.93 — 150

from Surface — μm

Distance from Fracture Orig

-150   -100   -50   0

7.93   6.48   4.58   0

Stress Intensity Factor - M

Fracture

Fracture Origin- μm

0   +50   +100   +150   +200

0   4.58   6.48   7.92   9.16

ity Factor-MPa m$^{1/2}$

Fracture Origin

+200   +250

9.16   10.24
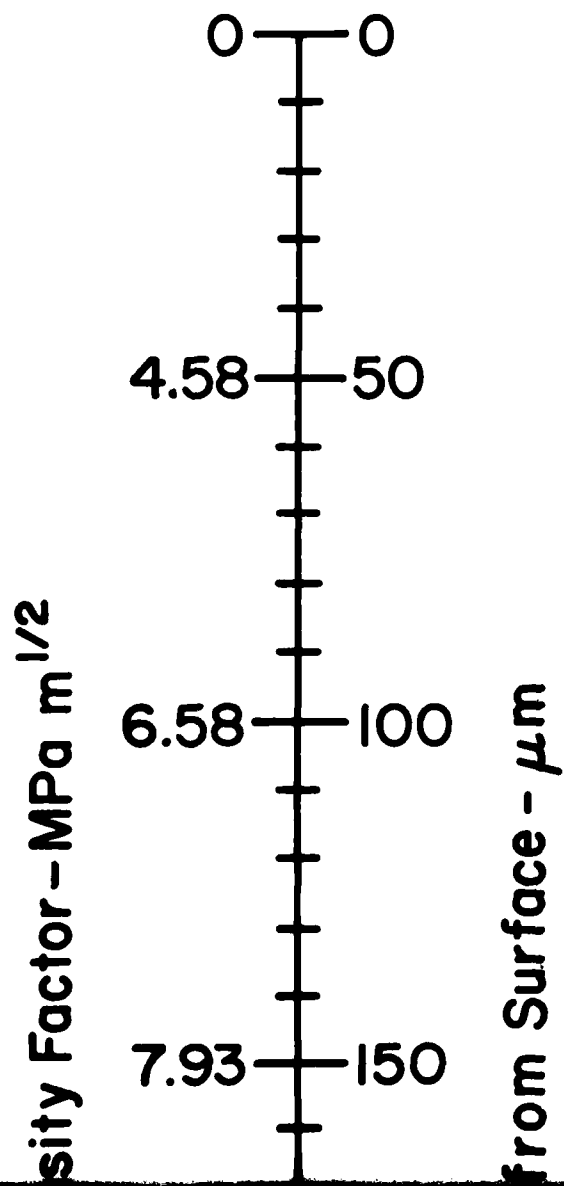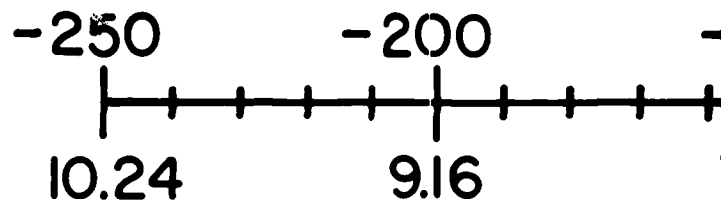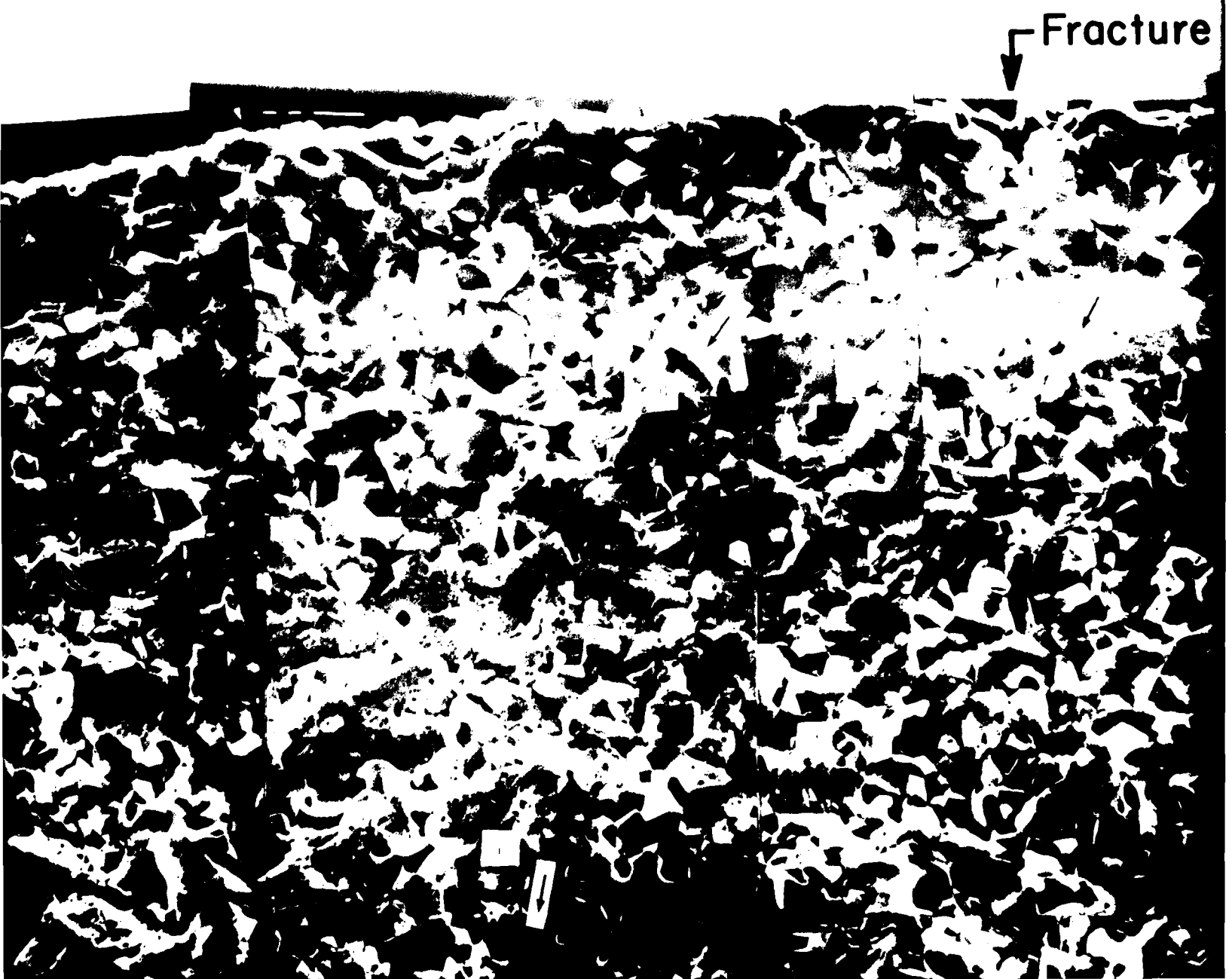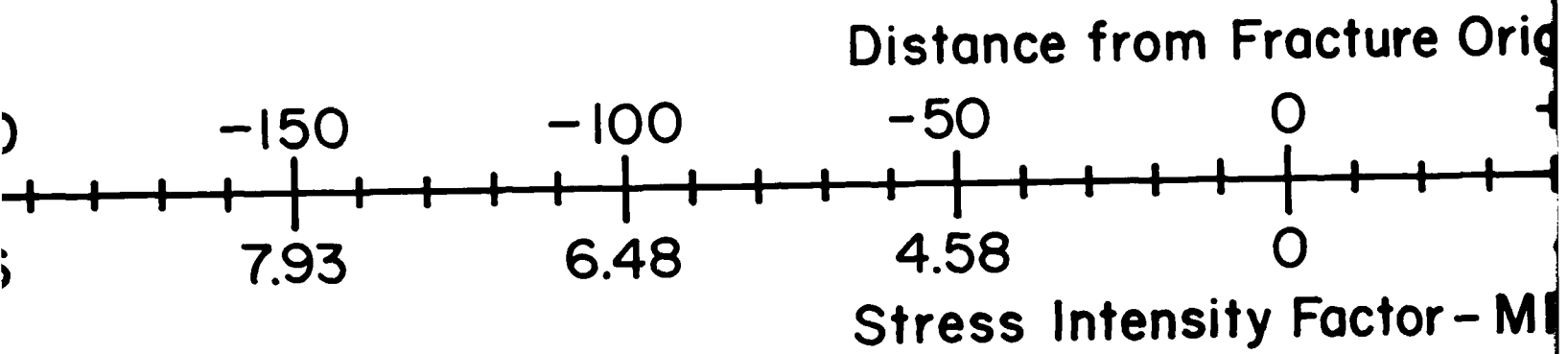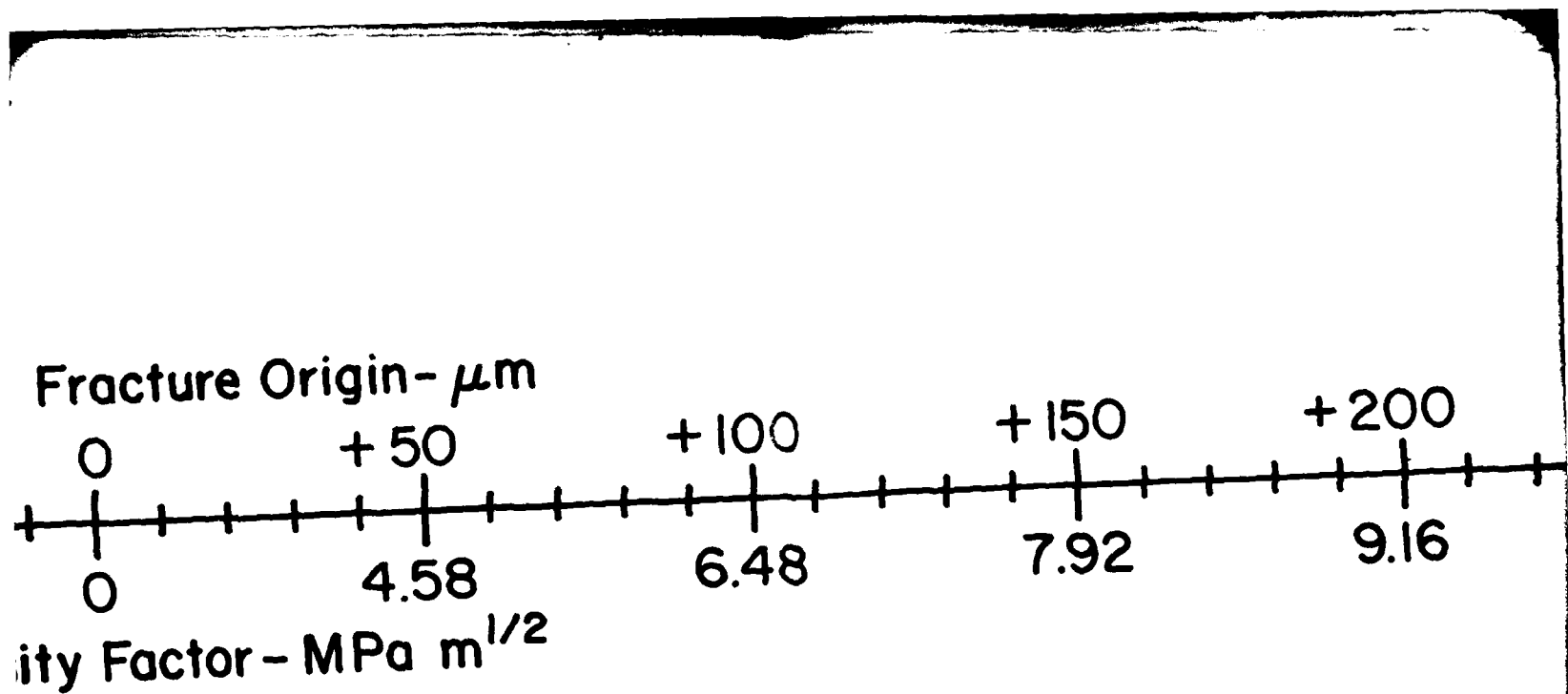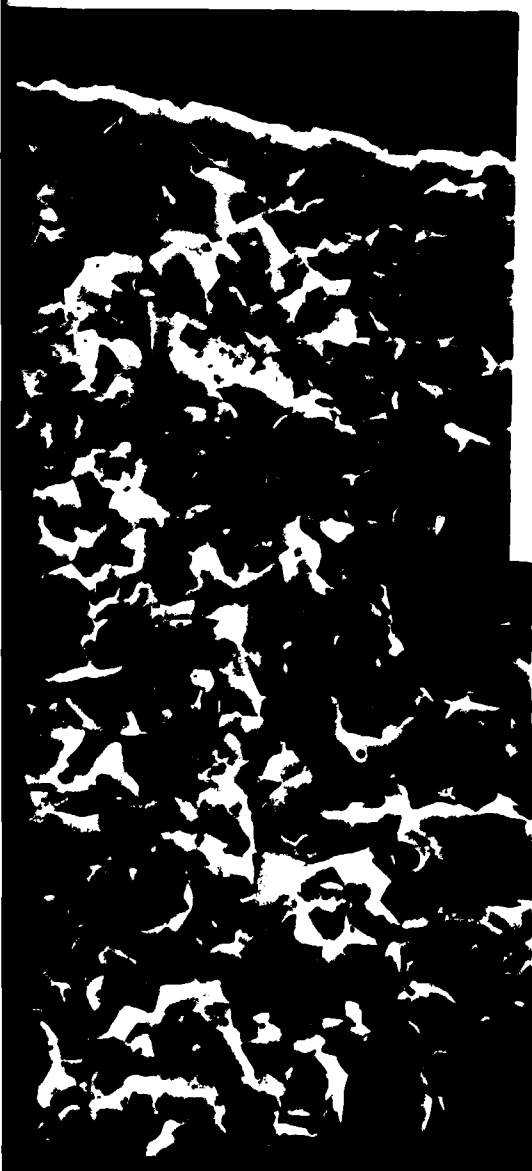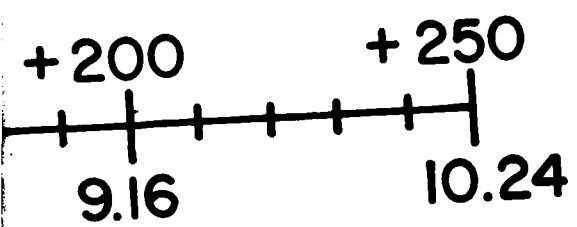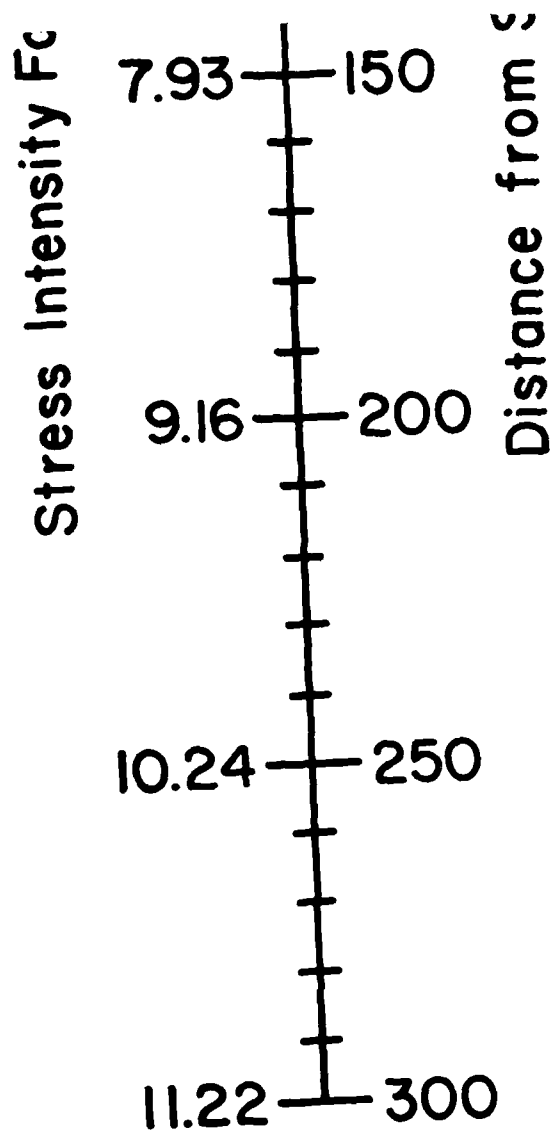
Figure 27. Composi
in CCl4
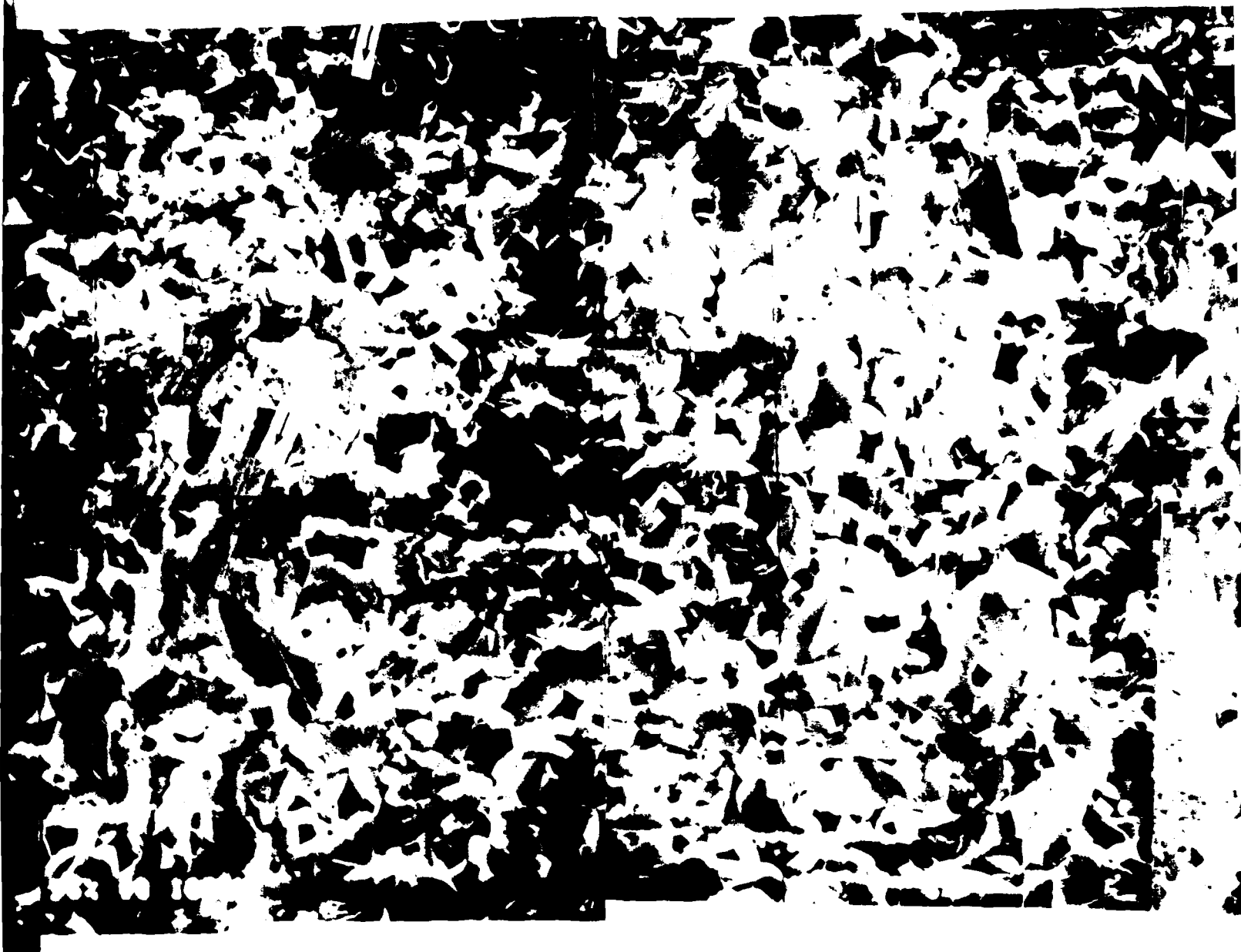
posite scanning electron micrograph of the fracture surfac
CI$_4$ (Specimen #8, σ_F = 509 MPa , 1000X).
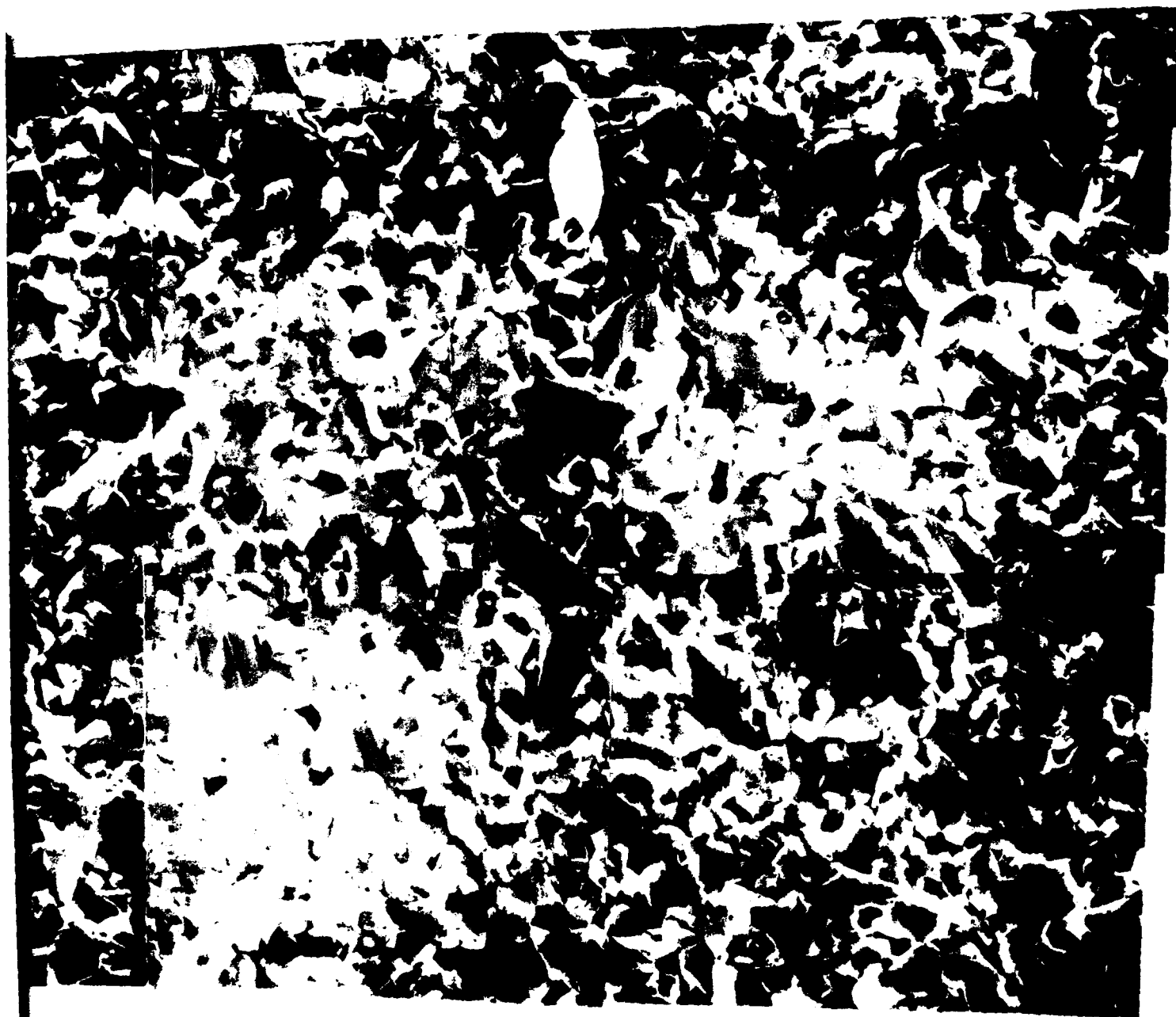
ure surface of a 96% alumina specimen fractured

left of the pore, the two cracks linked up. The calculated K_I value at this critical flaw boundary is 4.3 MPa $m^{\frac{1}{2}}$, assuming a semi-circular crack.

The K_I vs. PIF was determined for this specimen by the method described previously with the results shown in Figure 28. The curve shows minima in PIF at K_I values of 4.0, 5.6 and 6.0 MPa $m^{\frac{1}{2}}$, values close to the values observed in other cases. There are no very substantial differences in fracture mode that would indicate an effect of environment on the fracture mode.

The relationship of the percentage of the surface area consisting of transgranularly fractured grains with linear features (PLF) to the K_I acting at the crack front was determined by a similar method. The PLF increases strongly with K_I as shown in Figure 29. The PLF increases from close to zero at K_I = 3 MPa $m^{\frac{1}{2}}$ to about 60% at K_I = 6 MPa $m^{\frac{1}{2}}$. Subjectively, the boundary of the region containing linear features is at about this K_I value. It is interesting that this subjectively observed boundary is close to the maximum concentration of these grains.

The characteristics of the linear features in this specimen were studied extensively by stereo scanning electron microscopy mainly because the features were so varied in appearance and so well defined. The areas at which photographs were taken are labeled with letters on the composite photograph and the photographs are presented in Figures 30-35.

The photograph of area A which fractured at K_I = 3-4 MPa $m^{\frac{1}{2}}$ shows mainly transgranular fracture with only a few linear features which appear to be river marks. The areas of transgranular fracture are much larger than the grain size.

Area B was subjected to much higher K_I, perhaps up to 6.5 MPa $m^{\frac{1}{2}}$ and the fracture features show the response to this increase, especially the
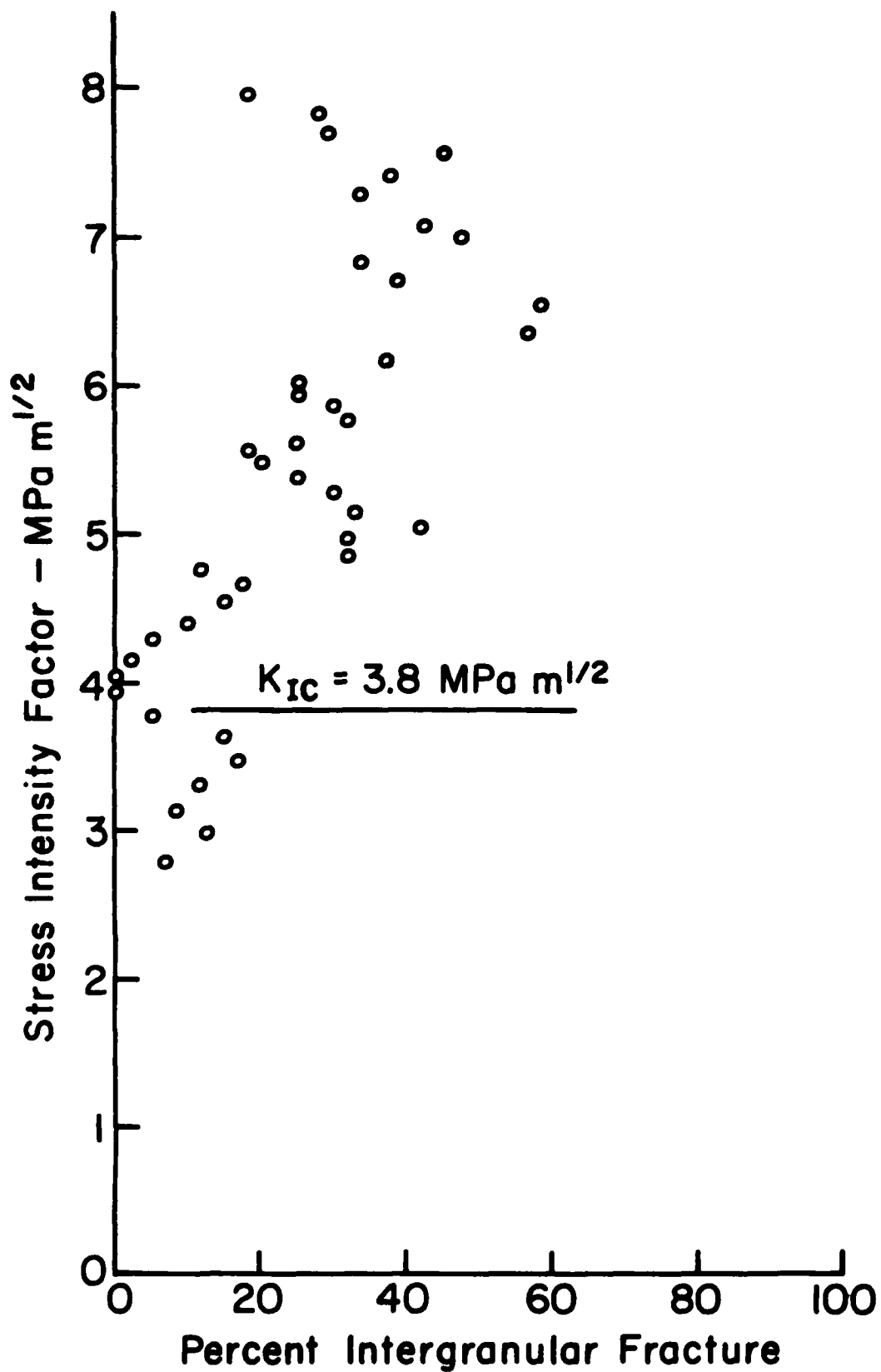
Figure 28. Stress intensity factor vs. percent intergranular fracture
(Specimen #8, 96% alumina fractured in CCl_4, $\sigma_F = 509$ MPa).
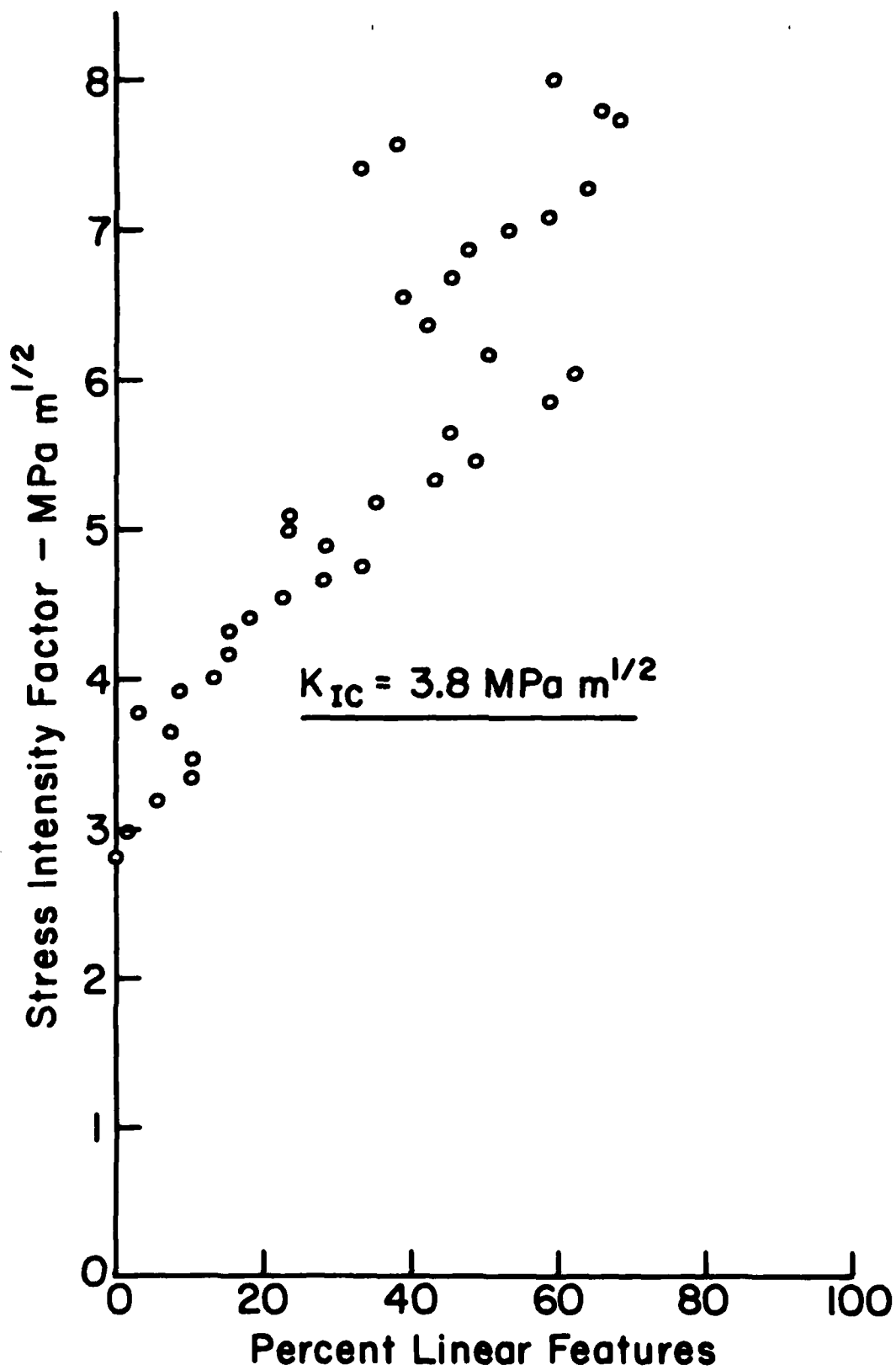
Figure 29.   Stress intensity factor vs. percent linear features
(Specimen #8, 96% alumina fractured in CCl$_4$, σ_F = 509 MPa).

increased area density of linear features. The fracture remains trans-granular and the areas are large so the individual grains are not well defined. The photograph shows regularly spaced horizontal lines on some of the lighter surfaces and jagged edges. These features are believed to be artifacts of vibrations of the SEM. Most of the linear features are river marks and ordinary cleavage steps.

Area C, which was subjected to K_I = 8 MPa $m^{\frac{1}{2}}$, represents an area in which there was more intergranular fracture. Perhaps for this reason there are a number of smaller areas of transgranular fracture and in these areas the individual grains are more well defined. Most of the linear features appear to be river marks but there are also ordinary cleavage steps and microcracks.

Area D, which was subjected to K_I values in the range 8-9 MPa $m^{\frac{1}{2}}$ is characterized by a high proportion of transgranular fracture with the individual grains in the transgranularly fractured areas being relatively well defined. In some cases the individual grains are evident because of microcracks in the grain boundaries. In other cases, the crack changed direction at the grain boundary so that the grain boundary is especially well defined under the stereo viewer. This observation suggests that at high crack velocities there is a greater tendency for the crack to change direction to take advantage of a lower fracture energy plane than at low crack velocities. Many linear features were observed as one might expect at high K_I. These linear features include a high fraction of river marks. In addition, the large,angular, five-sided grain has very regular parallel striations in the surface that appear to be oriented parallel to lattice planes. This grain is shown at higher magnification in Figure 34. Slip

Figure 30. Area A fractured at K_I = 3-4 MPa $m^{\frac{1}{2}}$ showing mainly *transgranular fracture* (96% alumina Specimen #8, σ_F = 509 MPa, 4000X).

Figure 31. Area B fractured at $K_I \simeq$ 6.5 MPa showing cleavage steps (96% alumina Specimen #8, σ_F = 509 MPa, 4000X).

Figure 32. Area C fractured at $K_I \cong 8$ MPa m$^{\frac{1}{2}}$ showing
smaller areas of transgranular fracture
with numerous linear features including
river marks (96% alumina Specimen #8,
$\sigma_F = 509$ MPa, 4000X).

Figure 33. Area D fractured at $K_I = 8$-9 MPa m$^{\frac{1}{2}}$ showing
a transgranularly fractured area in which
the individual grains are relatively well-
defined (96% alumina Specimen #8, $\sigma_F = 509$
MPa, 4000X).

and twinning were considered as possible mechanisms responsible for these linear features. The striations bear some resemblance to facets formed on annealing twins in brass[29a]. Heuer[29b] indicates that only rhombohedral deformation twinning occurs in alumina at room temperature or below in the absence of hydrostatic pressure. However, the possibility that slip or twinning occurred during earlier high temperature processing must be considered and the possibility that high temperatures existed momentarily at the crack front during fracture cannot presently be excluded. Therefore, the mechanism responsible for these features remains uncertain.

This series of pictures of A-D provides strong evidence of the increasing disruption of the fracture surface with increasing radius from the fracture origin (increasing K_I and V). Figure 35 shows Area E which contains a rectangular grain with numerous cleavage steps. The irregular spacings of the steps resemble those observed by Hillier[29c] in UO_2. Area E was subjected to $K_I \cong 7$ MPa $m^{\frac{1}{2}}$. Most of the surface is covered with linear features including cleavage steps.

Fracture in H_2O, Specimen #119

Specimen #119 was also loaded at a linear loading rate and fractured in about one minute. It was chosen as an example of fracture in water because of the large number of phenomena illustrated by the available photographs. The general appearance of the fracture surface is indicated by Figure 36 in which the fracture origin is indicated by A. A section of branched crack that did not separate from the fracture surface is indicated by B. The reflecting spots are shown in the optical micrograph in Figure 37. The reflecting spots surround the fracture origin. Careful comparison of the photographs reveals that the reflecting spots correspond in detail to the

Figure 34. Five-sided grain in Area D showing striations
parallel to grain edges and a microcrack at
the grain boundary (96% alumina Specimen #8,
σ_F = 509 MPa, 10,000X).

Figure 35. Area E fractured at $K_I \cong 7$ MPa m$^{\frac{1}{2}}$ showing
linear features including cleavage steps
(96% alumina Specimen #8, σ_F = 509 MPa,
4000X).

68
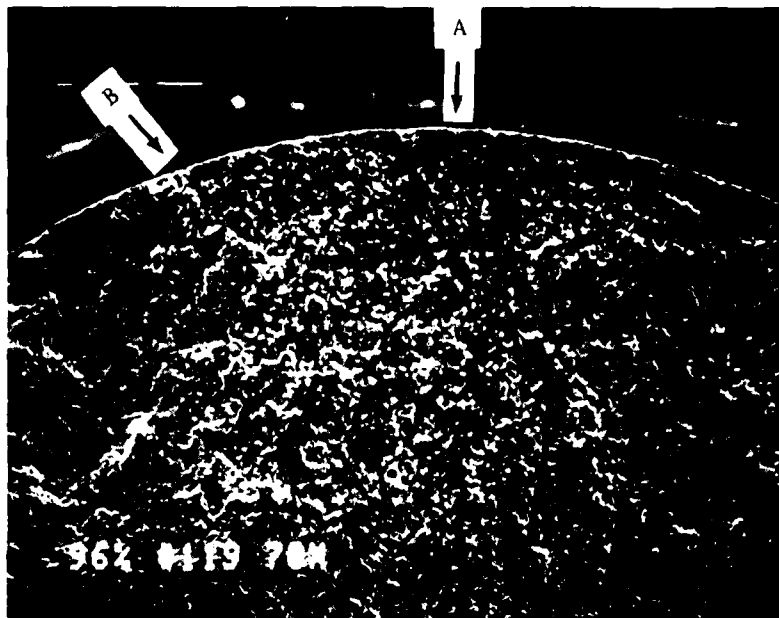
Figure 36. Fracture surface of 96% alumina Specimen
            #119 fractured in water, A is the fracture
            origin and B is a large scale crack branch-
            ing boundary (σ_F = 390 MPa, 70X).

Figure 37. Optical photomicrograph of fracture surface
            of 96% alumina Specimen #119 fractured in
            water showing reflecting spots surrounding
            the fracture origin (σ_F = 390 MPa, 60X).

areas of transgranular fracture. This is especially apparent in the case of the two streaks of reflecting spots that radiate from the fracture origin. Many of these details are described in the following paragraphs.

The composite photograph of the fracture surface of Specimen #119 is given in Figure 38. Because of the increased subcritical crack growth in environments containing water, this specimen fractured at a much lower fracture stress, 390 MPa, than Specimen #8. The fracture originated at a surface pore about 12 μm deep. Assuming a sharp crack at the pore boundary, K_I is less than 1.7 MPa at this boundary. Despite this low stress intensity factor the crack apparently grew from the pore and the growth was almost entirely by transgranular fracture.

The rather extensive region of transgranular fracture is typical of specimens that fracture at low stresses as a result of subcritical crack growth. In an attempt to evaluate the effect of environment independent of the effect on subcritical crack growth and fracture stress the PIF and PLF data have been plotted vs. K_I in Figures 39 and 40. The PIF vs. K_I data show minima in PIF at approximately the same K_I values as observed previously. As is sometimes observed in 96% alumina specimens fractured under conditions where there is considerable opportunity for subcritical crack growth, little or no intergranular fracture was observed near the fracture origin. The PLF vs. K_I data show an increase in PLF with K_I especially at K_I values over 6 MPa $m^{\frac{1}{2}}$. Comparison of these results with similar data in Figures 28 and 29 for Specimen #8 fractured in CCl_4 revealed some differences. In water there appears to be less intergranular fracture in the K_I range 5-6 MPa $m^{\frac{1}{2}}$ and fewer linear features in the K_I range 4-6.5 MPa $m^{\frac{1}{2}}$. It is uncertain at this point whether these results are meaningful

because the results depend to some extent on the quality of the photographs and the objectivity of the observer. Nevertheless, observation of more transgranular fracture and fewer linear features in H_2O compared with CCl_4 seems consistent with the fact that H_2O aids crack propagation.

The discussion in the previous paragraph raises the question whether or not the environment can diffuse to the crack front of fast moving cracks in these specimens. In fracture mechanics tests involving large cracks, Region II of the Log V vs. Log K_I curve (Figure 14) is a region in which the crack velocity is less than otherwise expected because the crack tends to outrun the environment. In double torsion beam tests on an aluminum oxide body Evans[24] observed Region II at $V \cong 10^{-3}$ $m \cdot s^{-1}$ for air at 50% rh. In these tests the diffusion distance is about 2 mm whereas in our case with inherent flaws the diffusion distance in K_I range of interest is about 100 μm, a factor of 20 less. On the other hand the crack velocities increase substantially above 10^{-3} $m \cdot s^{-1}$ to about 10^3 $m \cdot s^{-1}$ at the terminal velocity. Thus it seems that the effect of environment will persist to significantly higher crack velocities in specimens fractured from inherent flaws but the crack should eventually be expected to outrun the environment as the crack length and crack velocity continue to increase.

The characteristics of the linear features formed at various radii from the fracture origin were studied using photographs taken at higher magnifications. These photographs show that this fracture surface has a much less disturbed appearance than that of Specimen #8 which was fractured at a higher fracture stress in CCl_4. Also, a larger fraction of the linear features are ordinary river marks.

Figure 38. Composite scanning electron micrograph of the fracture
surface of a 96% alumina specimen fractured in water
(Specimen #119, σ_F = 390 MPa, 1000X).

300	250	200	150	100
8.60	7.85	7.62	6.08	4.96

Distance from Fracture Origin-μm

100   50   0   50   1

4.96   3.51   0   3.51   4

Stress Intensity Factor – MPa m^1/2

Fracture Origin

END
DATE
FILMED
02-82
DTIC
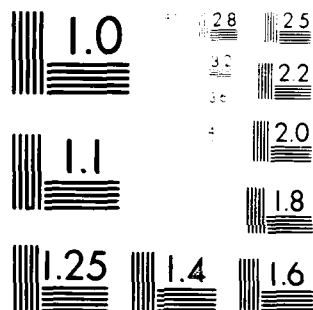
1.0

2.8   2.5
3.2
3.6   2.2

2.0

1.1

1.8

1.25   1.4   1.6

MICROCOPY RESOLUTION TEST CHART

100	150	200	250	30(
4.96	6.08	7.02	7.85	8.6(
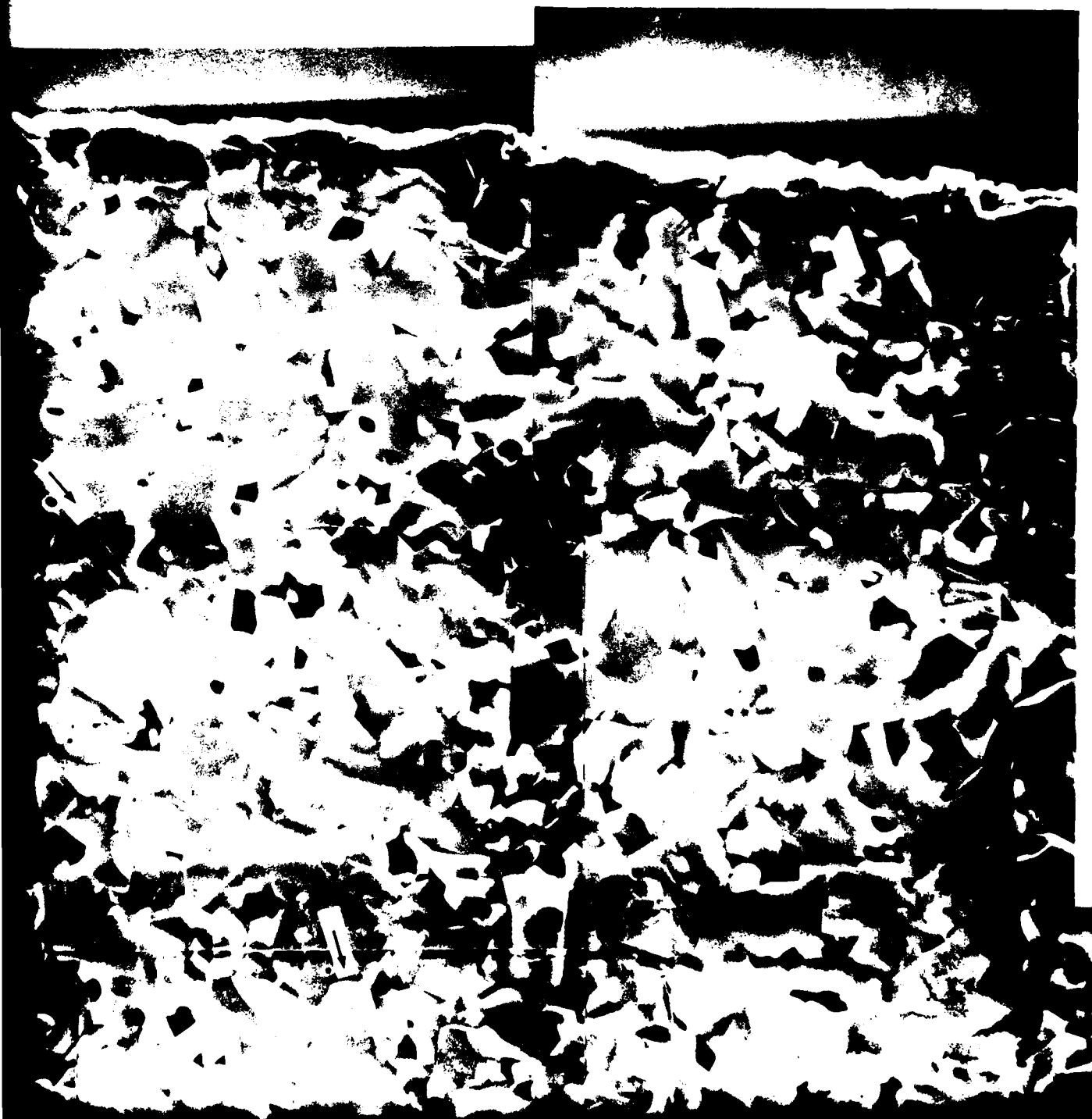
sity Factor – MPa m$^{1/2}$

250   300
7.85   8.60

0 ─┬─ 0

3.51 ─┼─ 50

4.96 ─┼─ 100

6.08 ─┼─ 150

nsity Factor – MPa m$^{1/2}$
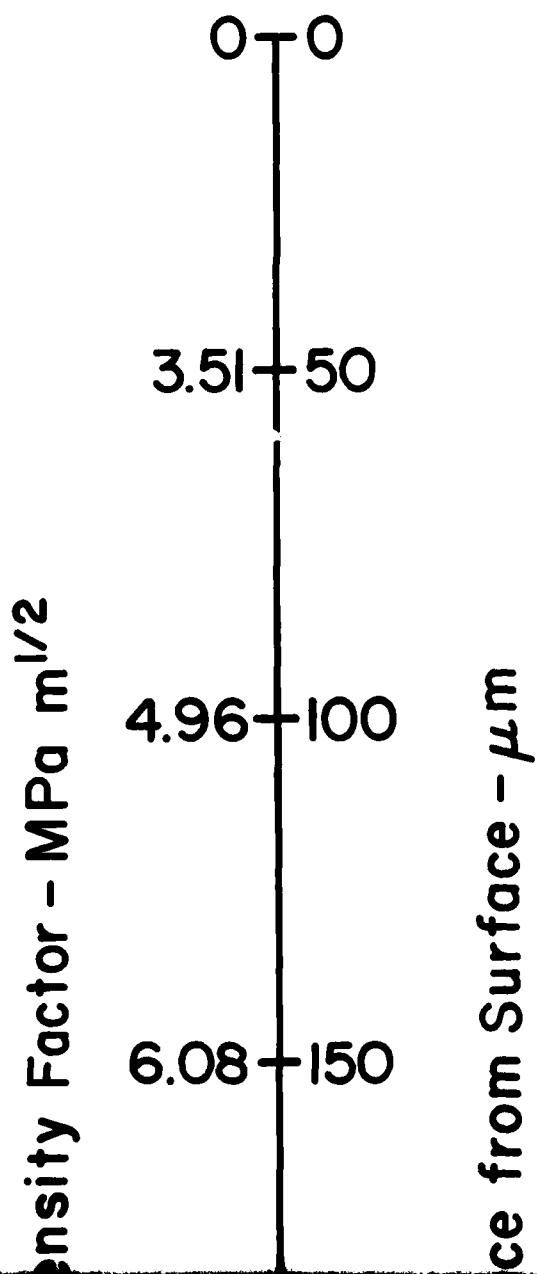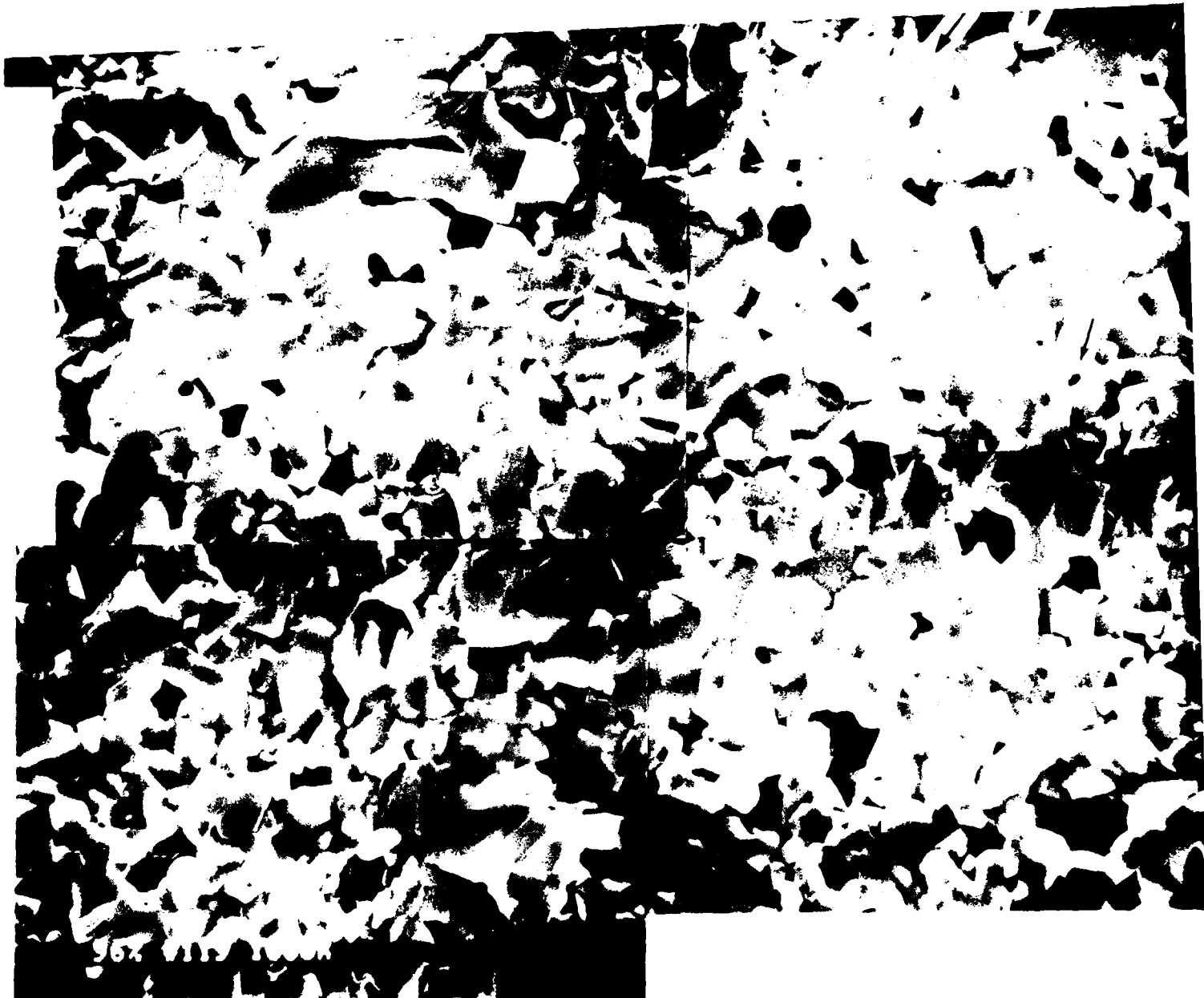
ce from Surface – μm

Figure 38. Composite scanning electron
in water (Specimen #119, σ_F
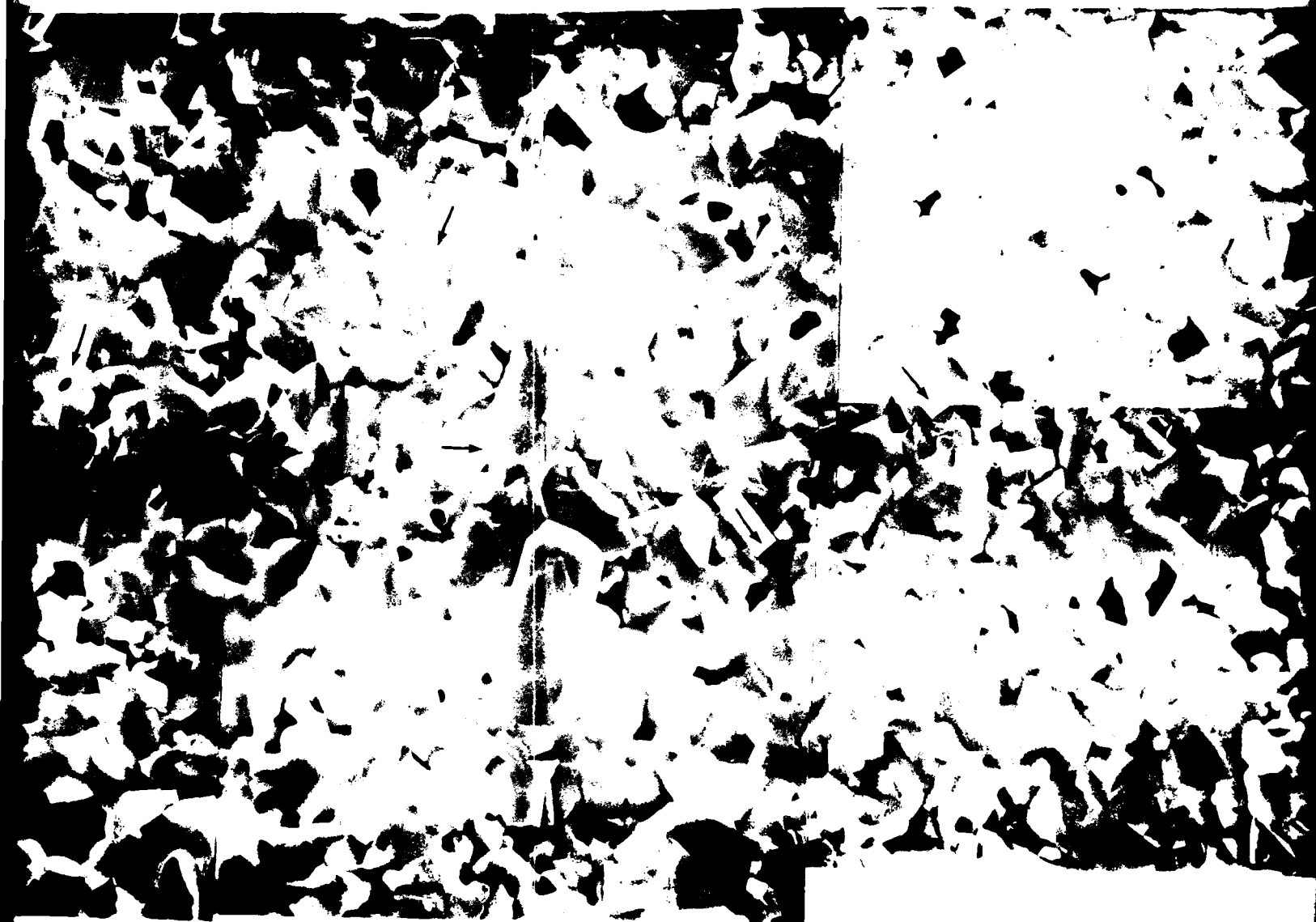
ectron micrograph of the fracture surface of a 96% alum
119 , σ_F = 390 MPa , 1000X).

Stress Intensity Fa

6.08 — 150

7.02 — 200

7.85 — 250

8.60 — 300
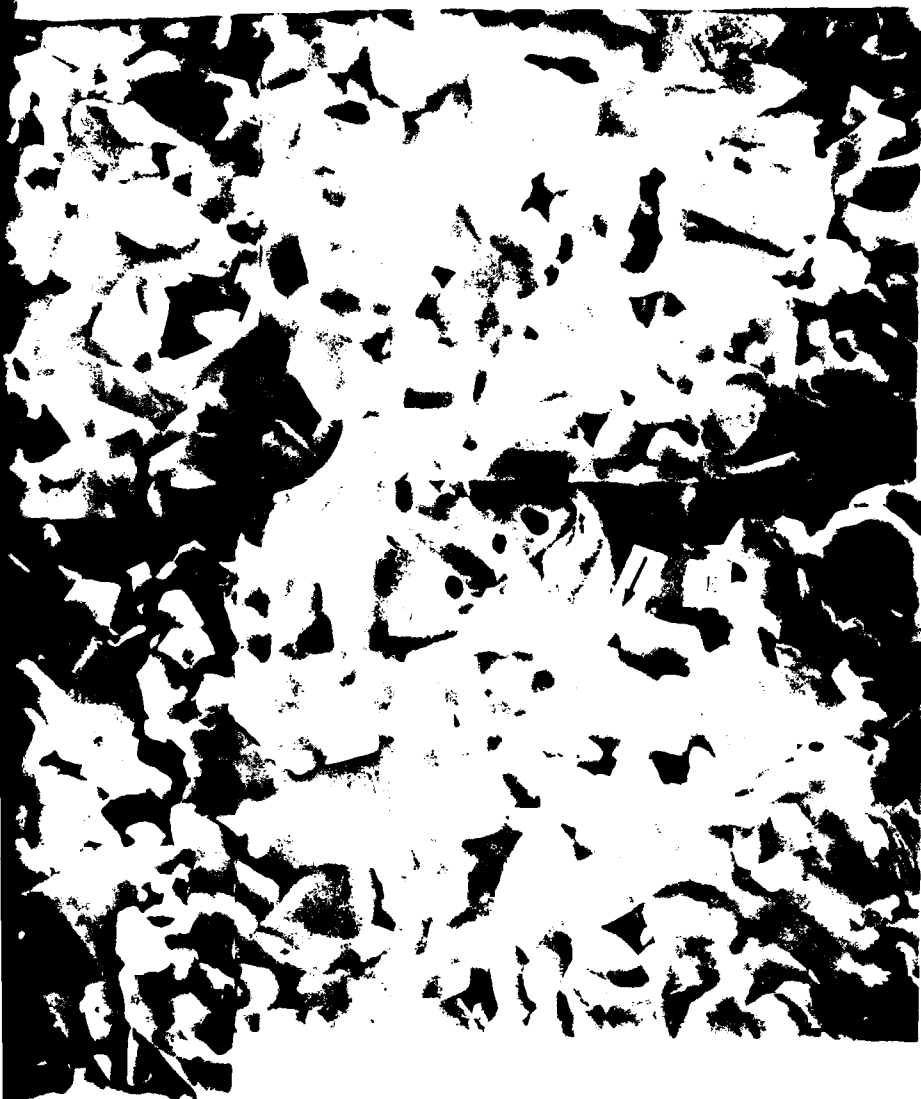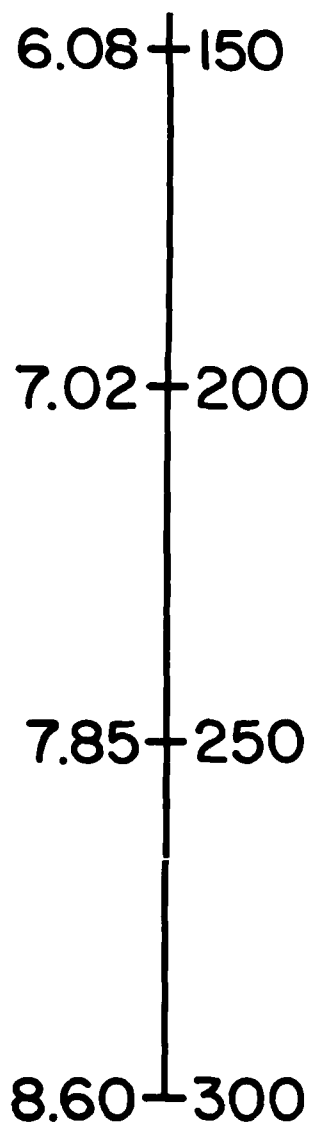
Distance from S

% alumina specimen fractured
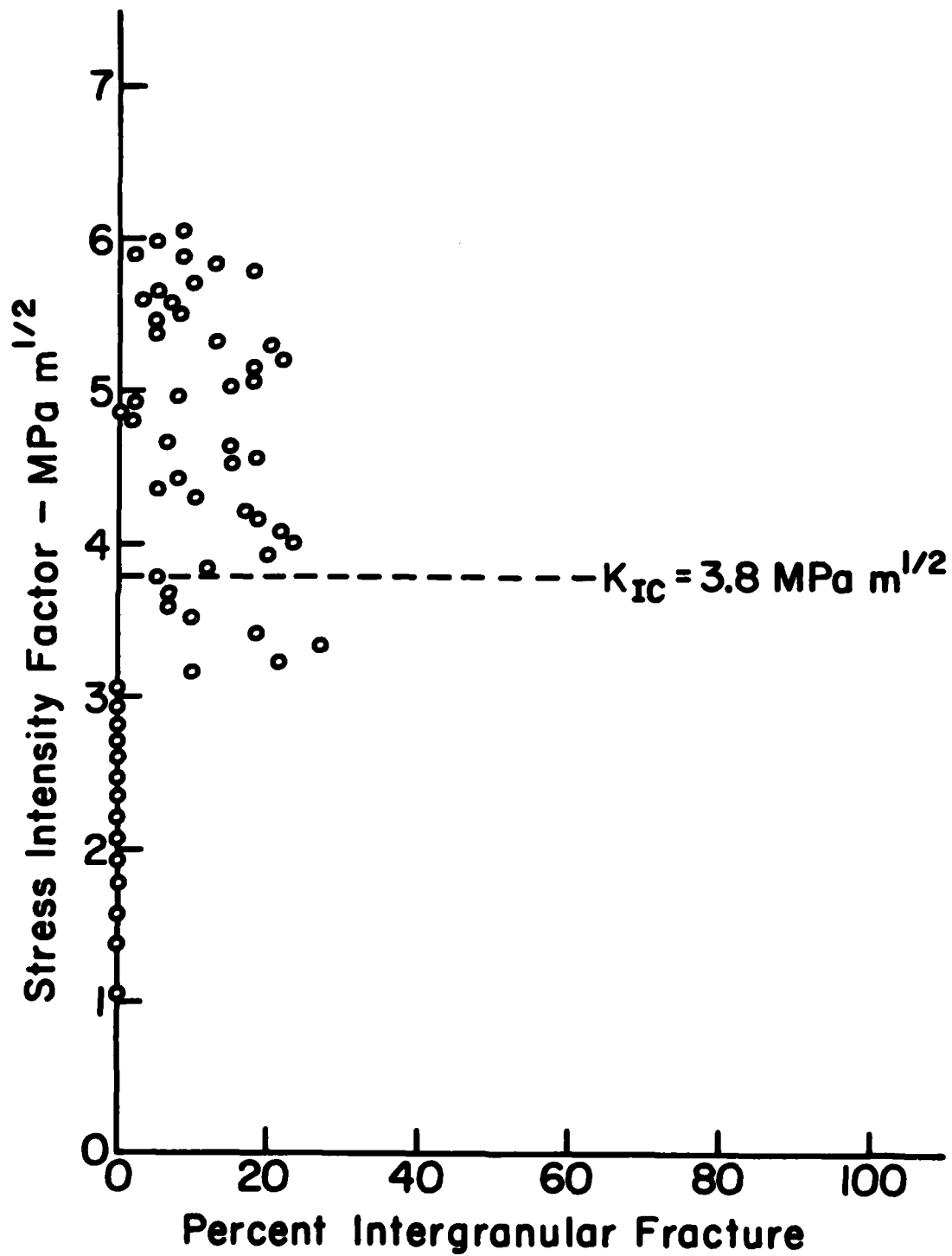
Figure 39. Stress intensity factor vs. percent intergranular fracture
(96% alumina Specimen #119 fractured in water, σ_F = 390 MPa).
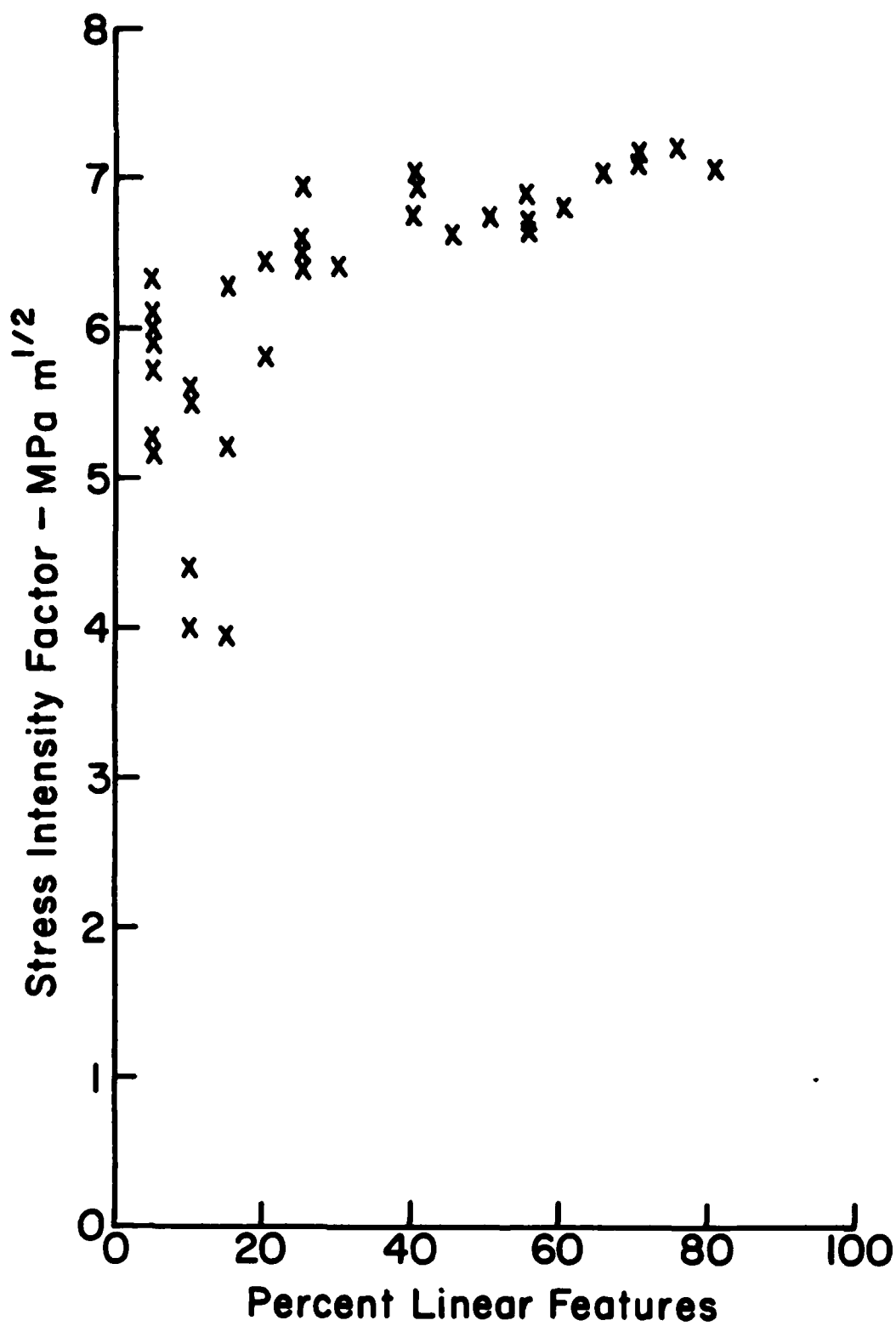
Figure 40. Stress intensity factor vs. percent linear features
(96% alumina Specimen #119 fractured in water, σ_F = 390 MPa).

An attempt was made to determine whether or not the regions of increased intergranular fracture represented regions that resisted crack growth by tracing the river marks in these areas. Presumably, if these are resistant regions the crack will tend to extend around these regions by transgranular fracture. Then, when the stress intensity factor at the boundaries of the resistant area increases to the value necessary to cause fracture there, the fracture may extend into the resistant region from several directions that may also be indicated by the river marks. The directions of crack propagation based on the river marks are indicated by the arrows in Figure 38. These arrows point in a variety of directions showing clearly that local fracture does not always propagate parallel to radii from the fracture origin.

Area L was subjected to more intensive observation. This area represents an area of increased intergranular fracture and it is shown at higher magnification in Figure 41. River marks are clearly visible adjacent to numbers 1-5 on the photo. Based on the fact that the direction of crack propagation is the same as the direction of water flow if the branches were tributaries of a river, it is apparent again that the direction of crack propagation varied at various points in the fracture surface. So far, examination of the river marks has not provided conclusive evidence that the regions of increased intergranular fracture are resistant to crack propagation. Nevertheless, based on the increase in PIF with K_I, it remains our opinion that this is the case.

Area L also shows a number of other interesting features. Some of the grains, especially the one at 6 show striations similar to those observed in Specimen #8. This grain is located where $K_I \cong 6$ MPa m$^{\frac{1}{2}}$. This K_I value is
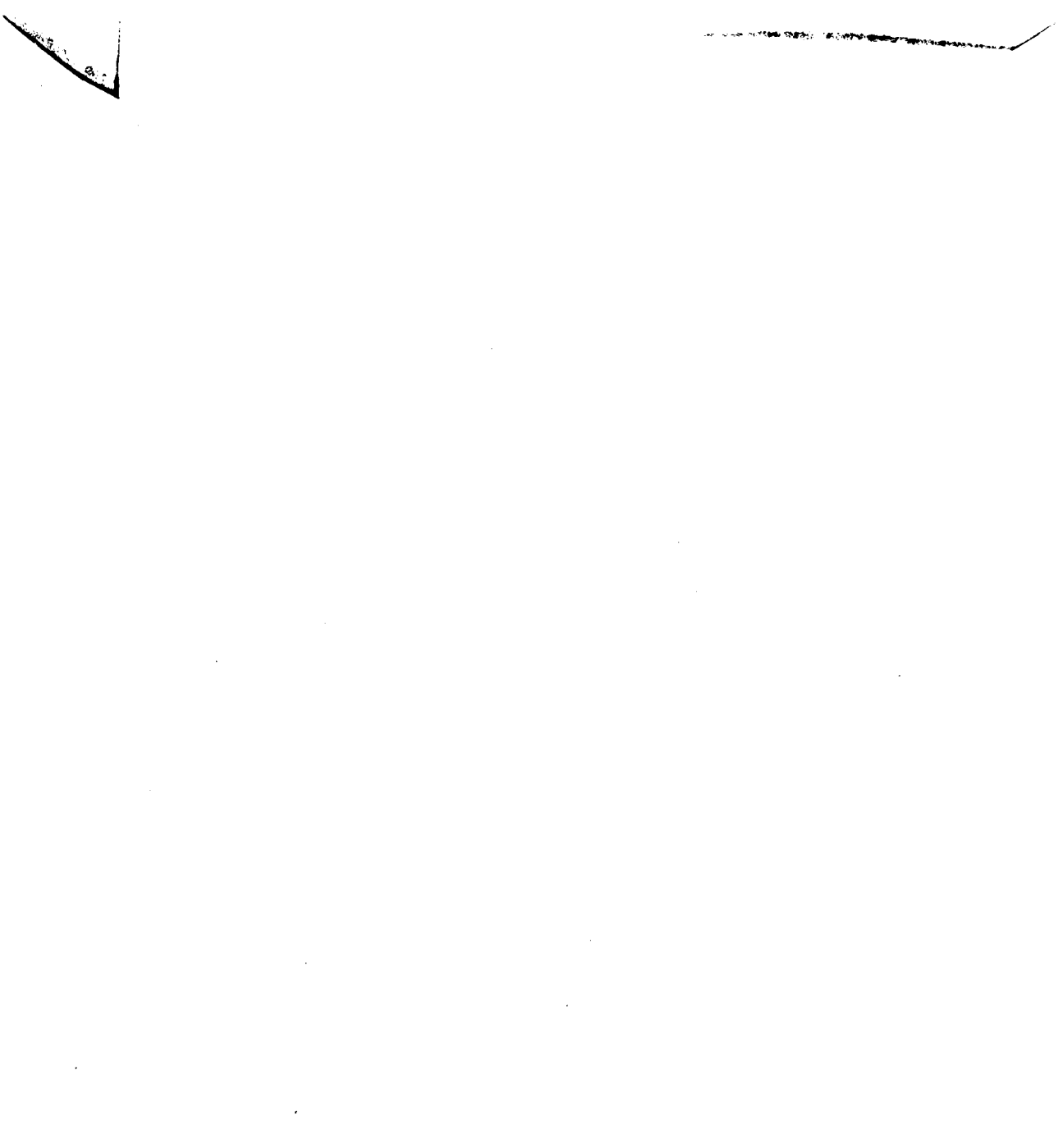
Figure 41. Area L of Figure 38 showing river marks and striations at higher magnification (96% alumina Specimen #119 fractured in water, σ_F = 390 MPa, 10,000X).

Figure 41. Area L of Figure 38 showing river
(96% alumina specimen #119 fractur

river marks and striations at higher magnification
ractured in water, σ_F = 390 MPa, 10,000X).

substantially lower than the K_I value at which these features were observed in Specimen #8. To the right of 1 is a cross hatched region. Another similar region can be seen above Area L in Figure 38. In some cases these cross hatched regions appear to occur as a result of intersections of Wallner lines in individual grains.

Other interesting features observed in this fracture surface are cleavage steps and microcracks. Cleavage steps from Area D of Figure 38, are shown in Figure 42. The microcracks have several different appearances. In some cases they occur at tilt-twist boundaries where river marks originate as shown in Figure 43. In other cases the microcracks are lined with globules of material that may be the siliceous intergranular phase. The appearance of this material suggests the possibility that it may have been melted during the passage of the crack.

Crack branching in Specimen #119

The region in which crack branching occurred is shown at higher magnification in Figure 44. This region is at a radius of about 500 μm from the fracture origin. The apparent stress intensity factor at crack branching (K_B) is 11.1 MPa $m^{\frac{1}{2}}$. This value is very close to the average values determined previously[15] which were 10.6 and 11.3 MPa $m^{\frac{1}{2}}$ after correction for the larger value of Y used in the present investigation.

In Figure 44 the line along which the crack branching originally occurred is indicated by the inclined lines at the edges of the photographs. This line is slightly above the bright line of grains that mark the edge under which the crack has propagated. The reason for the difference between these lines is that the sharp edge of the wedge formed by crack branching appears to have chipped away leaving the present blunt edge.

Figure 42. Cleavage steps at Area D in Figure 38
(96% alumina Specimen #119 fractured in
water, σ_F = 390 MPa, 4000X).

Figure 43. Microcrack at Area E in Figure 38
(96% alumina Specimen #119 fractured in
water, σ_F = 390 MPa, 10,000X).

78

BEFORE CRACK BRANCHING

AFTER CRACK BRANCHING

BEFORE CRACK BRANCHING

AFTER CRACK BRANCHING
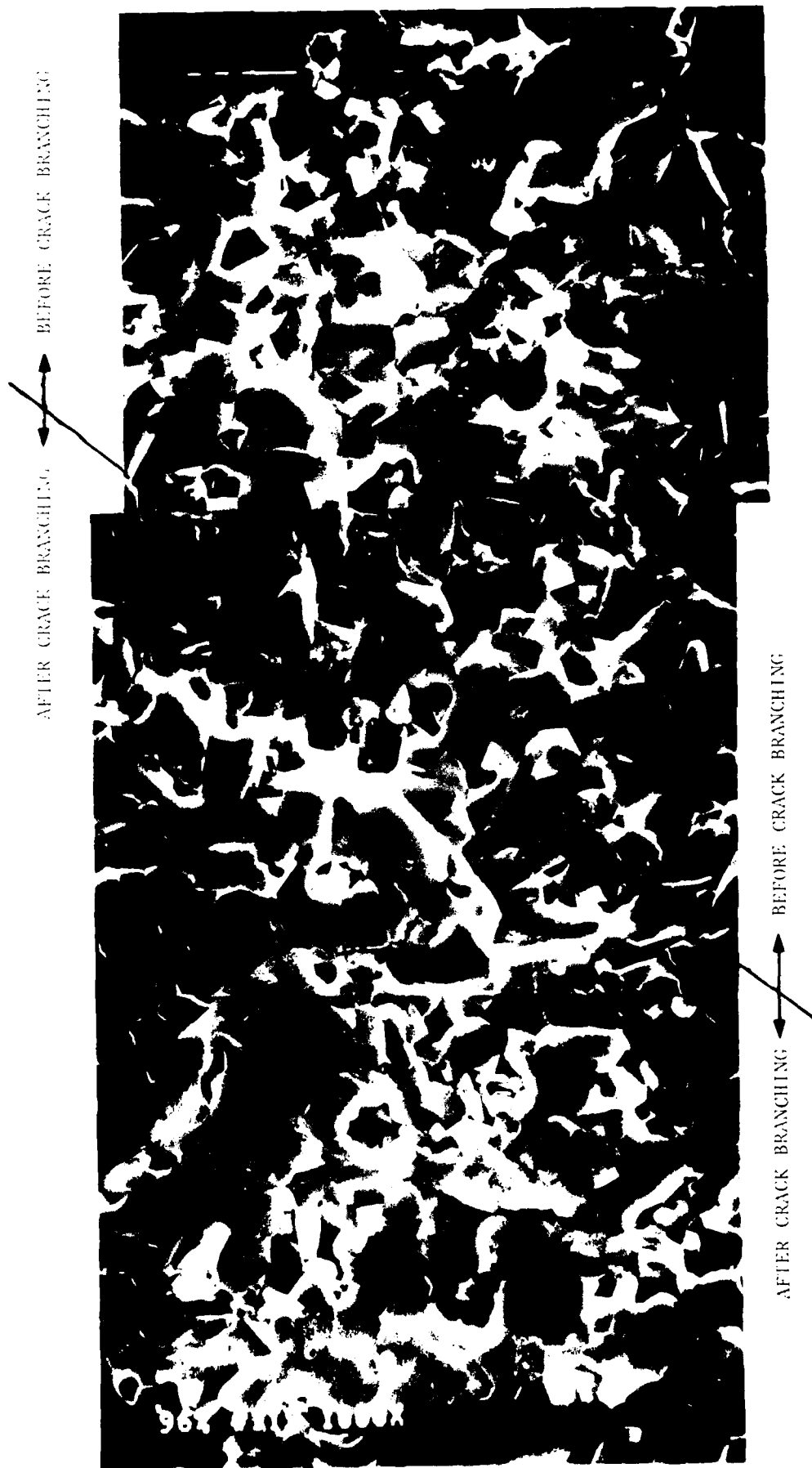
Figure 44. Comparison of the fracture surface before and after large scale crack branching (96% alumina Specimen #119 fractured in water).

The fracture surfaces before and after crack branching were expected to show substantial differences due to the fact that, because of the extra energy necessary to form four surfaces rather than two, less energy is available after branching to disturb the fracture surface. For example, in glass the mirror-like surface observed near the fracture surface reappears after branching (Figure 6). In the present case the areas of transgranular fracture seem to increase in size after branching. Otherwise, the degree of disturbance of the surfaces, for example the area density of linear features, doesn't seem to change appreciably.

These observations bear on the question whether there is an equivalent of mist (incipient crack branching) in these polycrystalline ceramics. If there is, it should appear above the crack branching boundary in Figure 44 and be absent below this boundary. It is not clear that such an equivalent of mist is present in this case.

Effect of environment on fracture features of other 96% alumina specimens

Composite photographs of fracture surfaces of other 96% alumina specimens fractured in water and CCl_4 were prepared and evaluated as indicated in the previous sections. In this section these fracture surfaces are systematically described and compared.

The characteristics of five specimens fractured in water are given in Table VI. Two of these specimens were loaded in flexure using a linear loading rate and three were fractured by delayed fracture. The fracture stresses were calculated taking the location of the fracture origin on the cylindrical surface into account. The specimens include high and low strength specimens fractured by linear loading and specimens that fractured over a wide range of times in delayed fracture. In addition, all of the

TABLE VI

Characteristics of 96% Al_2O_3 Specimens Fractured in Water

Specimen No.	Fracture Stress MPa	Time to Failure s	Flaw at Origin	Subcritical Region	Subcritical-Critical Boundary	Other Comments
67 (Linear Loading)	442	--	Intergranular machining flaw 5 μm(one grain) deep $K_I=1.26$ MPa m$^{\frac{1}{2}}$	Wavy transgranular fracture, scattered intergranular fracture	Critical flaw 40-45 μm deep, semi-circular. Pullouts & projecting graing $K_I=3.55-3.76$ MPa m$^{\frac{1}{2}}$	Large areas of radiating cleavage steps (river marks)in critical region
119 (Linear Loading)	390	--	Surface pore 10 μm deep $K_I=1.57$ MPa m$^{\frac{1}{2}}$	Wavy transgranular fracture, linking causes elliptical region, major axis along surface, very little intergranular fracture	Critical flaw ~44 μm deep, elliptical, pullouts and projecting grains at boundary $K_I=4.06$ MPa m$^{\frac{1}{2}}$	Radiating regions of transgranular fracture. Cross-hatched region of transgranular fracture (Wallner lines?),also good river markings
89 (Delayed Fracture)	390	1	Surface pore 17 μm deep $K_I=2.04$ MPa m$^{\frac{1}{2}}$	Wavy transgranular fracture, linking to right to another surface pore	Critical flaw ~60 μm deep, pullouts and projecting grains at boundary $K_I=3.84$ MPa m$^{\frac{1}{2}}$	Radiating regions of transgranular fracture. Linear features at $K_I = 6.0$ MPa m$^{\frac{1}{2}}$
104 (Delayed Fracture)	369	10	Flaw uncertain, perhaps linking of surface pore and subsurface pore	Wavy transgranular fracture, perhaps with linking to right	Critical flaw ~60 μm deep, pullouts and projecting grains at boundary $K_I = 3.63$ MPa m$^{\frac{1}{2}}$	Fracture surface has very uniform appearance,confirmed by reflecting spots, little evidence of radiating regions of transgranular fracture
142 (Delayed Fracture)	368	5057	Intergranular machining flaw and associated subsurface pore 16 μm deep $K_I=1.87$ MPa m$^{\frac{1}{2}}$	Wavy transgranular fracture, linking to right & left to form elliptical region with major axis along surface	Critical flaw ~55 μm deep, elliptical, pullouts and project-ing grains at boundary $K_I = 4.31$ MPa m$^{\frac{1}{2}}$	Large transgranu-lar areas scattered at large radii (advance cracks)

specimens were selected on the basis of relatively symmetrical crack propagation. This characteristic was judged mainly on the basis of symmetrical reflecting spots. The main purpose of this selection was to improve our estimates of the stress intensity factors acting at various stages of crack growth.

The following observations seem especially significant:

1. The fractures originated at surface pores or machining flaws.

2. The flaws at the fracture origins are much smaller than the critical flaws.

3. The estimated K_I values at the original flaw boundaries range from 1.26 - 2.04 MPa $m^{\frac{1}{2}}$, showing that subcritical crack growth must occur at low K_I values.

4. Flaw linking has an important role in subcritical crack growth.

5. Subcritical crack growth occurs by wavy transgranular fracture in which the direction of crack propagation changes only slightly relative to the average fracture plane in going from one grain to another.

6. In 96% Al_2O_3 the subcritical crack growth boundary is marked by an irregular row of pullouts and projecting grains.

7. The estimated K_I values at the subcritical crack growth boundary determined using the previously developed criteria range from 3.55 - 4.31 MPa $m^{\frac{1}{2}}$. These values can be compared with K_{IC} = 3.8 MPa $m^{\frac{1}{2}}$ measured using fracture mechanics tests on large cracks.

8. Transgranular fracture is the principal mode of fracture over the entire portion of the fracture surface that was examined (150 x 300 μm).

9. The frequency of occurrence of linear features increases with increasing distance from the fracture origin.

The characteristics of fracture surfaces of specimens fractured in "water free" media are tabulated in Table VII. As in the case of the specimens tested in water these specimens were loaded by two methods, either at a constant loading rate or by dead weight loading in delayed fracture tests.

The specimens in CCl_4 fractured at stresses ranging from 510 MPa for the strongest linearly loaded specimen down to 370 MPa for a delayed fracture specimen that fractured in 3600 s. The fractures originated at several different types of preexisting surface flaws. The stress intensity factors (K_I) at these flaw boundaries were calculated in several cases where the flaws were relatively well defined. The flaws were assumed to be semi-circular surface flaws. The K_I values ranged from 1.29 to 2.84 MPa $m^{\frac{1}{2}}$. The critical stress intensity factor (K_{IC}) of the 96% Al_2O_3 is about 3.8 MPa $m^{\frac{1}{2}}$. Therefore, it is apparent that a substantial amount of subcritical crack growth must have occurred in these specimens despite the relative absence of water in the environment.

The subcritical crack growth region consisted mainly of wavy transgranular fracture interspersed with small areas of intergranular fracture. In one case (#178) the wavy transgranular fracture region (and the reflecting spots) was elongated into the specimen, perhaps indicating less resistance to crack propagation perpendicular to the surface than parallel to it. In another case (#210) the transgranular fracture region consisted of radiating ridges rather than wavy areas. There is no obvious explanation for this difference in the fracture mode.

As in the cases of specimens fractured in water and in air, the sub-
critical to critical crack growth boundary was often marked by a discontinuous
line of pullouts and projecting grains. The region of wavy transgranular
fracture extends beyond this boundary, usually leading to another minimum
in the percent intergranular fracture. However, the surface has an in-
creasingly disturbed appearance and the regions of transgranular fracture
frequently were broken into segments radiating from the fracture origin.
At K_I values ranging from 4.7 to 7.4 MPa $m^{\frac{1}{2}}$, a diffuse boundary was observed
at which the fraction of grains with linear features increased substantially
and the boundaries of the individual grains in the regions of transgranular
fracture became much more evident.

Preliminary attempts were made to compare the fracture features of the
specimens fractured in "water free" media with those observed in specimens
fractured in water. Among the specimens with characterized fracture sur-
faces, the fracture stresses of the specimens fractured in water ranged
only from 368 to 442 MPa while those fractured in "water free" media ranged
from 370 to 510 MPa. Therefore, it was necessary to compare the fracture
features in some way that accounts for the differences in fracture stress,
for example, at equal values of stress intensity factor acting at the crack
tip at each stage of crack growth. The flaws at the fracture origins of
the specimens fractured in CCl_4 were larger and more well defined than those
of specimens fractured in water. This observation is reasonable, especially
in view of the fact that the higher loads applied to some of the specimens
loaded in CCl_4 allowed larger areas of the cylindrical surfaces to be
stressed at high stresses so that the fracture would tend to seek out larger
flaws. The ranges of K_I calculated at the boundary of pullouts and projecting
grains were approximately the same for both water and CCl_4 environments.

TABLE VII

Characteristics of 96% Al_2O_3 Specimens Fractured in "Water Free" Media

Specimen No.	Fracture Stress MPa	Time to Failure s	Flaw at Origin	Subcritical Region	Subcritical-Critical Boundary	Other Comments
Fractured in CCl_4						
8	509	--	Surface pore 18 μm deep K_I=2.75 MPa $m^{\frac{1}{2}}$ river marks point back to pore	Wavy transgranular fracture	Critical flaw 44 μm deep, semi-circular pullouts and projecting grains K_I=4.29 MPa $m^{\frac{1}{2}}$	Linear features K_I = 5.41 MPa $m^{\frac{1}{2}}$ Many microcracks
178	510	--	Loosely bonded grains ~5μm under surf. and ~10 μm diameter. K_I = 1.29 MPa $m^{\frac{1}{2}}$ Probable linking to surface	Wavy transgranular fracture, reflecting spots elongated into specimen	Critical flaw ~30 μm deep, semi-circular, pullouts and projecting grains interspersed with wavy transgranular fracture at boundary K_I = 3.55 MPa $m^{\frac{1}{2}}$	Large areas of wavy transgranular fracture beyond SCCG boundary linear features at ~7.4 MPa $m^{\frac{1}{2}}$
210	500	--	Pulled out surf. agglomerate 25 x 20 μm K_I=2.84 MPa $m^{\frac{1}{2}}$ Linking to left and right	Transgranular fracture, ridges radiating from surface	Critical flaw ~40 μm deep, semi-elliptical, pullouts and projecting grains, K_I = 4.42 MPa $m^{\frac{1}{2}}$	Projecting grains form ridge at K_I = 4.7 MPa $m^{\frac{1}{2}}$ linear features at ~7 MPa $m^{\frac{1}{2}}$
193	455	--	Surface pore 25 x 20 μm K_I=2.84 MPa $m^{\frac{1}{2}}$ linking to left and perhaps to right	Wavy transgranular fracture, intense reflecting spots	Critical flaw may have one or two lobes assuming one lobe ~50 μm deep, K_I = 4.07 MPa $m^{\frac{1}{2}}$, pullouts & projecting grains	Linear features at K_I = 6 MPa $m^{\frac{1}{2}}$ unusually large number of pores

(continued)

Table VII (continued)

Specimen No.	Fracture Stress MPa	Time to Failure s	Flaw at Origin	Subcritical Region	Subcritical-Critical Boundary	Other Comments
50 (delayed fracture)	442	10	Origin at pores ~25 μm from surface, linking to surface	Wavy transgranular fracture	Critical flaw ~50 μm deep, semi-circular K_I = 3.97 MPa m$^{\frac{1}{2}}$ pullouts and projecting grains	Linear features at K_I = 5.47 MPa m$^{\frac{1}{2}}$
54 (delayed fracture)	370	3586	Crushed grain ~12 μm deep K_I=1.63 MPa m$^{\frac{1}{2}}$ Linking to right and left	Wavy transgranular fracture	Critical flaw 60 μm deep, semi-circular, pullouts and projecting grains K_I = 3.64 MPa m$^{\frac{1}{2}}$	Linear features K_I = 4.7 MPa m$^{\frac{1}{2}}$
127 (delayed fracture)	382	11,700	Unbonded or loosely bonded surface grains	Wavy transgranular fracture, symmetrical reflecting spots	Critical flaw 52 μm deep, semi-circular pullouts and projecting grains K_I = 3.5 MPa m$^{\frac{1}{2}}$	Linear features K_I = 5.31 MPa m$^{\frac{1}{2}}$
103	444	--	Surface check possible linking to internal pore	Wavy transgranular fracture	Critical flaw 55 μm deep, semi-circular, pullouts and projecting grains K_I = 4.18 MPa m$^{\frac{1}{2}}$	Linear features K_I = 6.67 MPa m$^{\frac{1}{2}}$
Fractured in Silicone Oil (5 centistokes)						
150	500	--	No apparent flaw no linking	Wavy transgranular fracture	Critical flaw ~55 μm deep, semi-elliptical major-axis $\perp$ surface, pullouts and projecting grains K_I = 4.04 MPa m$^{\frac{1}{2}}$	Linear features intense radiating K_I = 5.42 MPa m$^{\frac{1}{2}}$

Direct comparisons were made for two pairs of specimens fractured at approximately equal fracture stresses. One member of each pair was fractured in each environment. These results are presented in Table VIII.

Based on Cuthrell's work[22a] and our earlier delayed fracture tests we expected to observe greater effects of environment on the micromechanisms of fracture than have, in fact, been observed in this study. However, in some cases Cuthrells results using CCl_4 were intermediate between the results in ultrahigh vacuum and those in water[22b]. He tentatively attributed these intermediate results to moisture trapped in the near-surface regions in the solids. Also, the present lot of material may be less susceptible to environmental effects. In general, our data on several lots of the material received over an interval of ten to fifteen years support this argument to some extent. However, it should be remembered that when the present lot was tested in the as-received condition with ground surfaces, the average flexural strengths were only 347 MPa in CCl_4 and 260 MPa in water. These results can be compared with results for an earlier lot with as-fired surfaces which yielded 288 MPa when tested in water and 348 MPa when tested in air. When the present material was refired at $1500^\circ C$ for one hour, the average flexural strength increased to 388 MPa when tested in laboratory air. Comparing this result with those obtained for the present annealed specimens tested under water indicates that the strength of the present lot may be stronger than the earlier lot by somewhat more than 46 MPa.

The fact that the present material is of better quality still does not explain why it is so little weakened by exposure to water. Therefore it may be helpful to speculate on possible ways that the material could be protected from the stress corrosion by water. One such mechanism might

TABLE VIII

Comparisons of Specimens Fractured at Nearly Equal Fracture

Stress in CCl_4 and Water

Environment	Specimen No.	Fracture Stress MPa	Time to Fracture S	Comparison
CCl_4	54	370	3586*	The specimen fractured in water has larger areas of transgranular fracture, fewer areas of small grains fractured by intergranular fracture and more radiating linear regions of transgranular fracture in the critical crack growth region.
Water	142	368	5057*	
CCl_4	193	455	**	The specimen fractured in water has a less definite flaw at the fracture origin, a "greyer" surface, and a less porous region around the origin, but it is not clear that there is more transgranular fracture around the origin. In fact there seems to be some difference between this comparison and #54 and #142 in this respect because in the present case the specimen fractured in water has more frequent scattered areas of intergranular fracture.
Water	67	442	**	

* delayed fracture test
** flexural strength test

involve the relative absence of residual stresses as a result of annealing.
We have not yet been able to review our own work completely or search the
literature for other cases in which delayed fracture tests on Al_2O_3 have been
done immediately after annealing but this may be the first time it has been
done. Marshall and Lawn[30] have shown recently that for glass tested in
water the percentage strength reduction due to residual stresses is greater
for specimens tested at low loading rates where more subcritical crack
growth can occur than it is at high loading rates. In polycrystalline
ceramics where a greater variety of micromechanisms are available, it seems
possible that the presence of the residual stresses might enhance the
mechanism most susceptible to stress corrosion, thus enhancing the observed
differences in fracture mode.

The frequency of occurrence of various types of flaws at fracture
origins is strongly dependent on the basic material and processes such as
grinding or annealing that are applied to the fired material. The material
is usually strongest in the as-fired condition. When it is ground, machin-
ing flaws and localized residual stresses may be introduced that may weaken
the material. Subsequent annealing may relieve residual stresses at the
machining flaws or partially heal them, leading to substantial increases in
strength. It should be remembered that when earlier specimens were tested
in the ground condition, they were weaker than expected and the lack of
well-defined features on the surfaces made it difficult to locate the
fracture origins. Therefore, specimens were annealed to improve the strength.
Probably, annealing reduced the fraction of the specimens failing at machin-
ing flaws and increased the fraction failing at surface pores and other types
of flaws. The types of flaws causing failure can be influenced by the
environment and the loading rate. Corrosive environments like water and low

loading rates favor surface flaw failure. Therefore, observation of a particular ratio of pores or machining flaws at the fracture origins reflects to a considerable extent the treatments applied to the specimens and the conditions under which they were fractured.

The present observations are consistent with our earlier opinion that, in 96% Al_2O_3, machining flaws are usually intergranular. Because the subcritical crack growth occurs by wavy transgranular fracture, the boundaries between the machining flaws and the subcritical crack growth are well defined. This comment applies also to the boundaries of pores and other fracture origins.

Because the flaws are so much smaller than the critical flaws, substantial subcritical crack growth must occur. It is surprizing that subcritical crack growth can occur at the low K_I values calculated at the origin flaws, assuming that they were semicircular cracks subjected to the maximum loading stresses. Crack velocity measurements of Freiman, McKinney and Smith[19] for the 96% alumina tested at about 40% relative humidity extrapolate to $10^{-8} m \cdot s^{-1}$ at 2.7 MPa $m^{\frac{1}{2}}$, in other words 0.01 $\mu m \cdot s^{-1}$, which should not cause failure in the times that the flaws were exposed to the stresses.

There are several possible explanations of the extent of subcritical crack growth including:

1. The stress intensity factors may be underestimated because of the presence of localized residual tensile stresses.

2. The stress intensity factor may be underestimated because of interactions with nearby flaws.

3. The localized resistance to crack growth may be lower than that determined on large cracks in standard fracture mechanics tests.

It is probable that all of the above mechanisms influence the slow crack growth in these specimens. Even though the specimens were annealed, small residual stresses may remain at the machining flaws. Furthermore, localized residual stresses arise during cooling due to thermal expansion anisotropy of the individual grains. In regions where several grains near a flaw are oriented so that the tensile stresses due to crystal anisotropy are parallel to the applied stresses, the crack growth will be enhanced, assuming that these lattice planes are planes with relatively low fracture energies. As it happens, in α-Al$_2$O$_3$ the c-axis is the high expansion direction[22a] so that the highest tensile stresses are induced on the basal plane which has the highest fracture energy. Therefore, the most vulnerable planes may be the pyramidal planes which are subjected to slightly lower stresses but have much lower fracture energies[4].

Flaw linking in alumina ceramics was first described by Evans and Tappin[3]. It has a critical role in subcritical crack growth when it occurs. Linking occurs because the stress concentrations at the flaws overlap, increasing the probability of fracture of the intervening material. Under conditions in which little subcritical crack growth occurs, flaw linking may be recognizable as paths of transgranular fracture joining neighboring flaws. In the present case, where subcritical crack growth and wavy transgranular fracture are widespread, it is more difficult to recognize flaw linking. River marks pointing from one flaw to another may be a useful indication. Another is the existence of an elliptical region of subcritical crack growth that does not conform to the ellipticity of the flaw at the fracture origin. This situation is frequently observed at surfaces where flaw linking results in elliptical regions of subcritical crack growth with their major axes extending along the surface. In some cases it seems best to assume that linking has occurred

because it seems necessary to permit subcritical crack growth and it
could reasonably have occurred in the circumstances.

It is probable that the resistance to fracture (fracture energy) at
fracture origins is lower than that of large cracks used for fracture
energy or fracture toughness measurements simply because the fracture will
seek out the less resistant regions. These regions may contain unbonded
or weakly bonded grains, pores, or crystals oriented with their less re-
sistant lattice planes oriented in the plane of the crack. This last
mechanism may be more important than one might think. Weiderhorn[4] has
shown that subcritical crack growth can occur on (10$\bar{1}$2) planes in sapphire
at K_I < 1.0 MPa m$^{1/2}$ when the relative humidity is 50%. This means that
favorably oriented grains at the origin flaw boundaries can crack at the
K_I values estimated for the present fracture origins. Therefore, it is
reasonable to think that subcritical crack growth begins by fracture of
these favorably oriented grains followed by flaw linking and ordinary sub-
critical crack growth.

Returning now to discussion of the original observations in Tables VI-VIII
it has been noted that the subcritical crack growth boundary is marked
by an irregular row of pullouts and projecting grains. Similar obser-
vations were made previously[2]. It is reasonable to assume that these
grains are oriented in directions resistant to fracture so that, instead,
intergranular fracture occurs. However, it seems that the situation is
more complex than that and also involves the crack velocity. We believe
that for the wavy transgranular fracture to occur the crack must be mov-
ing slowly so that when it encounters a resistant grain it can gradually
change to a less resistant transgranular path or go around the grain to
increase the K_I value acting on it. When the crack velocity increases

substantially as it does at K_{IC}, this may no longer be possible and the percentage of intergranular fracture increases.

The estimated K_I values at the subcritical crack growth boundary range from 3.55 - 4.31 MPa m$^{1/2}$. Based on the separate K_{IC} measurements, we would not have expected values over 3.8. Examination of the data shows that the high values occur in the cases in which there is substantial flaw linking along the surface to form a semi-elliptical region of sub-critical crack growth[*]. Careful examination of the fracture surfaces has not yet provided an explanation for this discrepancy.

The region beyond the subcritical crack growth boundaries contains large areas of wavy transgranular fracture. These areas contain relatively few of the linear features. If we are correct in assuming that wavy trans-granular fracture occurs in regions in which crack growth is slow, and occurs at low values of K_I, it means that these regions must form ahead of the main crack front. It seems possible that close examination of the river marks that indicate the direction of crack propagation in regions of transgranular fracture might provide evidence of the sequence in which cracking occurs. The same is true of the adjoining regions of inter-granular fracture and transgranular fracture with linear features. Pre-sumably, these regions resist fracture until K_I builds up to the point that fracture occurs at high velocities resulting in intergranular frac-ture and linear features in the transgranularly fractured grains.

---

[*] Note that these estimates of K_I took the ellipticity into account.

Transmission electron microscopy (TEM)

Perhaps the most powerful and versatile means for investigation of the micromechanisms of fracture of ceramics is TEM. Using this method Becher[31] has shown that, at elevated temperatures, plastic deformation in alumina is a result of mechanisms involving dislocations, mechanical twinning and/or grain boundary shear. Wiederhorn and coworkers[32] used TEM to study the tips of arrested tensile cracks in alumina single crystals at room temperature and failed to observe evidence of dislocation activity, indicating that the tensile fractures were perfectly brittle. However, plastic deformation does occur under compressive loading[33] and by explosive compaction[34] at room temperature. Explosive compaction yields dislocation generation and basal twinning as active deformation modes. Because the energy available to cause plastic deformation is much greater at overloaded cracks than at arrested cracks, it still seems possible that plastic deformation has occurred during the present fractures.

Slices that included the fracture surface as one surface were cut from some of the 96% Al_2O_3 specimens. These specimens were ion thinned. At first, ion thinning from the side opposite the fracture surface was attempted. For some reason, this method tended to make the material very friable so that the grains at the edges of holes tended to break off rather than become thinner. Therefore, the method was changed so that the slices were thinned from both sides but with the greatest ion bombardment on the side opposite the fracture surface. This change represents an undesirable compromise because the ion bombardment of the fracture surface will tend to remove the material that it was hoped to study. Nevertheless, using this method it was possible to obtain some thinned edges that were transparent enough to be studied.

Difficulties were also encountered in attempting to determine the locations of the thinned regions in relation to the fracture origins. This problem was overcome by taking pictures at various stages of thinning so that the changes in the outlines of the holes could be followed through the series.

The thinned specimens were examined by TEM using instruments located at Penn State University and at the National Bureau of Standards. The observations were made at locations far removed from the fracture origin in regions where the fracture surfaces had a disturbed appearance and excess energy was available to cause plastic deformation. The estimated K_I^* value was 12 MPa m$^{\frac{1}{2}}$. Numerous dislocations were observed in the photographs. The best photographs were taken by Dr. B. J. Hockey at NBS. Only limited attempts were made to characterize the observed dislocations. However, it was Dr. Hockey's judgement based on these observations that it was not necessary to invoke plastic deformation mechanisms during fracture to account for the presence of the observed dislocations. Some of these dislocations are shown in Figures 45 and 46. These figures show the change in appearance of the dislocation array as the tilt angle of the specimen is increased.

IV.   COARSE GRAINED 99+% ALUMINA (LUCALOX[+])

LUCALOX is a large grained, relatively pore free, alumina ceramic. A small number of cylindrical rods were fractured in flexure at room temperature. The fracture surface of one of these specimens was characterized with the results shown in Figure 47.

The photographs show the region surrounding the fracture origin on both halves of the specimen. The correspondence of features on both halves of the specimen is evident. The fracture origin is at the surface near the

---

+ General Electric Company, Cleveland, Ohio

Figure 35. Dislocations observed near fracture surface in a sample subjected to high E_1 696 alumina specimen 626, 36, 3650.

Figure 46. Dislocations observed near fracture surface in a region subjected to high K_I (96% alumina specimen 67B, 36,750X).
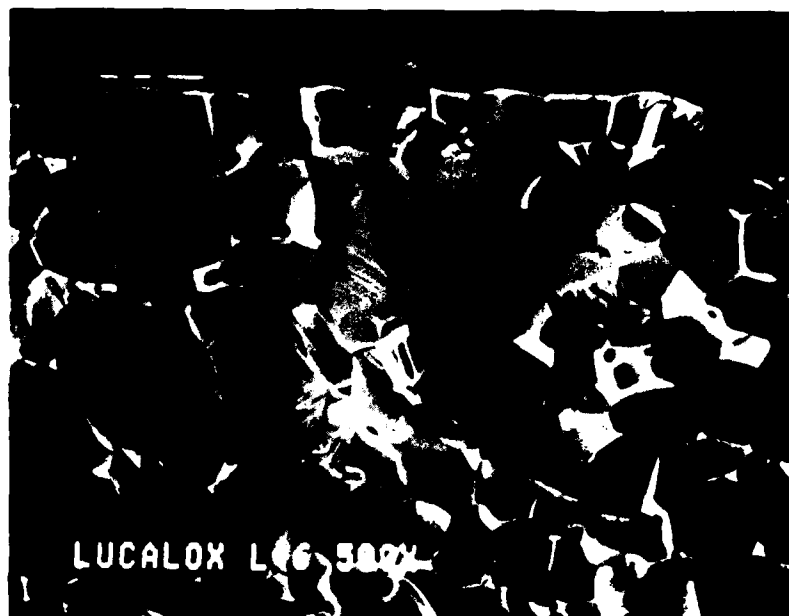
Figure 47. LUCALOX fracture surfaces, Specimen 1-6 fractured in flexure at 35°°C. Mating surfaces at fracture origin.

center of the photograph (horizontally). In the upper photograph, the
fracture origin may be located at the indentation in the surface that seems
to contain a small number of loose fragments.

The fracture origin is surrounded by a region of primarily trans-
granular fracture. This region is bounded by a row of projecting grains
located in a semi-elliptical line with a minor axis of about 80 μm
extending from the flaw to the boundary. On the matching photograph below,
the positions of the pullouts match those of the projecting grains above.
Beyond this boundary the fracture surface has a more disturbed appearance.

In 96% alumina, projecting grains and pullouts were one criterion
previously used for locating critical crack growth boundaries[2,8].
Observation of projecting grains and pullouts in LUCALOX raised the question
whether or not these features mark the critical crack growth boundary in
this case, also. Therefore, the critical stress intensity factor (K_{IC}) at
the boundary formed by the projecting grains was calculated using equation (1)
with σ_F = 345 MPa.   The K_{IC} values were calculated assuming either
semi-circular or elliptical flaws. Depending on the exact value of the
radius selected, the K_I values obtained assuming semi-circular flaws
ranged upward from 3.9 MPa $m^{\frac{1}{2}}$. Similarly, the K_I values obtained assuming
elliptical flaws ranged downward from 4.5 MPa $m^{\frac{1}{2}}$. The K_{IC} of LUCALOX is
4.1 MPa $m^{\frac{1}{2}}$[19]. Therefore, the present evidence indicates that the pro-
jecting grains and pullouts mark the subcritical crack growth boundary in

this specimen. Additional evidence supporting this conclusion is available in a photograph of a fracture surface to be published by Lankford[35].

Selected area electron channeling (SAEC)

To obtain definitive evidence of the micromechanisms by which fracture occurs, it is important to be able to determine the orientations of the individual grains in the fracture surface and the degree of plastic deformation of these grains. For example, it would be significant to be able to determine whether or not the projecting grains in Figure 47 are oriented so that the lattice planes in the fracture surface are resistant to fracture. Similarly, it would be significant to be able to determine the variation in the degree of plastic deformation of transgranularly fractured grains with variations in K_I and V along radii from the fracture origin.

Lankford and Davidson[36] have used SAEC to investigate the degree of plastic deformation in ceramic single crystals. In this cited reference they determined the depth of the plastic zone induced by grinding and polishing as a function of hardness for several ceramics including Al_2O_3.

Based on these results we decided to try to obtain channeling patterns from polycrystalline alumina specimens. This work was done by Lankford and Davidson at Southwest Research Institute. Initially, they attempted to obtain channeling patterns from some of our 96% alumina specimens. When this was unsuccessful, they switched to LUCALOX specimens from CFC and SWRI. These materials were found to have significantly different grain sizes; the specimens from CFC having grains ranging from 15-20 μm and the specimens from SWRI having grain sizes ranging from 24-40 μm.

The attempts to obtain channeling patterns from the finer grained specimens from CFC were unsuccessful but good patterns were obtained from

the coarser grained specimens. In one specimen, 12 grains were investigated yielding patterns of varying quality[35]. The quality of the patterns did not vary consistently with the appearance of the grains or with distance from the fracture origin. Also, it has not yet been possible to index the patterns to determine the orientations of the grains. Nevertheless, now that the conditions necessary to obtain patterns from fracture surfaces of this material are known, the prospects for determining crystal orientations and the degree of plastic deformation of individual grains seem promising.

V. CONCLUSIONS

1. In the three types of alumina ceramics investigated, the sizes of the flaws observed at the fracture origins are much smaller than the cracks necessary for $K_I = K_{IC}$ at the fracture stress. Therefore, subcritical crack growth must occur as part of the fracture process. In 96% alumina this statement applies for water and air (~40% rh), environments that enhance subcritical crack growth, and for CCl_4, an environment that does not enhance subcritical crack growth.

2. The subcritical crack growth occurs mainly by wavy transgranular fracture.

3. In addition to ordinary subcritical crack growth, the cracks grow by flaw linking. Flaw linking also occurs mainly by wavy transgranular fracture. In this investigation, most of the flaws involved in flaw linking were smaller and more widely separated than those described by Evans and Tappin[3]. Because the fracture stresses are similar, this raises the question of how the K_I value at the flaw can have been high enough to cause

linking. Evidence is lacking but the presence of regions that are less resistant to crack growth or the presence of localized residual stresses due to thermal expansion or elastic anisotropy are reasonable explanations.

4. In 96% alumina fractured at approximately constant K_I and crack velocities in the range 10^{-5}-10^{-6} m.s^{-1} in WOF tests, fracture occurred mainly by transgranular fracture. The average WOF values were slightly higher in CCl_4 than in environments containing water suggesting that the presence of water lowers the WOF and modifies the mechanism of fracture in the subcritical crack growth region.

5. In 96% alumina etched 20 hours to remove the siliceous intergranular phase the WOF values were increased substantially. It seems likely that weakening the grain boundaries by etching enhances microcracking ahead of the crack, increasing the size of the so-called process zone and leading to the higher WOF values. In the etched material the average WOF values of the environments containing water are higher than the value for CCl_4. A possible explanation of this observation is that, in the water containing environments, the water enhances the microcracking to yield a larger process zone than that in CCl_4. The large changes in the effect of environment on WOF obtained by etching, and the reversal of the relative magnitudes of the WOF values, may help to explain earlier cases in which contradictory results have been reported.

6. The boundary between the subcritical and critical crack growth regions in H.P. and 96% alumina is characterized by a minimum in percent intergranular fracture. This minimum also coincides approximately with the K_{IC} value (K_{IC} = 4.3 MPa m$^{\frac{1}{2}}$) necessary for fracture on $\{1\bar{1}26\}$ planes in

102

single crystals suggesting a possible mechanism controlling the transition

to critical crack growth. In 96% alumina and LUCALOX, the coarser grained

materials, the subcritical to critical crack growth boundary is also fre-

quently characterized by a row of pullouts and projecting grains suggesting

a second possible mechanism in these materials.

7. The fraction of transgranularly fractured surface containing

linear features increases strongly with apparent stress intensity factor.

The linear features include river marks, ordinary cleavage steps, striations,

cracks and other types of features.

8. The areas of transgranular fracture just before large scale crack

branching are smaller than those just after crack branching. In most other

respects the fracture surfaces, before and after, seem very similar.

Incipient branching similar to mist in glass was not observed.

VI. REFERENCES

1. H. P. Kirchner, W. R. Buessem, R. M. Gruver, D. R. Platts and R. E. Walker, "Chemical Strengthening of Ceramic Materials," Ceramic Finishing Company Summary Report, Contract N00019-70-C-0418 (December, 1970).

2. H. P. Kirchner and R. M. Gruver, "Fractographic Criteria for Subcritical Crack Growth Boundaries in 96% Al_2O_3," J. Amer. Ceram. Soc. 63 (3-4) 169-174 (1980).

3. A. G. Evans and G. Tappin, "Effects of Microstructure on the Stress to Propagate Inherent Flaws," Proc. Brit. Ceram. Soc. 20, 275-297 (June,1972).

4. S. M. Wiederhorn, "Fracture of Sapphire," J. Amer. Ceram. Soc. 52 (9) 485-491 (1969).

5. R. M. Gruver, W. A. Sotter and H. P. Kirchner, "Fractography of Ceramics," Ceramic Finishing Company Summary Report, Contract N00019-73-C-0357 (November, 1974).

6. H. P. Kirchner, R. M. Gruver and W. A. Sotter, "Characteristics of Flaws at Fracture Origins and Fracture Stress-Flaw Size Relations in Various Ceramics," Mater. Sci. Eng. 22, 147-156 (1976).

7. R. M. Gruver, W. A. Sotter and H. P. Kirchner, "Variation of Fracture Stress with Flaw Character in 96% Al_2O_3," Amer. Ceram. Soc. Bull. 55 (2) 198-202 (1976).

8. H. P. Kirchner, R. M. Gruver, D. M. Richard, "Fractographic Investigation of Subcritical Crack Growth at Inherent Flaws in Polycrystalline Ceramics," Ceramic Finishing Company Summary Report, Contract N00019-77-C-0328 (November, 1978).

9. H. P. Kirchner and R. M. Gruver, "A Fractographic Criterion for Subcritical Crack Growth Boundaries in Hot-Pressed Alumina," J. Mater. Sci. 14, 2110-2118 (1979).

10. H. P. Kirchner, R. M. Gruver and D. M. Richard, "A Fractographic Criterion for Subcritical Crack Growth Boundaries at Internal Fracture Origins in Silicon Nitride," J. Mater. Sci. 14, 2713-2720 (1979).

11. H. P. Kirchner and D. M. Richard, "Fracture Stress-Reflecting Spot Relations in Hot-Pressed Alumina," J. Mater. Sci. 15, 1319-1321 (1980).

12. A. B. J. Clark and G. R. Irwin, "Crack Propagation Behaviors," Experimental Mechanics 6 (6) 321-330 (1966).

13. J. Congleton and N. J. Petch, "Crack Branching," Phil. Mag. Series 8, 16, 749-760 (1967).

14. G. K. Bansal and W. Duckworth, "Effects of Specimen Size on Ceramic Strengths," from Fracture Mechanics of Ceramics," Vol. 3, Edited by R. C. Bradt, D. P. H. Hasselman and F. F. Lange, Plenum, New York (1978) pages 189-204.

15. H. P. Kirchner, "The Strain Intensity Criterion for Crack Branching in Ceramics," Engineering Fracture Mechanics 10, 283-288 (1978).

16a. J. Lebiedzik, "Multiple Electron Detector Method for Quantitative Microtopographic Characterization in the SEM," PhD Thesis, Penn State U. (1975).

  b. J. Lebiedzik, J. Lebiedzik, R. Edwards and B. Phillips, "Use of Micro-topography Capability in the SEM for Analyzing Fracture Surfaces," Scanning Electron Microscopy 61-66 (1979).

17. Contract N00019-77-C-0328, Unpublished research (1978).

18. B. R. Lawn and T. R. Wilshaw, "Fracture of Brittle Solids," Cambridge University Press, New York (1975) page 113.

104

19. S. W. Freiman, K. R. McKinney and H. L. Smith, "Slow Crack Growth in Polycrystalline Ceramics," from Fracture Mechanics of Ceramics, Vol. 2, Edited by R. C. Bradt, D. P. H. Hasselman and F. F. Lange, Plenum, New York (1974) pages 659-676.

20. D. Munz, R. T. Bubsey and J. L. Shannon, Jr. "Fracture Toughness Determination of Al_2O_3 Using Four-Point-Bend Specimens with Straight-Through and Chevron Notches," J. Amer. Ceram. Soc. 63 (5-6) 300-305 (1980).

21. H. P. Kirchner and D. A. Sentner, "Toughened Ceramic Adhesives for Structural Ceramics," Ceramic Finishing Company Report, NSF Grant No. DAR-8009270 (February, 1981).

22a. R. E. Cuthrell, "The Effect of Chemical Environments on the Fracture of Ceramic Surfaces," from the Science of Ceramic Machining and Surface Finishing II, Edited by B. J. Hockey and R. W. Rice, National Bureau of Standards Special Publication No. 562 (October, 1979) pages 139-145.

 b. R. E. Cuthrell and E. Randich, "The Embrittling Effects of Hydrogen on a Variety of Inorganic Materials as Indicated by Acoustic Emission," J. Mater. Sci. 14, 2563-2566 (1979).

 c. R. E. Cuthrell, "The Role of Ion Aggregates in Rebinder-Westwood Environmental Effects on Wear as Monitored by Acoustic Emission," J. Appl. Phys. 49 (1) 432-436 (1978).

23. R. W. Davidge and G. Tappin, "The Effects of Temperature and Environment on the Strength of Two Aluminas," Proc. Brit. Ceram. Soc. 15, 47-60 (1970).

24. A. G. Evans, "A Method for Evaluating the Time-Dependent Failure Characteristics of Brittle Materials- and Its Application to Polycrystalline Alumina," J. Mater. Sci. 7 (10) 1137-1146 (1972).

25. D. F. Dailly, G. W. Hastings and S. Lach, "Stress Corrosion in Debased Alumina," Special Ceramics 7, Proc. Brit. Ceram. Soc. 31, 191-200 (1981).

26. P. A. Rishel, J. M. Infield and H. P. Kirchner, "Leaching and Machining of Polycrystalline Alumina," Bull. Amer. Ceram. Soc. 47 (6) 702-706 (1968).

27. H. P. Kirchner and R. E. Walker, "Delayed Fracture of Alumina Ceramics with Compressive Surface Layers," Mater. Sci. Eng. 8, 301-309 (1971).

28. H. P. Kirchner, R. M. Gruver and R. E. Walker, "Strength Effects Resulting from Simple Surface Treatments," from The Science of Ceramic Machining and Surface Finishing, Edited by S. J. Schneider, Jr. and R. W. Rice, NBS Special Publication 348 (May, 1972) pages 353-363.

29a. C. S. Barrett, "Structure of Metals," McGraw-Hill Book Company, New York (1943) page 310.

 b. A. H. Heuer, "Plastic Deformation in Polycrystalline Alumina," Proc. Brit. Ceram. Soc. 15, 173-184 (1970).

29c. L. R. Hillier, "Natural Uranium Dioxide Fuel Pellet," J. Amer. Ceram. Soc. 61 (5-6) back cover (1978).

30. D. B. Marshall and B. R. Lawn, "Flaw Characteristics in Dynamic Fatigue: The Influence of Residual Contact Stresses," J. Amer. Ceram. Soc. 63 (9-10) 532-536 (1980).

31. P. F. Becher, "Deformation Behavior of Alumina at Elevated Temperatures," from Ceramics in Severe Environments, Vol. 5, Edited by W. W. Kriegel and H. Palmour III, Plenum, New York (1971) pages 315-329.

32. S. M. Wiederhorn, B. J. Hockey, and D. E. Roberts, "Effect of Temperature on the Fracture of Sapphire," Phil. Mag. 28, 783-796 (1973).

33. B. J. Hockey, "Observations on Mechanically Abraded Aluminum Oxide Crystals by Transmission Electron Microscopy," from The Science of Ceramic Machining and Surface Finishing, Edited by S. J. Schneider, Jr., and R. W. Rice, NBS Special Publication 348 (1972) pages 333-339.

34. C. S. Yust and L. A. Harris, "Observations of Dislocations and Twins in Explosively Compacted Alumina," To be published in the proceedings of The International Conference on the Metallurgical Effects of High Strain Rate Deformation and Fabrication, Albuquerque, New Mexico (1980).

35. J. Lankford and D. L. Davidson, "Electron Channeling Study of Fracture in Alumina-Evidence for Crack Tip Plasticity," To be published in the proceedings of The Third International Symposium on Fracture Mechanics of Ceramics (1981).

36. J. Lankford and D. L. Davidson, "Characterization of Surface Damage in Ceramics Using Selected Area Electron Channeling," from The Science of Ceramic Machining and Surface Finishing II, Edited by B.J. Hockey and R. W. Rice, NBS Special Publication 562 (October, 1979) pages 395-405.

DISTRIBUTION LIST

Commander	(19)	Brookhaven National Laboratory	(1)

Commander (19)
Naval Air Systems Command
Washington, D.C. 20361
Attn: AIR-00D4 (12)
     AIR-310C (1)
     AIR-320A (1)
     AIR -5163D4 (5)

Office of Naval Research (1)
800 N. Quincy St.
Arlington, VA 22217
Attn: Code 471

Commander (1)
Naval Surface Weapons Center
White Oak
Silver Spring, MD. 20910
Attn: Code R31

Director (2)
Naval Research Laboratory
Washington, D.C. 20375
Attn: Code 6360
     Code 8433

Commanding Officer (1)
David W. Taylor Naval Ship Re-
   search & Development Center
Annapolis, MD. 21412
Attn: W. Smith, Code 2832

Commanding Officer (1)
Naval Air Propulsion Center
Trenton, N.J. 08628
Attn: R. Valori, Code PE 72

Commander (1)
Naval Air Development Center
Warminster, PA. 18974
Attn: Code 6061

Commander (4)
Air Force Wright Aeronautical
   Laboratories
Wright-Patterson Air Force Base
Dayton, OH. 45433
Attn: Dr. J. Dill   POSL 1
     Dr. H. Graham   MLLM 1
     Mr. B.D. McConnell MLBT 1
     Ms. K. Lark   MLTM 1

Brookhaven National Laboratory (1)
Upton, N.Y. 11973
Attn: Dr. D. VanRooyen

Director (1)
Applied Technology Laboratory
U.S. Army Research and Tech-
   nology Laboratories
Fort Eustis, VA. 23604
Attn: DAVDL-ATL-ATP (Mr. Pauze)

U.S. Army Research Office (1)
Box CM, Duke Station
Durham, N.C. 27706
Attn: CRCARD

U.S. Army MERDC (1)
Fort Belvoir, VA. 22060
Attn: SMEFB-EP (W. McGovern)

Army Materials and Mechanics (1)
   Research Center
Watertown, MA. 02172
Attn: Dr. R. N. Katz

NASA Headquarters (1)
Washington, D.C. 20546
Attn: C. F. Bersch, RIM-6

NASA Lewis Research Center (2)
21000 Brookpark Rd.
Cleveland, OH. 44135
Attn: Dr. E. Zaretsky   1
     W. A. Sanders (49-1)
     and Dr. T. Hergell   1

Defense Advanced Research Project (1)
   Office
1400 Wilson Blvd.
Arlington, VA. 22209
Attn: Dr. VanReuth

Inorganic Materials Division (1)
Institute for Materials Research
National Bureau of Standards
Washington, D.C. 20234

Department of Engineering (1)
University of California
Los Angeles, CA. 90024
Attn: Profs. J. W. Knapp and
     G. Sines

Engineering Experiment Station (1)
Georgia Institute of Technology
Atlanta, GA. 30322
Attn: J. D. Walton

University of Illinois (1)
College of Engineering
204 Ceramics Building
Urbana, IL. 61801
Attn: Sherman D. Brown
Dept. of Ceramic Engineering

Department of Metallurgy (1)
Massachusetts Institute of
Technology
Cambridge, MA. 02139

Department of Engineering Research (1)
North Carolina State University
Raleigh, N.C. 27607
Attn: Dr. H. Palmour

Ceramic Science and Engineering (1)
Section
Pennsylvania State University
University Park, PA. 16802
Attn: Dr. R. E. Tressler

Rensselaer Polytechnic Institute (1)
110 Eighth Street
Troy, N.Y. 12181
Attn: R. J. Diefendorf

School of Ceramics (1)
Rutgers, The State University
New Brunswick, N.J. 08903

Virginia Polytechnic Institute (1)
Minerals Engineering
Blacksburg, VA. 20460
Attn: Dr. D. P. H. Hasselman

Advanced Mechanical Technology Inc.(1)
141 California Street
Newton, MA. 02158
Attn: Dr. Walter D. Syniuta

Aerospace Corporation (1)
Materials Laboratory
P.O. Box 95085
Los Angeles, CA. 90045

Supervisor, Materials Engineering (1)
Department 93-39M
AiResearch Manufacturing Company
of Arizona
402 South 36th Street
Pheonix, AZ. 85034

Materials Development Center (1)
AVCO Systems Division
Wilmington, MA. 01887
Attn: Tom Vasilos

Lycoming Division (1)
AVCO Corporation
Stratford, CT. 06497
Attn: Mr. D. Wilson

Batelle Memorial Institute (2)
505 King Avenue
Columbus, OH. 43201
Attn: Ceramics Dept. 1
Metal & Ceramic
Info. Center 1

Bell Helicopter Textron (1)
P.O. Box 482
Fort Worth, TX. 76101
Attn: R. Battles

The Boeing Company (1)
Materials and Processes Labor-
atory
Aerospace Group
Seattle, WA. 98124
Attn: J. VanWyk

Research and Development Division (1)
Carborundum Company
Niagra Falls, N.Y. 14302
Attn: Mr. C. McMurty

Ceradyne, Inc. (1)
Box 1103
Santa Ana, CA. 92705

Coors Porcelain Company (1)
600 Ninth Street
Golden, CO. 80401
Attn: Research Dept.

Glass-Ceramics Research Dept. (1)
Corning Glass Works
Corning, N.Y. 14832

Cummings Engine Company Columbus, IN. 47201 Attn: Mr. R. Kamo, Director of Research	(1)	NDH Division General Motors Corporation Hayes Street Sandusky, OH. 44870 Attn: H. Woerhle	(1)
Curtiss-Wright Company Wright Aeronautical Division One Passaic Street Woodridge, N.J. 07075	(1)	Hughes Aircraft Company Culver City, CA. 90230 Attn: M. N. Gardos	(1)
E. I. DuPont de Nemours & Co. Experimental Station, Bldg. 302 Wilmington, DE. 19898	(1)	IIT Research Institute 10 West 35th Street Chicago, IL. 60616 Attn: Ceramics Division	(1)
Federal-Mogul Corporation Anti-Friction Bearing R&D Center 3980 Research Park Drive Ann Arbor, MI. 48104 Attn: D. Glover	(1)	Industrial Tectonics, Inc. 18301 Santa Fe Avenue Compton, CA. 90224 Attn: Hans R. Signer	(1)
Fiber Materials, Inc. Biddeford Industrial Park Biddeford, ME. 04005 Attn: Dr. H. Dean Batha	(1)	Kaweki-Berylco Industry Box 1462 Reading, PA. 19603 Attn: Mr. R. J. Longnecker	(1)
Product Development Group Ford Motor Company 20000 Rotunda Drive Dearborn, MI. 28121 Attn: Mr. E. Fisher	(1)	Research and Development Div. Arthur D. Little Company Acorn Park Cambridge, MA. 02140	(1)
Aircraft Engine Group Technical Information Center Main Drop N-32, Building 700 General Electric Company Cincinnati, OH. 45215	(1)	Materials Research Corporation Orangeburg, N.Y. 10962	(1)
		Mechanical Technology, Inc. 968 Albany-Shaker Road Latham, N.Y. 12110 Attn: Dr. E. F. Finkin	(1)
Mettalurgy and Ceramics Research Department General Electric R&D Laboratories P.O. Box 8 Schenectady, N.Y. 12301	(1)	Norton Company Industrial Ceramics Division One New Bond Street Worcester, MA. 01606 Attn: Dr. M. Torti	(1)
Space Sciences Laboratory General Electric Company P.O. Box 8555 Philadelphia, PA. 19101	(1)	Raytheon Company Research Division 28 Seyon Street Waltham, MA. 02254	(1)
Detroit Diesel Allison Division General Motors Corporation P.O. Box 894 Indianapolis, IN. 46206 Attn: Dr. M. Herman	(1)	North American Rockwell Science Center P.O. Box 1085 Thousand Oaks, CA. 91360	(1)

109

Ceramic Division (1)
Sandia Corporation
Albuquerque, N.M. 87101

SKF Technology Services (1)
SKF Industries, Inc.
1100 First Street
P.O. Box 515
King Of Prussia, PA. 19406
Attn: P. A. Madden

Solar Turbines International (1)
P.O. Box 80966
San Diego, CA. 92138
Attn: G. W. Hosang

Southwest Research Institute (1)
P.O. Drawer 28510
San Antonio, TX. 78228

Materials Sciences & Engineering (1)
    Laboratory
Stanford Research Institute
Menlo Park, CA. 94025
Attn: Dr. Cubiciotti

Teledyne CAE (1)
1330 Laskey Road
Toledo, OH. 43601
Attn: Hugh Gaylord

Marlin Rockwell, Division of TRW (1)
Jamestown, N.Y. 14701
Attn: John C. Lawrence and
      A. S. Irwin

Union Carbide Corporation (1)
Parma Technical Center
P.O. Box 6116
Cleveland, OH. 44101

Union Carbide Corporation (1)
Electronics Division
P.O. Box 23017
San Diego, CA. 92100

Materials Sciences Laboratory (1)
United Technologies
East Hartford, CT. 06101
Attn: Dr. J. J. Brennan

Pratt & Whitney Aircraft Group (1)
Government Products Division
United Technologies
P.O. Box 2691
West Palm Beach, FL. 33402
Attn: Mr. J. Miner

United Technologies Research Center (1)
East Hartford, CT. 06108
Attn: F. L. Ver Snyder

Astronuclear Laboratory (1)
Westinghouse Electric Corporation
Box 10864
Pittsburgh, PA. 15236

Westinghouse Research Laboratories (1)
1310 Beulah Road
Churchill Borough
Pibbsburgh, PA. 15235
Attn: Dr. R. Bratton

Williams Research Corporation (1)
Walled Lake, MI.
48088

FIL

02